UNIVERSITY OF OKLAHOMA
GRADUATE COLLEGE

Enhanced Measurement of Transmission with Quantum States of Light

A DISSERTATION
SUBMITTED TO THE GRADUATE FACULTY
in partial fulfillment of the requirements for the
Degree of
DOCTOR OF PHILOSOPHY

By

TIMOTHY S. WOODWORTH
Norman, Oklahoma
2022

Downloaded from SHAREOK. Persistent Handle URL: https://hdl.handle.net/11244/336869

Enhanced Measurement of Transmission with Quantum States of Light

A DISSERTATION APPROVED FOR THE
HOMER L. DODGE DEPARTMENT OF PHYSICS AND ASTRONOMY

BY THE COMMITTEE CONSISTING OF

Dr. Alberto M. Marino, Chair

Dr. Doerte Blume

Dr. Arne Schwettmann

Dr. Ian Sellers

Dr. Choon Yik Tang

Chapter 4 Copyright by American Physical Society 2020
Chapter 6 and Appendix C Copyright by IOP Publishing 2021
All other chapters
Copyright by TIMOTHY S. WOODWORTH 2022
All Rights Reserved.

Curriculum Vitae

Publications

Timothy S. Woodworth, Carla Hermann-Avigliano, Kam Wai Clifford Chan, and Alberto M. Marino, "Transmission estimation at the fundamental quantum Cramér-Rao bound with macroscopic quantum light", arXiv:2201.08902 (2022)

Mohammadjavad Dowran, Timothy S. Woodworth, Ashok Kumar, and Alberto M. Marino, "Fundamental sensitivity bounds for quantum enhanced optical resonance sensors based on transmission and phase estimation", Quantum Science and Technology **7**, 015011 (2021)

Timothy S. Woodworth, Kam Wai Clifford Chan, Carla Hermann-Avigliano, and Alberto M. Marino, "Transmission estimation at the Cramér-Rao bound for squeezed states of light in the presence of loss and imperfect detection", Physical Review A **102**, 052603 (2020)

Conference Presentations

2022 Quantum 2.0
Transmission Estimation at the Fundamental Limit With Bright Quantum States of Light

2021 Southwest Quantum Information and Technology Conference
Single Mode Squeezers for Enhancement of Transmission Estimation with Macroscopic Quantum States

2021 Division of AMO Physics Conference
Optimal Transmission Estimation Using Macroscopic Quantum States of Light

2020 Southwest Quantum Information and Technology Conference
Comparison of the Quantum Cramér-Rao Bounds for Quantum-Enhanced Resonant Detection Based on Phase and Transmission Estimation

2019 Southwest Quantum Information and Technology Conference
Experimental Saturation of the Quantum Cramér-Rao Bound for Transmission Measurements

2018 International Conference on Quantum Communication, Measurement and Computing
Reaching the Quantum Cramér-Rao Bound for Transmission with a Simple Measurement Scheme

2018 Southwest Quantum Information and Technology Conference
Reaching the Quantum Cramér-Rao Bound for Transmission with a Simple Measurement Scheme

2017 Division of AMO Physics Conference
Reaching the Quantum Cramér-Rao Bound for Transmission with a Simple Measurement Scheme

Acknowledgments

If you were successful, somebody along the line gave you some help. There was a great teacher somewhere in your life. Somebody helped to create this unbelievable American system that we have that allowed you to thrive. Somebody invested in roads and bridges. If you've got a business, you didn't build that. Somebody else made that happen. The Internet didn't get invented on its own. Government research created the Internet so that all the companies could make money off the Internet.

— US President Barack Obama

It is impossible to thank everyone who made it possible for me to come this far. Growing up, who knows how many teachers, friends, and family members helped push me towards a life of science? So instead, I am going to thank my mom. While everyone else may have planted the seeds, she watered and fertilized my future career. I remember back when I was a kid, she even got in contact with a college professor to learn more about some pseudoscience job I was interested in from a Micheal Crichton book.

As for the professors who taught me how to be a physicist, starting when I was at Spoon River College, Dr. Win Htwe taught three semester of physics classes consisting of me, myself, and I. If he had not been so dedicated to teaching, I may not have stayed in physics. I am thankful he was willing to do so much for me.

At Western Illinois University, I would like to thank my undergrad advisor Dr. Pengqian Wang for introducing me to experimental research and my Master's advisor Dr. Kishor T. Kapale for showing me the wonders of theory, where things actually work like they are supposed to. I would also like to thank Drs. Esteban D. Araya, P. K. Babu, Mark S. Boley, Saisudha B. Mallur, and Jim Rabchuk for all their teaching, help, and support through my years at WIU.

Here at OU, the list of faculty is so much larger, so I am not going to write out everyone's name. Too many have helped and supported me. Everyone here is dedicated to teaching the next generation of scientist and making sure we have the tools to succeed when we leave.

Though, I really should thank the guys in the mechanical and electrical shop, Chad and Alex, for putting up with me. I was constantly bugging them to build my stuff, fix my stuff (that I broke), and order my stuff. They always got it done quickly and with a smile, and maybe just a little teasing.

And finally, I wish to thank my Ph.D. Advisor, Dr. Alberto M. Marino. He has always shown great patience with me. From the time when I first started and spent half the day either in his office or waiting for him in front of it with thousands of questions to the middle

years when nothing in the experiment worked and I was a big ball of frustration and anger. I am grateful for his guidance and *constant* push to give it my all. I would not be the scientist I am today without him.

Abstract

Quantum metrology is the application of quantum mechanics towards the enhancement of measurements. This is typically achieved through either quantum measurements, such as photon counting, or using quantum states. In this thesis, we focus on the use of a high power quantum state of light, known as the bright two mode squeezed state, to achieve a quantum enhancement in the estimation of transmission by reducing the uncertainty in the value down to the fundamental limit allowed by quantum mechanics. These bright two mode squeezed states are of particular use to enhance the precision of many sensing devices beyond the classical limit, via quantum enhancement, and current state-of-the-art due to being generated at high power.

We start with an introduction to the theoretical calculations that set the fundamental lower limit in the uncertainty in the estimation of a parameter, transmission in our case. This limit is given by the quantum Cramér-Rao bound. We go over the bound for the bright single mode squeezed state and calculate the bound for the bright two mode squeezed state. These squeezed states offer a large enhancement in transmission estimation at high transmissions compared to classical states. We also expand on these bound to include losses in the states both before and after probing the transmissive system and detail measurements that are able to saturate the quantum Cramér-Rao bound, even in the presence of loss. Operating at this bound means that, for our state, no other estimation can do better.

We experimentally verify that we can estimate transmission at the quantum Cramér-Rao bound for the bright two mode squeezed state. Achieving such uncertainty levels at the quantum Cramér-Rao bound required extensive control of our experiment and precise calibration of our state and system. In addition, we expand upon the calculations of the quantum Cramér-Rao bound to include generation of the bright two mode squeezed state in a more realistic system that takes into account the absorptive medium that is used.

Finally, we examine systems that have a resonant frequency dependent transmission and phase responses. This allows us to compare and identify the optimal measurement parameter for use in estimating frequency shifts in the system response. We focus on systems with resonance responses, in which there is a large change in transmission around a single frequency. We show that for resonances with the common Lorentzian lineshape, the phase measurement is in general more sensitive to frequency shifts than the transmission measurements. However, for lineshapes with a sharper change in transmission, we show that the transmission measurement can do better than phase measurements.

Contents

Acknowledgments vi

Abstract viii

List of Tables xii

List of Figures xiv

List of Acronyms xv

List of Symbols xvii

1 Introduction 1
- 1.1 Transmission estimation . . . 4
- 1.2 Outline . . . 5

I Background Information 6

2 Gaussian States of Light 7
- 2.1 Representations of states . . . 9
- 2.2 Gaussian states of light . . . 11
  - 2.2.1 Vacuum and coherent states . . . 11
  - 2.2.2 Squeezed states . . . 12
  - 2.2.3 Two mode squeezed states . . . 14
  - 2.2.4 Thermal state and density matrices . . . 16

3 Parameter Estimation Limits: The Cramér-Rao Bound and Fisher Information 18
- 3.1 Parameter estimation bounds . . . 19
  - 3.1.1 Classical Fisher information . . . 20
  - 3.1.2 Quantum Fisher information . . . 21
  - 3.1.3 Other forms of the quantum Fisher information . . . 23

II Quantum Enhanced Transmission Estimation **26**

4 QCRB of Transmission with Gaussian States of Light **27**
4.1 Modeling transmission estimation . . . 27
4.1.1 Classical and ultimate limit for transmission estimation . . . 29
4.2 Quantum enhanced QCRB with squeezed states . . . 31
4.2.1 Single mode squeezed states . . . 31
4.2.2 Two mode squeezed states . . . 33
4.3 QCRB with extraneous losses and imperfect detection . . . 37
4.4 Measurements that saturate the QCRB for transmission estimation . . . 39

5 Experimental Saturation of the Transmission QCRB with a bTMSS **44**
5.1 Overview of the experiment . . . 44
5.1.1 State generation . . . 45
5.1.2 Converting variance of measurement to transmission uncertainty . . . 48
5.1.3 System . . . 50
5.1.4 Results . . . 52
5.2 Control . . . 54
5.2.1 Transmission modulation control . . . 54
5.2.2 State control . . . 56
5.3 Calibration . . . 57
5.3.1 EOM calibration . . . 57
5.3.2 Photon flux to photon number conversion . . . 58
5.3.3 State characterization for determining the QCRB . . . 64
5.4 Final results . . . 69

6 Resonance Sensors: Comparison of Sensitivity Limits Based on Phase and Transmission Measurements **71**
6.1 Lossy phase estimation with a bTMSS . . . 74
6.1.1 Measurement to saturate phase bound . . . 75
6.2 Frequency estimation . . . 77

7 Conclusion **88**
7.1 Future outlook: multiple transmissions . . . 89
7.1.1 Two transmission measurements for estimating a single parameter . . . 89

III Appendices **91**

A Covariance Matrix for bTMSS Generated in an Absorptive Medium **92**

B Fitting of Theory Parameters to Experimental Measurement Results **98**
B.1 Differential evolution 99
B.2 Finding s and T_x 100

C Kramers-Kronig Relations **102**

List of Tables

6.1 Frequency for maximum sensitivity 80
6.2 Maximum slopes for Butterworth lineshape 83

List of Figures

2.1 Phase space representations 10

3.1 Block diagram of parameter estimation 18
3.2 Displacement example 25

4.1 Setup of theoretical model for transmission estimation 28
4.2 Diagram of ultimate limit setup 29
4.3 Plot of transmission estimation functions for squeezed states 35
4.4 Plot showing the effects on loss on transmission estimation 39
4.5 Intensity and optimized intensity difference measurement 40

5.1 Setup of experiment for transmission estimation 45
5.2 Probe detuning from pump 47
5.3 Ramping of SNR to find transmission uncertainty 48
5.4 Conversion of voltage modulation to transmission modulation using EOM . . 52
5.5 Plot of experimental results 53
5.6 EOM lock diagram 55
5.7 Pound-Drever-Hall error signal 56
5.8 Calibration of transmission modulation 58
5.9 Diagram of spectrum analyzer 59
5.10 Plot of experimental results with photon counting 64
5.11 Absorptive squeezing model 65
5.12 Plot of experimental results showing saturation of transmission QCRB . . . 70

6.1 Response of a resonance sensor 72
6.2 Simple plot of peak and dip resonance 78
6.3 Plots of resonance sensitivity comparisons 79
6.4 Plot of resonance sensitivity as a function of squeezing 82
6.5 Graphs comparing resonance sensitivity using transmission or phase for different lineshapes 84
6.6 Effects of loss on resonance sensitivity 85

7.1 Two transmissions plot 90

A.1 Schematic of absorptive squeezing 94

List of Acronyms

AOM	Acousto-Optical Modulator	A gradient created by sound waves used as a frequency shifter.
BGPR	Bode Gain-Phase Relation	Relation between the frequency dependent transmission and minimum phase response.
bSMSS	Bright Single Mode Squeezed Light	A single mode Gaussian quantum state with a large amplitude and one quadrature variance below the Quantum Noise Limit (QNL).
bTMSS	Vacuum Two Mode Squeezed State	A two mode Gaussian quantum state with a large amplitude in either mode and a sum or difference of mode quadrature variances below the Quantum Noise Limit (QNL).
DE	Differential Evolution	A genetic algorithm used for optimization.
EOM	Electro-Optical Modulator	Crystal that retards one polarization of light by an amount governed by an applied voltage.
EM	Electro-Magnetic	Field that composes the radiation of light.
EQEF	Effective Quantum Enhancement Factor	Used in the resonance sensor chapter to quantify the quantum enhancement of an estimation when using quantum light instead of classical.
FFT	Fast Fourier Transform	Algorithm to quickly compute the Fourier transform.
FHT	Fast Hilbert Transform	Uses the Fast Fourier Transform (FFT) to quickly perform a Hilbert transform.
FOM	Figure of Merit	Used in the resonance sensor chapter to compare phase measurements to transmission measurements for frequency estimation.
FWM	Four Wave Mixing	A process that can be used to generate a two mode squeezed states by interaction of four photons from up to four different modes of light.

HWHM	Half-Width at Half-Maximum	The distance from maximum value to half maximum value.
KKR	Kramers-Kronig Relation	Relation between the real and imaginary part of a transfer function.
LIGO	Laser Interferometer Gravitational-Wave Observatory	Observatory used to measure gravitational waves.
LO	Local Oscillator	High amplitude modulation used as a phase reference.
LPF	Low Pass Filter	Used to attenuate high frequencies and pass low frequencies
PDH	Pound-Drever-Hall	Technique, named after the researchers who discovered it, used to generate a derivative signal for locking to a maximum or minimum value.
PBS	Polarizing Beam Splitter	A prism used to split light into component parts given by the polarization of the incident light.
POVM	Positive Operator Valued Measurement	A way to describe an arbitrary measurement in quantum mechanics.
QNL	Quantum Noise Limit	The minimum variance of a measurement when using classical states of light.
RBW	Resolution Bandwidth	Low Pass Filter (LPF) used in spectrum analyzers to set the frequency resolution.
SLD	Symmetric Logarithmic Derivative	Symmetric operator form of the derivative of the log of a matrix.
SNR	Signal-to-Noise Ratio	Amplitude of the signal in terms of multiples of the background noise.
VBW	Video Bandwidth	Low Pass Filter (LPF) used in spectrum analyzers to set the bandwidth for smoothing of traces.
vSMSS	Vacuum Single Mode Squeezed State	A single mode Gaussian quantum state of zero mean amplitude and one quadrature variance below the Quantum Noise Limit (QNL).
vTMSS	Vacuum Two Mode Squeezed State	A two mode Gaussian quantum state of zero mean amplitude in either mode and a sum or difference of mode quadrature variances below the Quantum Noise Limit (QNL).

List of Symbols

$\vec{A}$	A vector
$\hat{A}$	An operator
$\langle \hat{A} \rangle$	Expectation value
$\langle \Delta^2 \hat{A} \rangle$	Variance
i	$\sqrt{-1}$
A^*	Complex conjugate ($i \to -i$)
$\hat{A}^T$	Transpose $\left(\begin{pmatrix} a & b \\ c & d \end{pmatrix} \to \begin{pmatrix} a & c \\ b & d \end{pmatrix} \right)$
$\hat{A}^\dagger$	Conjugate transpose $\left(i \to -i \text{ and } \begin{pmatrix} a & b \\ c & d \end{pmatrix} \to \begin{pmatrix} a & c \\ b & d \end{pmatrix} \right)$
$\hat{a}_j$	Field operator for mode j
$\hat{n}_j$	Photon number operator for mode j
$\hat{Q}$	Quadrature operator
$\hat{X}$	Amplitude quadrature operator
$\hat{Y}$	Phase quadrature operator
$[\hat{A}, \hat{B}]$	Commutation relation ($\hat{A}\hat{B} - \hat{B}\hat{A}$)
$\{\hat{A}, \hat{B}\}$	Anti-commutation relation ($\hat{A}\hat{B} + \hat{B}\hat{A}$)
$\vec{d}$	Displacement vector
$\boldsymbol{\sigma}$	Covariance matrix
Σ	Covariance matrix in symplectic form
$\hat{D}$	Displacement operator
$\hat{S}$	Squeezing operator
$\hat{B}$	Beam splitter operation
$\hat{G}$	Generator operator used to cause an evolution of a parameter, *i.e.* momentum is a generator for position.
ρ	Density matrix
F^Q	Quantum Fisher information (QFI)

Chapter 1

Introduction

Those things which I am saying now may be obscure, yet they will be made clearer in their proper place.

— Nicolaus Copernicus

The world around us is quantified through measurement. The weather outside is quantified through measurements of temperature and humidity. The brightness of a lightbulb is measured by lumens and the loudness of a motor by decibels. Through these measurements questions of whether today is hotter than yesterday, which lightbulb illuminates a room better, or will this jet engine blow out someone's eardrums can be answered safely.

Here, we will address the measurement of parameters. For the purposes of this thesis, we define a parameter as a property that cannot be directly measured and must be inferred from measurements of observables, *i.e.*, properties that can be directly measured. For example, the color of a brick is an observable while the specific heat of the brick is a parameter that requires a series of measurements in order to calculate it. The parameter we will focus on primarily is transmission. We will show how the measurement of this parameter can be improved by using bright quantum states of light.

Under the assumptions of classical mechanics, it was thought that the uncertainty in a measurement arose only from the instruments and methods used, meaning that an observable, such as the position of particle, has a definite value and any uncertainty in that value must come from the measurement. Therefore, technology should improve to the point that measurements would be perfect, such that no fluctuations in the measurement results would be possible. The development of quantum mechanics showed that this is not the case and that fundamentally there are uncertainties that better engineering or instrumentation cannot remove[1,2]. This quantum mechanical property is limited by the Heisenburg uncertainty principle, which states that the distribution in the measured values of two observables is constrained by the commutablility, *i.e.*, by how much the order of their observation matters.

The lack of commutation of two observables, which is a quantum mechanical effect, can be visualized via the Stern-Gerlach experiment[1–3]. In this experiment, a collimated stream of hot silver atoms is passed through a magnetic field gradient pointed in the vertical or horizontal direction, perpendicular to the flow of atoms. The silver atoms have a single

electron in the outermost shell, which causes the atoms to be deflected either towards or away from the direction of the magnetic field, depending on the direction of the magnetic moment of the electron. For hot silver atoms, half are deflected in each direction due to the quantization of the magnetic moment and the equal probability of having one direction or the other.

Initializing the atoms with a vertical field and following only the upwardly deflected atoms, the initial electron magnetic moment is 'up'. A horizontal field then measures how much of the 'up' magnetic moment is also 'left' or 'right'. It turns out that 'up' contains equal parts of 'left' and 'right' and is thus deflected in both directions. Following the 'right' magnetic moment atomic stream, it is known that the electron was measured to be in the 'up' magnetic moment, as that is the state it was initialized in. However, the electron no longer is in the 'up' state as the horizontal measurement forced it into the 'right' state. Thus, when the vertical component of the magnetic moment is measured again, the 'right' stream splits evenly into a 'right' - 'up' stream and a 'right' - 'down' stream of atoms. The horizontal and vertical components of the magnetic moment cannot both be known simultaneously as measuring one component scrambles the information of the other. Taking the original 'up' atoms and applying a vertical and then horizontal field would lead to 'up' - 'right' and 'up' - 'left' measurement results of equal weight. However, the application of a horizontal field and then a vertical field leads to 'right' - 'up', 'left' - 'up', 'right' - 'down', and 'left' - 'down' of equal proportions. Thus, the order of the measurements changes the measurement results.

The fact that the order of operations in which these two different observations are made haves an effect on the results implies that there is a relationship between the measurements and their commutation. One of these relations is the Heisenburg uncertainty principle, where the minimum uncertainties of the measurements are inversely proportional to each other and constrained by the commutation of the observables,

$$\left\langle \Delta^2 \hat{A} \right\rangle \left\langle \Delta^2 \hat{B} \right\rangle \geq \frac{1}{4} \left| \left\langle \left[\hat{A}, \hat{B} \right] \right\rangle \right|^2, \tag{1.1}$$

where $\hat{A}$ is an observable, $[\hat{A}, \hat{B}] = \hat{A}\hat{B} - \hat{B}\hat{A}$ is the commutation relation, $\langle \hat{A} \rangle$ is the expectation value of the measured observable, and $\langle \Delta^2 \hat{A} \rangle = \langle \left(\hat{A} - \langle \hat{A} \rangle \right)^2 \rangle$ is the variance. This uncertainty relations shows that states generally do not have definite values but a range of simultaneous values with a probability distribution for possible measurement results.

A common example of the uncertainty principle is the position-momentum uncertainty of a particle,

$$\left\langle \Delta^2 \hat{x} \right\rangle \left\langle \Delta^2 \hat{p} \right\rangle \geq \frac{\hbar^2}{4}, \tag{1.2}$$

where $\hat{x}$ is the position operator, $\hat{p}$ is the momentum operator, and $\hbar$ is the reduced Planck constant. If a particle is tightly constrained to a small region, then its momentum must take a large range of values, just as an electron beam or optical laser tightly focused will quickly spread out over a wide area during propagation. As the uncertainty principle only sets the lower bound, the uncertainty of the momentum and position can both be large. The constraint states that a particle cannot have a singular position or a singular momentum.

Measurement of these quantities must have a distribution and cannot return the exact same value every time.

At the same time as the Heisenburg uncertainty principle was being developed, statistical bounds were being found to limit the precision with which a parameter can be estimated. The Fisher information[4], together with the Cramér-Rao bound[5–9], set the lower bound in the uncertainty in estimating the mean value of a parameter given a distribution of measurement results. This bound tells us how well any analysis of a given data set could estimate the value of a parameter, thus stating what the best analysis could achieve.

As an example, let us look at a coin. For 4 flips of a fair coin, one that has an equal chance of getting heads or tails, there is only a 3/8 chance of getting the same number of heads as tails. Thus, it is unlikely to get a measurement result of a fair coin as fair from four flips. To reduce the uncertainty in whether the coin is balanced, this measurement would need to be repeated multiple times. Attaching numbers to the results, we can define tails as -1 and heads as 1 such that a fair coin has a mean of 0. Different numbers of heads and tails from each set of 4 flips are due to the variance of the distribution of results. The fair coin has a variance of 2 for four flips, meaning there is a good chance of having one more heads than tails, or vice versa, of having an equal number of both.

To check if a coin is fair, we need to know the mean value. As stated above, from a single set of 4 flips it is unlikely to get the mean result. In fact, the variance of possible estimated "mean" values from a single set of 4 flips is the same as the variance of 4 flips (2 for a fair coin). However, as we repeat the measurement, the variance of the estimated mean value decreases as there is a similar probability of measuring above or below the mean value. In most cases, the variance of the mean decreases inversely with the number of repeated measurements.

However, is the most precise way to test the fairness of a coin looking at the mean value of many coin tosses? Could counting the number of repeated results such as heads-heads-heads allow for a lower variance of the mean value? To answer these questions, the Cramér-Rao bound sets the lower bound for the variance about the mean for such estimation problems. If an analysis for estimating a value has a variance about the mean equal to the Cramér-Rao bound, it is an optimal estimator that gives the most precise estimation possible from the data.

Returning to quantum mechanics, the Cramér-Rao bound then also limits how well a parameter can be estimated from a set of measurements of the observables. Not only is there a distribution of measurement results due to the state not having a singular value, but there is also a limit to how well the distribution can be characterized from those measurements. Therefore if the state changes, it may not be detectable due to the uncertainty in the mean and other moments of the distribution of the measurements. For example, a small shift in the position of a focused beam of particles may be hard to detect if the shift is smaller than the position distribution.

From these constraints, quantum metrology attempts to find the optimal way to sense small changes in a parameter using quantum mechanics. Typically this involves using a quantum state that has properties that make sensing the parameter of interest easier than it

would be with classical states or quantum measurements, such as photon counting. For this thesis, we will specialize on quantum metrology using quantum states of light and typically, our work is based on Gaussian states of light that can be generated at high powers. The high power allows for even better estimations of parameters, like how flipping the coin more often better resolved the fair or unfair coin. We will focus on estimating transmission through an optical system using these states, but we will briefly cover phase estimation as well.

1.1 Transmission estimation

Transmission estimation is important since every optical system, both quantum and classical, suffers from some amount of loss. Thus, the characterization of any system includes estimating the transmission through it. Losses cause quantum states to transition into classical states, thereby losing quantum properties.

In communication [10–13], the transmission along a channel sets limits on the rate at which information can be sent and how often the signal needs to be amplified. If the transmission is estimated to be higher than it is, this can cause corrupted downloads of data over the internet, inaudible voice chat on phone lines, or, in the extreme case, two parties being unable to communicate at all. If transmission is estimated lower than it is, resources are wasted amplifying the signal and data rates are set too low. To optimize the use of a communication channel, the transmission must be continuously remeasured so that data can be set at the maximum rate possible at any given time and minimum resources are used to amplify the signal. Transmission estimation also needs to be done quickly, such that the measurement does not overtly interfere with the communications.

In other sensing applications, the transmission of the sensing device needs to be taken into account when generating an initial optical state. For interferometers used to measure the phase difference between two arms of the device, a difference in transmission between the arms can cause a calibration error in the phase estimation. Since the power of the output of the interferometer is used to measure phase, a drop in transmission can be misinterpreted as a change in phase. For interferometers enhanced with quantum states of light [14], losses can reduce the advantage of quantum states over classical ones and, in the worst case, the quantum state can actually become worse than a classical state for phase estimation. In certain cases, the quantum state that gives the greatest improvement in the phase estimation is determined by the amount of loss in the interferometer [14].

Transmission is also used in resonance sensors [15,16], such as a plasmonic sensor [17,18] for which a local change in the refractive index causes a change in the transmission. These sensors can be used to measure air purity, pressure, or the temperature of an object. They can also be used in medical applications to detect the presence of certain proteins used as markers for various diseases and other biological markers.

Much work has been done in order to improve the calibration or sensing of transmission using quantum states of light [19–23]. The theoretical limit in the uncertainty in the estimation of transmission is known to be reached by certain low power quantum states of light [20,21]. However, the uncertainty scales inversely with power and thus the lower power quantum

states have limited applicability. Only when studying transmissive systems with very low damage thresholds, on the order of a few photons per second, can these optimal quantum states be beneficial. For this thesis, we will use a bright, high power quantum state that can estimate transmission better than classical states and, under certain conditions, can reach the same theoretical limit as the aforementioned optimal low power states. These bright quantum states expand the applicability of quantum enhanced transmission estimation by being generated with power comparable to many classical estimation schemes.

Recent experiments with quantum states of light to estimate transmission have shown an enhancement [24–28]. However, none of them have reported uncertainties in the estimation at the fundamental limit. In certain cases, this is due to how the data was analyzed [24–27] and in others it is due to not having enough control over their experiment to keep from adding additional sources of uncertainty into the estimation [28].

1.2 Outline

The chapters are broken up as follows. Chapter 2 introduces Gaussian states of light and the properties and representations of these states. In Chapter 3, the Fisher information and Cramér-Rao bound are introduced, as well as the quantum mechanical expansions of each. The original work I focused on as part of my dissertation starts in Chapter 4, which explains the theory of transmission estimation with Gaussian states of light. My experimental work that confirms the theory is presented in Chapter 5. Chapter 6 expands on the previous transmission theory to compare transmission estimation to phase estimation in the context of a resonance sensor. Finally, Chapter 7 concludes with an overview of the work as well as possible future expansions of it.

Part I

Background Information

Chapter 2

Gaussian States of Light

In quantum theory, light is quantized into wavepackets called photons. Each photon is a particle and a wave. For a state of light, it is difficult to describe, or achieve an intuitive understanding of, the wave and particle nature of the state with a single representation. Here, we will cover different states of light using different representations to build an understanding of the relevant properties of the light used in this thesis. However, the light must first be quantized.

For light in a finite volume V, the vector potential $\vec{A}$ of the electromagnetic (EM) wave must satisfy the wave equation

$$\nabla^2 \vec{A} + \frac{1}{c^2}\frac{\partial^2 \vec{A}}{\partial t^2} = 0. \tag{2.1}$$

The vector potential can be written as[29,30]

$$\vec{A} = c\sum_k \frac{1}{\sqrt{2\omega_k}} \left[\vec{u}_k(\vec{r})\alpha_k(t) + \vec{u}_k^*(\vec{r})\alpha_k^*(t)\right], \tag{2.2}$$

where k labels the specific mode or solution to the wave equation, $\vec{u}_k(\vec{r})$ are the spatial mode functions that satisfy the boundary conditions of the wave equation, $\alpha_k(t)$ are the temporal mode functions, and ω_k is the angular frequency of the EM wave. Using the Coulomb gauge, $\nabla \cdot \vec{A} = 0$, and assuming a square volume with periodic boundary conditions, the mode functions can be solved such that

$$\vec{u}_k(\vec{r}) = \sqrt{\frac{1}{V}}\vec{\varepsilon}_p(\vec{k})e^{-i\vec{k}\cdot\vec{r}} \tag{2.3}$$

and

$$\alpha_k(t) = \alpha_k e^{i\omega_k t}, \tag{2.4}$$

where $\vec{\varepsilon}_p(\vec{k})$ is the polarization vector of the wave, $\vec{k}$ is the wave vector or momentum of the light, and $\omega_k = c|\vec{k}|$. The vector potential can now be written as

$$\vec{A} = \sum_k \sqrt{\frac{c}{2|\vec{k}|V}}\vec{\varepsilon}_p(\vec{k})\left(\alpha_k e^{-i\left(\vec{k}\cdot\vec{r}-\omega_k t\right)} + \alpha_k^* e^{i\left(\vec{k}\cdot\vec{r}-\omega_k t\right)}\right). \tag{2.5}$$

The vector potential can be quantized by setting $\alpha_k \to \sqrt{\hbar}\hat{a}_k$ [29,30], such that

$$\vec{\hat{A}} = \sum_k \sqrt{\frac{c\hbar}{2|\vec{k}|V}} \vec{\varepsilon}_p(\vec{k}) \left(\hat{a}_k e^{-i(\vec{k}\cdot\vec{r}-\omega_k t)} + \hat{a}_k^\dagger e^{i(\vec{k}\cdot\vec{r}-\omega_k t)} \right), \tag{2.6}$$

where $\hat{a}_k^\dagger$ is the Hermition conjugate of $\hat{a}_k$. These field operators are called the creation, $\hat{a}_k^\dagger$, and annihilation, $\hat{a}_k$, operators as they create or destroy a photon in the corresponding mode of the field, respectively. A quadrature operator $\hat{Q}$ can be defined for an arbitrary phase, γ, as

$$\hat{Q}(\gamma) = \hat{a}e^{-i\gamma} + \hat{a}^\dagger e^{i\gamma}, \tag{2.7}$$

such that the quantized vector potential of a single mode, such that we can drop the k subscript, can be written as

$$\vec{\hat{A}} = \sqrt{\frac{c\hbar}{2|\vec{k}|V}} \vec{\varepsilon}_p(\vec{k}) \hat{Q}(\vec{k}\cdot\vec{r} - \omega t), \tag{2.8}$$

such that it contains only one operator.

The state that most resembles the classical model of an electromagnetic (EM) wave is the coherent state $|\alpha\rangle$, which satisfies $\hat{a}\,|\alpha\rangle = \alpha\,|\alpha\rangle$. The expectation value of the vector potential of a coherent state is

$$\langle\alpha|\,\hat{A}(\gamma)\,|\alpha\rangle = \sqrt{\frac{c\hbar}{2|\vec{k}|V}} \vec{\varepsilon}_p(\vec{k}) \left(\alpha e^{-i\gamma} + \alpha^* e^{i\gamma}\right) \tag{2.9}$$

such that in the classical limit of $\hbar = 1$, the expectation value of the vector potential exhibits the same behavior as in classical theory. This can also be seen by comparing Eq. (2.5) and Eq. (2.9) as the expectation values of quantum operators correspond to their classical counterparts.

For the particle nature of light, let us look at the energy of the EM wave. The classical Hamiltonian is given by [29,30]

$$H = \frac{1}{2}\int_V \left(|\vec{E}|^2 + |\vec{B}|^2\right) d^3\vec{r}, \tag{2.10}$$

where $\vec{E}$ is the electric field and $\vec{B}$ is the magnetic field. These fields can be obtained from the vector potential via

$$\vec{E} = -\frac{1}{c}\frac{\partial \vec{A}}{\partial t} \tag{2.11}$$

$$\vec{B} = \nabla \times \vec{A} \tag{2.12}$$

and thus the Hamiltonian can be shown to take the form [29,30]

$$H = \omega|\alpha|^2. \tag{2.13}$$

Quantizing the field with $\alpha \to \sqrt{\hbar}\hat{a}$ gives the Hamiltonian operator

$$\hat{H} = \hbar\omega\frac{\hat{a}^\dagger\hat{a} + \hat{a}\hat{a}^\dagger}{2} \tag{2.14}$$

$$= \hbar\omega(\hat{n} + 1/2), \tag{2.15}$$

where $\hat{n} = \hat{a}^\dagger\hat{a}$ is the number operator and due to the noncommutativity of the field operators, $[\hat{a}, \hat{a}^\dagger] = 1$, we have symmetrized the ordering. Now the energy of the EM wave is quantized by the number of photons in the state and increasing or decreasing the energy can only be done in steps of $\hbar\omega$ by adding or subtracting photons, respectively.

The state that most exemplifies this property is the Fock state. This state, also known as the number state, has an exact number of photons n. It is written as $|n\rangle$ and has mean energy

$$\langle n|\,\hat{H}\,|n\rangle = (n + 1/2)\hbar\omega \tag{2.16}$$

with no variance

$$\left\langle \Delta^2\hat{H} \right\rangle = \langle n|\,\hat{H}^2\,|n\rangle - \left(\langle n|\,\hat{H}\,|n\rangle\right)^2 = 0. \tag{2.17}$$

This purely quantum state is only defined by the number of photons and has no classical analog since it has no mean vector potential

$$\langle n|\,\hat{A}(\gamma)\,|n\rangle = 0, \tag{2.18}$$

and is not the vacuum state of no photons, $|0\rangle$. This state exemplifies the particle nature of light. Being only of the particle nature, it cannot be described using the classical EM wave theory.

Due to the wave-particle nature of light, an arbitrary state is not easily understood by looking solely at the wave nature, $\hat{A}(\gamma)$, or particle nature, $\hat{H}$, of the light. While a state can be fully described via either one, it is not always intuitive to do so. For transmission estimation, it is easier to understand the underlying physics by examining the particle nature of states of light used to probe the system under study. The calculations that are introduced in the next chapter are, however, simpler to do using the wave nature.

2.1 Representations of states

To represent the states used in this thesis, we will use two forms. The first is the representation in the Fock basis where any arbitrary state $|\Psi\rangle$ can be written as a superposition of Fock states[29,30]

$$|\Psi\rangle = \sum_n \psi_n\,|n\rangle\,, \tag{2.19}$$

with $\psi_n = \langle n|\Psi\rangle$ and $\sum_n |\psi_n|^2 = 1$. This representation, along with the mean and variance of the number operator, is used to explore the particle nature of the state. The second representation is based on the quadrature measurements, which will be expanded upon here before examining the states of light used in this thesis.

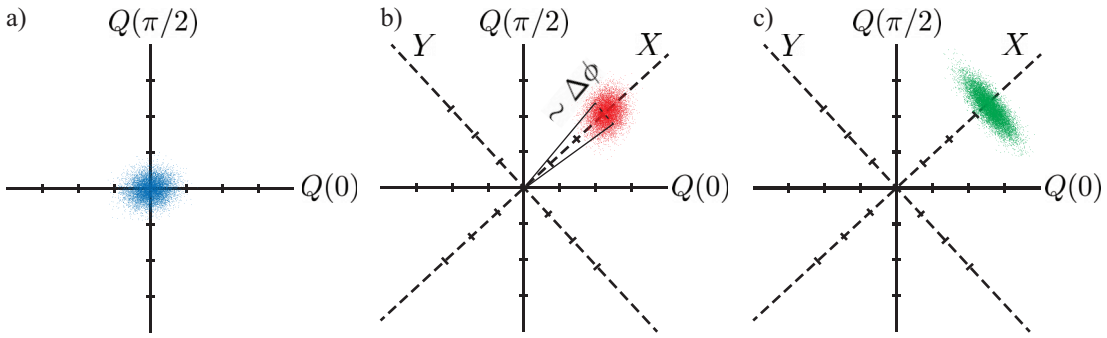


Figure 2.1: Phase space representations of a vacuum state a) in blue, coherent state b) in red, and a squeezed state c) in green in quadrature space. For the coherent and squeezed states, a quadrature $\hat{X}$ can be defined along the direction of the offset, or displacement, from zero and, for large displacement, along the direction of phase rotation, $\hat{Y}$.

For the coherent state, the expectation value of an arbitrary quadrature takes the form

$$\left\langle \hat{Q}(\gamma) \right\rangle = 2|\alpha| \cos(\chi - \gamma), \tag{2.20}$$

where $\chi = \arg(\alpha)$ is the phase of α. Plotting the quadrature distribution of a state in a phase space diagram, Fig. 2.1, we can see that by setting $\gamma = \chi$ the quadrature measurement is along the direction of the amplitude of the EM wave, Fig. 2.1(b), and thus is called the amplitude quadrature. In the conjugate direction, $\gamma = \chi + \pi/2$, and for sufficiently large amplitudes, $\langle \hat{Q}(\chi) \rangle \gg \langle \Delta^2 \hat{Q}(\chi + \pi/2) \rangle$, the $\hat{Q}(\chi + \pi/2)$ quadrature measurement points in the direction of phase rotation for the state and the variance of this quadrature is equivalent to the variance of the phase of the EM wave, using the small angle approximation. Thus, this quadrature is called the phase quadrature. For simplicity, we shall limit our discussion of quadratures to the amplitude quadrature, $\hat{X}$, and phase quadrature, $\hat{Y}$, whenever possible instead of the general quadrature measurement.

Certain states have a probability distribution in quadrature space that is Gaussian, *i.e.* they can be fully described by the mean and variance of the quadrature observables[31]. Gaussian states can thus be fully characterized by their covariance matrix, $\boldsymbol{\sigma}$, and displacement vector, $\vec{d}$, which are defined as[32]

$$\begin{aligned}
\vec{d} &= \langle \hat{\mathbb{A}} \rangle, && (2.21)\\
\sigma_{i,j} &= \left\langle \{ \hat{\mathbb{A}}_i - d_i, \hat{\mathbb{A}}_j^\dagger - d_j^* \} \right\rangle && (2.22)\\
&= \left\langle \hat{\mathbb{A}}_i \hat{\mathbb{A}}_j^\dagger + \hat{\mathbb{A}}_j^\dagger \hat{\mathbb{A}}_i \right\rangle - 2 \left\langle \hat{\mathbb{A}}_i \right\rangle \left\langle \hat{\mathbb{A}}_j^\dagger \right\rangle && (2.23)\\
&\equiv 2\,\mathrm{Cov}(\hat{\mathbb{A}}_i, \hat{\mathbb{A}}_j^\dagger), && (2.24)
\end{aligned}$$

where Cov is the covariance, $\hat{\mathbb{A}} = (\hat{a}_1, ..., \hat{a}_k, \hat{a}_1^\dagger, ..., \hat{a}_k^\dagger)^T$ is a column matrix of annihilation and creation operators for k photonic modes of the state with the superscript T representing the transpose operation, and $\{\hat{A}, \hat{B}\} = \hat{A}\hat{B} + \hat{B}\hat{A}$ is the anti-commutation relation. These

are the complex forms of the covariance matrix and displacement as they look at the field operators, $\hat{a}$ and $\hat{a}^\dagger$, instead of the $\hat{X}$ and $\hat{Y}$ quadratures used in the real forms. We use the complex form as it is useful later when finding limits in precision for parameter estimation. To compare between the two forms, the diagonal of the complex covariance matrix corresponds to the mean quadrature variance

$$\sigma_{i,i} = \left\langle \hat{a}_i \hat{a}_i^\dagger + \hat{a}_i^\dagger \hat{a}_i \right\rangle - 2 \left\langle \hat{a}_i \right\rangle \left\langle \hat{a}_i^\dagger \right\rangle = \frac{\left\langle \Delta^2 \hat{X}_i \right\rangle + \left\langle \Delta^2 \hat{Y}_i \right\rangle}{2} \tag{2.25}$$

and the off-diagonal terms arise from the asymmetry of the uncertainty

$$\sigma_{i,i+k} + \sigma_{i+k,i} = \left\langle \Delta^2 \hat{Q}_i(0) \right\rangle - \left\langle \Delta^2 \hat{Q}_i(\pi/2) \right\rangle \tag{2.26}$$

for $i \leq k$, and the argument, $\arg(\sigma_{i,i+k})$, gives the direction of the asymmetry. Where the asymmetry comes from and what all these terms mean will become clearer in the next section where we talk about various Gaussian states of light that are important for this thesis.

2.2 Gaussian states of light

As stated above, Gaussian states of light can be fully described by the mean and covariance of the field operators. As such, we can use the covariance matrix and displacement vector introduced in the last section to represent these states. In this section, we will show how this is done for various states and also go over their Fock basis representation.

2.2.1 Vacuum and coherent states

The vacuum state has a wave function in the Fock basis of $|0\rangle$ as it has, as the name implies, no photons. However, as shown in Fig. 2.1(a), this state still has quadrature noise,

$$\left\langle \Delta^2 \hat{Q}(\gamma) \right\rangle = 1, \tag{2.27}$$

as even the vacuum has EM fluctuations. This comes from the commutation relation of the quadrature observables

$$[\hat{X}, \hat{Y}] = 2i, \tag{2.28}$$

such that the Heisenburg uncertainty relation, see Eq. (1.1), gives

$$\left\langle \Delta^2 \hat{X} \right\rangle \left\langle \Delta^2 \hat{Y} \right\rangle \geq 1. \tag{2.29}$$

Thus, no matter the state, even vacuum, there are still fluctuations of the EM field. This can be also seen from the Hamiltonian introduced in Eq. (2.15), where the extra $\frac{1}{2}\hbar\omega$ in $\hat{H} = \hbar\omega(\hat{n} + 1/2)$ gives the energy of these vacuum fluctuations.

Writing the vacuum state in the covariance matrix form, the displacement vector is $\begin{pmatrix}0 & 0\end{pmatrix}^T$ due to having zero mean amplitude. However, the covariance matrix, much like the quadrature variance, is not zero as

$$\boldsymbol{\sigma} = \begin{pmatrix}1 & 0\\ 0 & 1\end{pmatrix} = \mathrm{diag}(1,1). \tag{2.30}$$

From Eq. (2.27), it is known that all the quadrature measures have an equal variance of 1. Thus the diagonal of the vacuum state covariance matrix is 1 and the off diagonal terms are zero as the noise is equal in all directions.

A coherent state, the state that most resembles a classical EM wave, is generated by displacing the vacuum state such that the displacement vector is

$$\vec{d} = \begin{pmatrix}\alpha\\ \alpha^*\end{pmatrix}. \tag{2.31}$$

The covariance matrix of the coherent state is the same as the vacuum state, $\mathrm{diag}(1,1)$, as it is only the displacement of the vacuum state, *i.e.* shift the quadrature distribution from Fig. 2.1(a) to Fig. 2.1(b). Thus, the coherent state also has equal noise in every quadrature. As it is at the Heisenberg uncertainty limit, this state is also known as the minimum uncertainty classical state.

The dispacement is done using the displacement operator [29,30]

$$\hat{D}(\alpha) = e^{\alpha\hat{a}^\dagger - \alpha^*\hat{a}}, \tag{2.32}$$

which creates a coherent state wavefunction when applied to the vacuum [30]

$$|\alpha\rangle = \hat{D}(\alpha)\,|0\rangle = e^{-\frac{|\alpha|^2}{2}} \sum_{n=0}^{\infty} \frac{\alpha^n}{\sqrt{n!}}\,|n\rangle\,. \tag{2.33}$$

The number of photons in a coherent state has a Poisson distribution, or random distribution

$$P(n) = |\,\langle n|\alpha\rangle\,|^2 = e^{-|\alpha|^2}\frac{|\alpha|^{2n}}{n!}, \tag{2.34}$$

where $P(n)$ is the probability of detecting n photons. Detection of these states with a photon counting or intensity measurement has a 'shot noise' variance. This variance changes linearly with the mean number of photons of the state, $\langle\Delta^2\hat{n}\rangle = \langle\hat{n}\rangle = |\alpha|^2$ and comes from the particle nature, and distribution, of the photons.

2.2.2 Squeezed states

As seen in Eq. (2.27), there are always fluctuations of the field, even in vacuum. The vacuum and coherent states have a symmetric uncertainty in $\langle\Delta^2\hat{X}\rangle = \langle\Delta^2\hat{Y}\rangle = 1$. This is the minimum quadrature variance a classical state can have and is called the quantum

noise limit (QNL). Only quantum states, such as squeezed states, can have the noise in one quadrature lower than the QNL, though at the expense of increased noise in another quadrature. For squeezed states it is possible to have a phase space distribution as shown in Fig 2.1(c) where

$$\left\langle \Delta^2 \hat{X} \right\rangle = e^{-2s} \tag{2.35}$$

$$\left\langle \Delta^2 \hat{Y} \right\rangle = e^{2s}, \tag{2.36}$$

and $s \geq 0$ is the squeezing parameter. Given the direction of squeezing, the amplitude noise in this example is reduced below the QNL at the expense of the phase noise. Whenever one quadrature is squeezed, the other must be anti-squeezed, due to the Heisenberg uncertainty principle, Eq. (2.29).

A state is squeezed using the squeezing operator [29,30]

$$\hat{S}(\xi) = e^{\frac{1}{2}\left[\xi(\hat{a}^\dagger)^2 - \xi^* \hat{a}^2\right]}, \tag{2.37}$$

where $\xi = se^{i\theta}$ and θ is the angle of squeezing which sets the quadrature which has reduced variance and which has increased variance, *i.e.* the angle of the ellipse Fig. 2.1(c). Squeezing the vacuum state generates the wavefunction [30]

$$\hat{S}(\xi)\left|0\right\rangle = \frac{1}{\sqrt{\cosh(s)}} \sum_{n=0}^{\infty} \frac{[(2n)!]}{2^n n!} [e^{i\theta} \tanh(s)]^n \left|2n\right\rangle, \tag{2.38}$$

a state which is called the vacuum single mode squeezed state (vSMSS). As can be seen from the ket on the right hand side, this state is a superposition of only Fock states with even number of photons. This is due to the nonlinearity of the squeezer, Eq. (2.37), where the photon creation and annihilation operators are squared. Thus photons are always created and destroyed simultaneously in pairs. Due to this, the photon number variance for this state is greater than that of a coherent state, $\langle \Delta^2 \hat{n} \rangle = 2 \langle \hat{n} \rangle (\langle \hat{n} \rangle + 1)$, even though there is reduced noise in a quadrature.

The covariance matrix for this state is given by

$$\boldsymbol{\sigma} = \begin{pmatrix} \cosh(2s) & -e^{i\theta}\sinh(2s) \\ -e^{-i\theta}\sinh(2s) & \cosh(2s) \end{pmatrix}. \tag{2.39}$$

Here, the diagonal terms are greater than those for the coherent state as the average quadrature noise has increased, but there are non-zero off diagonal terms due to the asymmetry of the quadrature noise of the state. Only the variances in the quadrature along and perpendicular to the squeezing direction saturate the Heisenberg uncertainty relation as the average variance has increased. The argument of the off diagonal term, θ, gives the angle of squeezing, while the magnitude of the term alludes to the amount of squeezing as the amount of imbalance between the quadrature variances increases with squeezing. Squeezing a displaced state gives a displacement vector of

$$\vec{d} = \begin{pmatrix} \alpha\cosh(s) - \alpha^* e^{i\theta}\sinh(s) \\ \alpha^*\cosh(s) - \alpha e^{-i\theta}\sinh(s) \end{pmatrix}, \tag{2.40}$$

and the same covariance matrix as the vSMSS. Depending on the angle of squeezing, the displacement, and therefore the amplitude as well as the photon number, can either be amplified or attenuated. Squeezing a state where the displacement is much greater than the quadrature variance creates a bright single mode squeezed state (bSMSS). An amplitude quadrature that is squeezed leads to a sub-Poisson distribution of the photon number, such that the variance is less than that of a coherent state,

$$\begin{aligned}\left\langle \Delta^2 \hat{n} \right\rangle &= \langle\alpha| \hat{S}^\dagger \hat{n}^2 \hat{S} |\alpha\rangle - \langle\alpha| \hat{S}^\dagger \hat{n} \hat{S} |\alpha\rangle^2 && (2.41)\\ &= \langle\alpha| (\hat{S}^\dagger \hat{a}^\dagger \hat{S})(\hat{S}^\dagger a \hat{S})(\hat{S}^\dagger a^\dagger \hat{S})(\hat{S}^\dagger a \hat{S}) |\alpha\rangle - \langle\alpha| (\hat{S}^\dagger \hat{a}^\dagger \hat{S})(\hat{S}^\dagger \hat{a} \hat{S}) |\alpha\rangle^2 && (2.42)\\ &= \langle \hat{n} \rangle e^{-2s}, && (2.43)\end{aligned}$$

where we have used the unitary property $\hat{S}\hat{S}^\dagger = \mathbb{I}$, where $\mathbb{I}$ is the identity matrix, and the transform $\hat{S}^\dagger \hat{a} \hat{S} = \hat{a}\cosh(s) - \hat{a}^\dagger e^{i\theta}\sinh(s)$. However, if the phase quadrature is squeezed the number variance is higher, $\langle \Delta^2 \hat{n} \rangle = \langle \hat{n} \rangle e^{2s}$.

2.2.3 Two mode squeezed states

Gaussian states are not limited to a single mode and can be split into multiple modes characterized by different polarizations, propagation directions, or frequencies. For instance, the squeezing operation can be done over two modes, which correlates the quadrature fluctuations of the two modes to reduce the variance in the sum or difference amplitude or phase quadrature, or some other combination of quadratures. For example, if given two modes, the probe mode indicated by the subscript p and the conjugate mode with subscript c, the sum and difference variances of the amplitude and phase quadratures can be

$$\begin{aligned}\left\langle \Delta^2 \left(\hat{X}_p - \hat{X}_c \right) \right\rangle &= 2e^{-2s} && (2.44)\\ \left\langle \Delta^2 \left(\hat{X}_p + \hat{X}_c \right) \right\rangle &= 2e^{2s} && (2.45)\\ \left\langle \Delta^2 \left(\hat{Y}_p - \hat{Y}_c \right) \right\rangle &= 2e^{2s} && (2.46)\\ \left\langle \Delta^2 \left(\hat{Y}_p + \hat{Y}_c \right) \right\rangle &= 2e^{-2s}, && (2.47)\end{aligned}$$

while the variance of any quadrature of a single mode is greater than that of a coherent state, *i.e.* $\langle \Delta^2 \hat{X}_p \rangle > 1$. The QNL for the sum and difference quadratures, as can be seen by setting $s = 0$ above, is 2 and only quantum states are able to have a smaller quadrature uncertainty. It should also be noted that the difference in one quadrature commutes with the sum in the conjugate quadrature,

$$\left[\left(\hat{X}_p - \hat{X}_c \right), \left(\hat{Y}_p + \hat{Y}_c \right) \right] = 0, \quad (2.48)$$

and therefore both of these variances can be reduced simultaneously.

The two mode squeezing operation [29,30],

$$\hat{S}_{p,c}(\xi) = e^{\xi \hat{a}_p^\dagger \hat{a}_c^\dagger - \xi^* \hat{a}_p \hat{a}_c}, \quad (2.49)$$

generates a pair of photons simultaneously in two separate modes with one photon in what we call the probe mode and the other in what we call the conjugate mode. This operator transforms the field operators as

$$\hat{S}^{\dagger}_{p,c}\hat{a}_p\hat{S}_{p,c} = \hat{a}_p\cosh(s) - \hat{a}^{\dagger}_c e^{i\theta}\sinh(s) \tag{2.50}$$

$$\hat{S}^{\dagger}_{p,c}\hat{a}_c\hat{S}_{p,c} = \hat{a}_c\cosh(s) - \hat{a}^{\dagger}_p e^{i\theta}\sinh(s). \tag{2.51}$$

Using this transform, the covariance matrix of this state can be found to be

$$\boldsymbol{\sigma} = 2\begin{pmatrix} \mathrm{Cov}(\hat{a}_p,\hat{a}^{\dagger}_p) & \mathrm{Cov}(\hat{a}_p,\hat{a}^{\dagger}_c) & \mathrm{Cov}(\hat{a}_p,\hat{a}_p) & \mathrm{Cov}(\hat{a}_p,\hat{a}_c) \\ \mathrm{Cov}(\hat{a}_c,\hat{a}^{\dagger}_p) & \mathrm{Cov}(\hat{a}_c,\hat{a}^{\dagger}_c) & \mathrm{Cov}(\hat{a}_c,\hat{a}_p) & \mathrm{Cov}(\hat{a}_c,\hat{a}_c) \\ \mathrm{Cov}(\hat{a}^{\dagger}_p,\hat{a}^{\dagger}_p) & \mathrm{Cov}(\hat{a}^{\dagger}_p,\hat{a}^{\dagger}_c) & \mathrm{Cov}(\hat{a}^{\dagger}_p,\hat{a}_p) & \mathrm{Cov}(\hat{a}^{\dagger}_p,\hat{a}_c) \\ \mathrm{Cov}(\hat{a}^{\dagger}_c,\hat{a}^{\dagger}_p) & \mathrm{Cov}(\hat{a}^{\dagger}_c,\hat{a}^{\dagger}_c) & \mathrm{Cov}(\hat{a}^{\dagger}_c,\hat{a}_p) & \mathrm{Cov}(\hat{a}^{\dagger}_c,\hat{a}_c) \end{pmatrix} \tag{2.52}$$

$$= \begin{pmatrix} \cosh(2s) & 0 & 0 & -e^{i\theta}\sinh(2s) \\ 0 & \cosh(2s) & -e^{i\theta}\sinh(2s) & 0 \\ 0 & -e^{-i\theta}\sinh(2s) & \cosh(2s) & 0 \\ -e^{-i\theta}\sinh(2s) & 0 & 0 & \cosh(2s) \end{pmatrix}. \tag{2.53}$$

For the single mode squeezed state the off diagonal terms of the covariance of the field operator with itself are non-zero, as the single mode quadratures are squeezed. For the two mode squeezed state, the off diagonal covariance terms are only present between the two fields as photons are being generated or annihilated together. The covariance terms of $\hat{a}_p$ and $\hat{a}_c$ and $\hat{a}^{\dagger}_p$ and $\hat{a}^{\dagger}_c$ are non-zero, while the covariance terms of $\hat{a}_p$ and $\hat{a}^{\dagger}_c$ are zero. This gives the sum and difference quadrature squeezing. At the same time, the probe or conjugate quadratures have symmetric noise as, unlike the single mode squeezing case, there is zero covariance of $\hat{a}_{p,c}$ or $\hat{a}^{\dagger}_{p,c}$ with itself. This is due to the photon pairs now being generated in separate modes instead of in the same mode.

Applying the squeezing operator on the vacuum state creates the vacuum two-mode squeezed state (vTMSS) with wavefunction [30]

$$\hat{S}_{p,c}(\xi)\left|0\right\rangle_p\left|0\right\rangle_c = \frac{1}{\cosh(s)}\sum_{n=0}^{\infty} e^{in\theta}\left[\tanh(s)\right]^n\left|n\right\rangle_p\left|n\right\rangle_c. \tag{2.54}$$

Like the vSMSS, the vTMSS contains only even numbers of photons but these photons are split between the two modes. As such, the intensity difference between the two modes of the vTMSS has zero variance, $\langle\Delta^2\left(\hat{n}_p - \hat{n}_c\right)\rangle = 0$, as the photons in each mode are simultaneously generated in pairs and therefore are perfectly correlated.

Squeezing the two modes after displacement, α for the probe mode and β for the conjugate mode, results in the state

$$\hat{S}_{p,c}(\xi)\hat{D}_p(\alpha)\hat{D}_c(\beta)\left|0\right\rangle_p\left|0\right\rangle_c = \left|\alpha,\beta;\xi\right\rangle_{p,c}, \tag{2.55}$$

which can generate a bright two mode squeezed state (bTMSS) if the displacement is sufficiently large. This state has a displacement vector of

$$\vec{d} = \begin{pmatrix} \alpha\cosh(s) - \beta^* e^{i\theta}\sinh(s) \\ \beta\cosh(s) - \alpha^* e^{i\theta}\sinh(s) \\ \alpha^*\cosh(s) - \beta e^{-i\theta}\sinh(s) \\ \beta^*\cosh(s) - \alpha e^{-i\theta}\sinh(s) \end{pmatrix} \tag{2.56}$$

and no change to the covariance matrix from the state without displacement, just like for the single mode squeezed state. The bTMSS has more photons in each mode than the vTMSS due to the displacement but at the expense of increased intensity difference noise, $\langle \Delta^2 (\hat{n}_p - \hat{n}_c) \rangle = |\alpha|^2 + |\beta|^2$ when the amplitude difference quadrature is squeezed or only a single mode is displaced, $\alpha\beta = 0$. Physically, this excess noise and increased power is due to stimulating the squeezing process using coherent light. The generated photons are perfectly correlated but the correlations of the initial coherent states cannot increase, so the photons from those modes remain uncorrelated and the variances from each state add together. As explained in the next section, each mode of the two-mode squeezed state by itself is a thermal state, or displaced thermal state for the bTMSS, and only together do the modes have reduced noise properties, as compared to coherent states.

2.2.4 Thermal state and density matrices

A thermal state is a classical state of light generated as an incoherent mixture of photons. As such, this state cannot be written as a superposition of Fock states as it has a definite but as of yet unknown number of photons. This is a subtle but significant difference from a coherent state, which is in a coherent superposition of different Fock states and collapses to one of them upon measurement. The thermal state is in an ensemble of Fock states. Like colored marbles in a bag, it is unknown which one is grabbed until it is pulled out and observed but the marble is not in a superposition of different colors.

To describe a thermal state we need to use a density matrix[33,34], ρ, which allow us to combine classical probability, *i.e.* marbles in a bag, with quantum superpositions. A wavefunction of the states discussed previously, known as pure states in this notation, can be written as a density matrix by writing it as an outer product with itself, for example the coherent state has a density matrix of

$$\rho_{\text{coh}} = |\alpha\rangle\langle\alpha| \,, \tag{2.57}$$

as there is a 100% probability of finding the state as a coherent state. Formally, a density matrix is an operator and is written as $\hat{\rho}$, but for this thesis we drop the hat. For a state that has a 50% probability of being a coherent state and 50% probability of being in a vacuum state, the density matrix is written as

$$\rho = \frac{1}{2}|\alpha\rangle\langle\alpha| + \frac{1}{2}|0\rangle\langle 0| \tag{2.58}$$

and is known as a mixed state as it requires a mix of classical probability to fully describe. The thermal state has a density matrix of the form [30]

$$\rho_{\text{th}} = \frac{1}{1+\bar{n}} \sum_{n=0}^{\infty} \left(\frac{\bar{n}}{1+\bar{n}} \right)^n |n\rangle\langle n| \,, \tag{2.59}$$

where $\bar{n} = \langle \hat{n} \rangle$ is the mean number of photons. The thermal state has a super-Poisson distribution of photons with a number variance of $\langle \Delta^2 \hat{n} \rangle = \bar{n}\,(\bar{n}+1)$. The quadrature noise for the thermal state is symmetric like the coherent state except that it has a higher uncertainty,

$$\left\langle \Delta^2 \hat{Q}(\gamma) \right\rangle = 2\bar{n} + 1. \tag{2.60}$$

The state has a quadrature mean of zero as the photon generation for a thermal state is not coherent and thus the temporal phase of each photon is random, scrambling the EM wave. The covariance matrix for the state is

$$\boldsymbol{\sigma} = \begin{pmatrix} 2\bar{n}+1 & 0 \\ 0 & 2\bar{n}+1 \end{pmatrix} \tag{2.61}$$

and the state, due to the incoherence of the photon phases, has zero displacement.

For the vTMSS, if one of the modes was not measured or lost, the remaining mode would have a covariance matrix of the form

$$\begin{aligned} \boldsymbol{\sigma} &= \begin{pmatrix} \cosh^2(s) + \sinh^2(s) & 0 \\ 0 & \cosh^2(s) + \sinh^2(s) \end{pmatrix} && (2.62) \\ &= \begin{pmatrix} 2\bar{n}+1 & 0 \\ 0 & 2\bar{n}+1 \end{pmatrix}, && (2.63) \end{aligned}$$

since $\langle \hat{n}_p \rangle = \langle \hat{n}_c \rangle = \sinh^2(s) = \cosh^2(s) - 1$. For the bTMSS, the remaining mode would be a displaced thermal state. It is important to keep this in mind when discussing quantum metrology using two mode squeezed states, as the quantum advantage from using these states disappears when losses are too high. This is due to the states tending towards thermal states, which have variances much higher than the QNL.

Chapter 3

Parameter Estimation Limits: The Cramér-Rao Bound and Fisher Information

As mentioned in the introduction, we define a parameter as a property of a system or state that does not have an associated observable. Using this definition, energy is not a parameter as it is given by the mean of the Hamiltonian, $\hat{H}$, but properties like transmission and phase are, as they cannot be measured directly and must be inferred by the results of other measured observables. Since parameters cannot be directly measured, how to best estimate their values is an area of active research. The best estimation of a parameter is the one that has the smallest uncertainty in the estimated mean value.

Precise, low uncertainty, estimations of parameters are used in sensing applications and the testing of fundamental physics. An example from fundamental physics is the measurement of the fine structure constant. Measuring a value different than what is predicted by the standard model in particle physics would point to potential model improvements[35]. In sensing, a famous example is the Laser Interferometer Gravitational-Wave Observatory (LIGO) that uses a change in the geometric phase between the two arms of the interferometer to detect gravitational waves[36]. Precise phase estimation allows for the detection of weaker signals and therefore allows for the detection of more instances of gravitational disturbances. In this chapter we will discuss the general framework for parameter estimation and give bounds for the minimum estimation uncertainty.

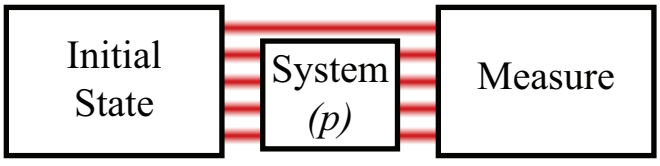


Figure 3.1: Block diagram of the three parts of parameter estimation. A state of light is prepared with one or more modes. At least one mode interacts with the system under study that contains the parameter of interest, p. Measurements are done on the light after interaction with the system to estimate the parameter value.

As shown in Fig. 3.1, parameter estimation involves three main components: a system under study whose response depends on the parameter of interest; a state, optical for this thesis, to interact with the system; and a measurement of the state to extract the information needed to estimate the parameter value. For a measurement M, the uncertainty in the value of the parameter p is given by error propagation of the measurement uncertainty into uncertainty of the parameter value[37]

$$\langle \Delta^2 p \rangle = \left| \frac{\partial M}{\partial p} \right|^{-2} \langle \Delta^2 M \rangle , \tag{3.1}$$

where $\langle \Delta^2 M \rangle$ is the variance of the measurement and $\frac{\partial M}{\partial p}$ is the rate of change, or slope, of the mean value of the measurement for changes in the parameter. To reduce the uncertainty in the parameter, either the measurement uncertainty must decrease or there must be a large change of the measurement results for small changes in the parameter value. The larger the slope and the smaller the spread of measurement results, the smaller the changes in the parameter that can be detected. Ideally, a change from an initial parameter value to a new value would have no overlap of measurement results from the initial value. This allows for different parameter values to be distinct from each other during the measurement.

The goal of our work has been to improve the precision with which a parameter, usually transmission, can be estimated. This is done by first finding the fundamental limits in precision when using certain optical states to estimate a parameter and then finding measurements that reach the fundamental limit. We will specialize to Gaussian states of light, when looking at the fundamental limit for parameter estimation. Particularly, we look at the coherent state and squeezed states, with particular focus on the bTMSS.

3.1 Parameter estimation bounds

Not every measurement leads to the same precision in the estimation of a parameter. A change in a given parameter could change the measured quadrature and intensity of a state of light, but one of these measures may be more sensitive to the change than the other. There may even be an unknown measurement that has even higher precision. Finding the limits in the uncertainty of estimating a parameter value leads to knowing whether certain measures are optimal, and therefore at the fundamental limit, or if another measurement can perform better.

The first part of this section derives the lower bound in the uncertainty in the estimation of the parameter given the change in measurement results with respect to changes in the parameter value. The second part shows the fundamental limit of how precise a measurement can be by examining how much the state changes with respect to the parameter of interest. If a measurement's precision is at the fundamental limit, it is an optimal measurement that cannot be improved upon.

3.1.1 Classical Fisher information

For a given measurement, an estimator attempts to predict the value of a parameter of interest. An unbiased estimator[38], $\tilde{p}(x)$, gives, on average, the correct value of the parameter such that $\int \tilde{p}(x)\varrho(x|p)dx = p$, where $\varrho(x|p)$ is the probability distribution of getting the measurement result x given a parameter value p. For example, a high speed camera can be used to give an unbiased estimation for the time it takes a ball to fall from a set height by taking the frame at with the ball is closest to the ground. This frame would have an equally likely chance to be slightly before or after the ball actually hitting the ground, but on average would give a good timing of the landing. A person with a stopwatch would give a biased estimation as they would stop the timer after the impact. Thus, on average, the recorded time would be longer than the actual time to fall.

The minimum uncertainty in the estimation of a parameter can be derived from the definition of an unbiased estimator by first subtracting the actual value of the parameter[5–9]

$$\int [\tilde{p}(x) - p]\varrho(x|p)dx = 0. \tag{3.2}$$

Taking the derivative on both sides of Eq. (3.2) in terms of p and using $\int \varrho(x|p)dx = 1$ and $\frac{\partial \varrho}{\partial p} = \varrho\frac{\partial \ln(\varrho)}{\partial p}$ gives

$$1 = \int \left\{[\tilde{p}(x) - p]\sqrt{\varrho(x|p)}\right\}\left\{\sqrt{\varrho(x|p)}\frac{\partial \ln[\varrho(x|p)]}{\partial p}\right\}dx. \tag{3.3}$$

Applying the Cauchy-Schwarz inequality $(\int AB\,dx)^2 \leq (\int A^2dx)(\int B^2dx)$ then gives

$$1 \leq \left\{\int [\tilde{p}(x) - p]^2\varrho(x|p)dx\right\}\left\{\int \varrho(x|p)\left(\frac{\partial \ln[\varrho(x|p)]}{\partial p}\right)^2 dx\right\}. \tag{3.4}$$

Since the estimator is unbiased, $p = \langle\tilde{p}\rangle$, the first term on the right hand side is the variance. Thus Eq. (3.4) can be rewritten as

$$\langle\Delta^2\tilde{p}\rangle \geq \frac{1}{F(p)}, \tag{3.5}$$

where

$$F(p) = \int \varrho(x|p)\left(\frac{\partial \ln[\varrho(x|p)]}{\partial p}\right)^2 dx \tag{3.6}$$

is the second term on the right hand side of Eq. (3.4). This term is called the Fisher information[4] and it is independent of the estimator. The Cramér-Rao bound[5–9], Eq. (3.5), states that the minimum uncertainty in the estimation of a parameter is given by the inverse of the Fisher information.

Not every estimator will saturate the bound. An unbiased estimator does not constrain the fluctuations around the mean value, it only means that the average is correct. For

instance, if there exists an unbiased estimator with zero variance, another estimator can be constructed from that noiseless estimator plus some random term of zero average value. For a more physical example, making measurements with a detector with high electronic noise is always going to lead to higher uncertainties than making measurements with one that has low electronic noise. Thus, an estimator being unbiased does not guarantee maximum precision.

As we can see from the derivative in Eq. (3.6), the more the measurement results change with the parameter value, the more information is gained about the parameter and thus an estimator should have a lower uncertainty in estimating the parameter's value. Since the derivative in the Fisher information acts on the natural log of the distribution, halving and doubling the probability of a measurement has the same information gain. Thus, the Fisher information can be called a metric for the distinguishability of measurement results, as it is dependent on how the measurement results change for small changes in the parameter.

3.1.2 Quantum Fisher information

As mentioned before, in classical physics it was thought that all measurement fluctuations were due to the measurement device. As such, sufficient engineering should allow for perfect noiseless measurements, such that $\varrho(x|p)$ would be infinitely narrow and only allow for a single unique x for each parameter value. This would lead to an infinite Fisher information. However, quantum mechanics shows that the state itself also leads to measurement noise. A perfect measurement would thus only have the noise from the state measured as the distribution of $\varrho(x|p)$ would be dominated by quantum statistics.

To find the lower bound in the uncertainty in the estimation of a parameter using a perfect measurement, the classical terms from the last section need to be restated in quantum terms to take advantage of the quantum description of states. The probability distribution can be rewritten as

$$\varrho(x|p) \to \mathrm{Tr}(\hat{\Pi}_x \rho_p) \tag{3.7}$$

where $\hat{\Pi}_x$ is a positive operator value measurement (POVM) for value x and ρ_p is the density matrix of the probing state after interacting with the system under study. A POVM is a general way to express a physical measurement as an operator. Applying the trace operation with the density matrix is equivalent to taking the expectation value, $\mathrm{Tr}(\hat{\mathcal{O}}\rho) = \langle\hat{\mathcal{O}}\rangle$. The Fisher information can be expressed in semi-operator form as [39]

$$F(p) = \int \frac{1}{\varrho(x|p)} \left(\frac{\partial \varrho(x|p)}{\partial p}\right)^2 dx \tag{3.8}$$

$$= \int \frac{1}{\mathrm{Tr}(\hat{\Pi}_x \rho_p)} \left(\frac{\partial \mathrm{Tr}(\hat{\Pi}_x \rho_p)}{\partial p}\right)^2 . \tag{3.9}$$

To write the Fisher information completely in operator form, the derivative operation needs to also be written as an operator. This can be done using the symmetric logarithmic deriva-

tive (SLD), $\hat{L}_p$ where

$$\frac{\hat{L}_p\rho_p + \rho_p\hat{L}_p}{2} = \frac{\partial\rho_p}{\partial p}. \tag{3.10}$$

The SLD concept comes from the derivative of the natural log of a variable. The derivative of the natural log is equal to the derivative of the variable times the inverse of variable. Working with non-commuting variables, it is not clear if the inverse should be before, a right logarithmic derivative ($\frac{1}{\rho}\frac{\partial\rho}{\partial p}$), or after the derivative, a left logarithmic derivative ($\frac{\partial\rho}{\partial p}\frac{1}{\rho}$). The symmetric logarithmic derivative is the symmetric form of both options. Using the SLD, Eq. (3.9) can be written purely with operators,

$$F(p) = \int \frac{\Re\left[\mathrm{Tr}(\rho_p\hat{\Pi}_x\hat{L}_p)\right]^2}{\mathrm{Tr}(\rho_p\hat{\Pi}_x)}dx, \tag{3.11}$$

where $\Re[\cdot]$ is the real part.

To find the fundamental limit in the uncertainty for estimating a parameter value dominated by quantum fluctuations, the measurement must be removed from the Fisher Information, just like the estimator was removed from the classical Fisher information. Using $\mathrm{Re}(X)^2 \leq |X|^2$ and together with the permutation property of the trace operation, $\mathrm{Tr}(\hat{A}\hat{B}\hat{C}) = \mathrm{Tr}(\hat{C}\hat{A}\hat{B}) = \mathrm{Tr}(\hat{B}\hat{C}\hat{A})$, we can start the process of removing the measurement, $\hat{\Pi}_x$. These properties transform Eq. (3.11) into[39]

$$F(p) \leq \int \left|\mathrm{Tr}\left(\frac{\sqrt{\rho_p\hat{\Pi}_x}}{\sqrt{\mathrm{Tr}(\rho_p\hat{\Pi}_x)}}\sqrt{\hat{\Pi}_x}\hat{L}_p\sqrt{\rho_p}\right)\right|^2 dx \tag{3.12}$$

which is saturated whenever $\hat{L}_p\rho_p$ is also a valid density matrix. Once again, using the Cauchy-Schwarz inequality, this time of the form $|\mathrm{Tr}(\hat{A}^\dagger\hat{B})|^2 \leq \mathrm{Tr}(\hat{A}^\dagger\hat{A})\mathrm{Tr}(\hat{B}^\dagger\hat{B})$ gives

$$F(p) \leq \int \mathrm{Tr}\left(\frac{\rho_p\hat{\Pi}_x}{\mathrm{Tr}(\rho_p\hat{\Pi}_x)}\right)\mathrm{Tr}(\hat{\Pi}_p\hat{L}_p\rho_p\hat{L}_p)dx \tag{3.13}$$

$$= \int \mathrm{Tr}(\hat{\Pi}_x\hat{L}_p\rho_p\hat{L}_p)dx. \tag{3.14}$$

Finally, using the POVM property $\int \mathrm{Tr}(\hat{\Pi}_x\hat{\mathcal{O}})dx = \mathrm{Tr}(\hat{\mathcal{O}})$ for any operator $\hat{\mathcal{O}}$, the dependence on the measurement can be removed and a QFI, $F^Q(p)$, can be defined such that

$$F(p) \leq F^Q(p) = \mathrm{Tr}(\rho_p\hat{L}_p^2) = \left\langle\hat{L}_p^2\right\rangle. \tag{3.15}$$

The QFI then sets a QCRB of the form

$$\langle\Delta^2 p\rangle \geq \frac{1}{F^Q(p)}. \tag{3.16}$$

The QFI only depends on the state and system under study. Similar to the classical Fisher information, the QFI is dependent on the square of the logarithmic changes in the state. As such, the QFI is a metric for the distinguishability of the state after interaction with the system for different parameter values.

For the estimation of a parameter value to saturate the QCRB, the estimator from the measurement results must be efficient, such that the classical Cramér-Rao bound is saturated and the measurement must be optimal, such that the classical Fisher information is equal to the QFI and thus the classical and quantum bounds are the same.

3.1.3 Other forms of the quantum Fisher information

Keeping the QFI in terms of the SLD is not always useful as the SLD is primarily used for QFI calculations and is not readily available in the literature for most systems. To take advantage of the body of work already done studying quantum systems, the QFI can be rewritten in more familiar terms by first solving for the SLD using the Lyapunov matrix equation[40]. Working in the eigenbasis of $\rho_p = \sum_n r_n |\psi_n\rangle \langle\psi_n|$, the SLD takes the form[39]

$$\hat{L}_p = 2\int_0^\infty e^{-\rho_p q}\frac{\partial \rho_p}{\partial p}e^{-\rho_p q}dq \tag{3.17}$$

$$= 2\sum_{\substack{n,m \\ r_m+r_n>0}} \frac{\langle\psi_m|\frac{\partial\rho_p}{\partial p}|\psi_n\rangle}{r_m+r_n}|\psi_m\rangle\langle\psi_n|, \tag{3.18}$$

where q is a dummy variable used for integration. The QFI can then be written in terms of the change in the density matrix,

$$F^Q(p) = 2\sum_{\substack{n,m \\ r_m+r_n>0}} \frac{\left|\langle\psi_m|\frac{\partial\rho_p}{\partial p}|\psi_n\rangle\right|^2}{r_m+r_n}. \tag{3.19}$$

This form is useful when the density matrix and its dynamics are calculable, which is typically true for states with a finite number of non-zero probabilities, r_n. In particularly, this holds for pure states, as there is only a single non-zero eigenvalue to sum over. However, the derivative of the density matrix for certain parameters can be difficult to calculate and thus this technique may not always be the easiest to use.

In such cases, it may be more tractable to examine how the system under study affects the state instead of how the state itself changes. If the dynamics of the density matrix are fully defined by a unitary matrix, $\hat{U}$, then the QFI can be written as[41]

$$F^Q(p) = 4\sum_{\substack{n \\ r_n>0}} r_n\left\langle\Delta^2\hat{G}\right\rangle_n - \sum_{\substack{n\neq m \\ r_n+r_m>0}} \frac{8r_n r_m}{r_n+r_m}\left|\langle\psi_n|\hat{G}|\psi_m\rangle\right|^2, \tag{3.20}$$

where

$$\hat{G} = i\left(\frac{\partial \hat{U}^\dagger}{\partial p}\right)\hat{U}, \tag{3.21}$$

$$\left\langle \Delta^2 \hat{G} \right\rangle_n = \langle \psi_n | \hat{G}^2 | \psi_n \rangle - \langle \psi_n | \hat{G} | \psi_n \rangle^2, \tag{3.22}$$

and $\hat{G}$ is called the generator. Examples of generators are the time independent Hamiltonian as a generator for time, momentum as the generator for position, and photon number for phase. The unitary operator can be written as $\hat{U} = e^{i\hat{G}p}$, if the generator is independent of the parameter. If the state is pure after interacting with the system, such that there is a single nonzero $r_n = 1$, the second term on the right hand side of Eq. (3.20) vanishes and the QFI simplifies to $F^Q = 4\langle \Delta^2 \hat{G} \rangle$. Since the generator commutes with the unitary operation of the system under study, the variance of $\hat{G}$ is the same for the state before or after interacting with the system. Thus, using this form of the QFI, it is possible to find the QCRB just from the initial state and the generator. This form also demonstrates that to have a lower QCRB for a parameter, a state inevitably has a large uncertainty in the conjugate variable due to the uncertainty principle. For example, a system causes a displacement b to a probing state and the parameter of interest is the magnitude of the displacement, $|b|$. We assume that the displacement operator of such a system can be written as

$$\hat{D}(b) = e^{-i|b|\hat{Q}\left(\delta + \frac{\pi}{2}\right)}, \tag{3.23}$$

where $\delta = \arg(b)$ is the phase of the displacement. The generator in this example is

$$\hat{G} = i\left(\frac{\partial \hat{D}(b)^\dagger}{\partial p}\right)\hat{D}(b) \tag{3.24}$$

$$= -\hat{Q}\left(\delta + \frac{\pi}{2}\right) \tag{3.25}$$

with variance $\langle \Delta^2 \hat{G} \rangle = \langle \Delta^2 \hat{Q}(\delta + \pi/2) \rangle$. As shown in Fig. 3.2, if a bSMSS is used for sensing the displacement, the optimal squeezing angle would be perpendicular to the displacement.

For some parameters and states the above methods are still intractable due to containing a large number of terms. For transmission estimation with squeezed light, which is what this thesis focuses on, losses cause the states to loose purity and the theory description often requires an infinite dimensional density matrix. As such, the summation of the forms listed would have infinite terms. However, as already discussed in the last chapter, Gaussian states are fully characterized by their covariance matrix, σ, and displacement vector, $\vec{d}$, and the QFI can also be written using only those terms. Since the dimensions of this form only depend on the number of modes, losses will not increase the dimensionality of the problem.

The QFI for a 2 mode Gaussian state is given by[32]

$$F^Q(p) = \frac{1}{2\left(|\Sigma| - 1\right)}\left\{ |\Sigma| \operatorname{Tr}\left[\left(\Sigma^{-1}\dot{\Sigma}\right)^2\right] + \sqrt{|\mathbb{I} + \Sigma^2|}\operatorname{Tr}\left[\left(\left(\mathbb{I} + \Sigma^2\right)^{-1}\dot{\Sigma}\right)^2\right] \right.$$
$$\left. + 4\left(\lambda_1^2 - \lambda_2^2\right)\left(\frac{\dot{\lambda}_2^2}{\lambda_2^4 - 1} - \frac{\dot{\lambda}_1^2}{\lambda_1^4 - 1}\right)\right\} + 2\dot{\vec{d}}^\dagger \sigma^{-1} \dot{\vec{d}}, \tag{3.26}$$

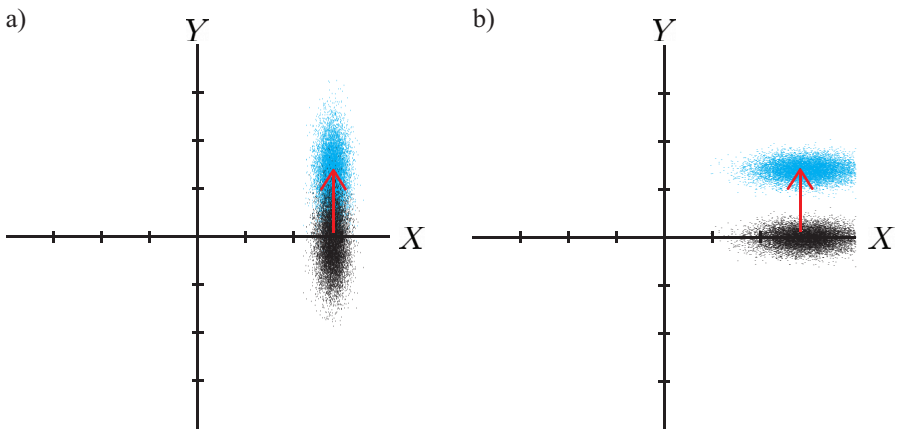


Figure 3.2: For an initial state (black) displaced (red arrow) to a new final state (cyan) it is more difficult to distinguish the change for the state squeezed orthogonal to the displacement (a) than for the state squeezed along the direction of the displacement (b). For in (a), the measured quadrature results from before and after the displacement have a large overlap.

where $\Sigma = K\sigma$ is the covariance matrix in symplectic form, $|\cdot|$ is the determinant, $\dot{\Sigma}$ is the elementwise derivative with respect to the parameter p, and λ_i are the symplectic eigenvalues of the symplectic covariance matrix. Even though for 2 modes the covariance matrix is 4×4, there are only 2 symplectic eigenvalues used to find the QFI. For each eigenvalue λ_i there exists another eigenvalue $-\lambda_i$ of Σ and only the magnitude of the eigenvalues are needed for the calculation. The K term, from $\Sigma = K\sigma$, is defined by the commutation relation of the creation and annihilation operators, $\hat{A} = (\hat{a}_1, ..., \hat{a}_n, \hat{a}_1^\dagger, ..., \hat{a}_n^\dagger)^T$,

$$[\hat{A}, \hat{A}^\dagger] = K, \tag{3.27}$$

such that

$$K = \begin{pmatrix} \mathbb{I} & 0 \\ 0 & -\mathbb{I} \end{pmatrix} \tag{3.28}$$

and $\mathbb{I}$ is the $n \times n$ identity matrix, which is 2×2 matrix for the two mode Gaussian.

This is the form of the QFI that will be used for the majority of this thesis. In the next few chapters, we will go over how to use the Gaussian QFI to find the QCRB for the estimation of transmission using a coherent or squeezed state. Our work has focused on finding the fundamental limit in the estimation of transmission using a bTMSS and the applications of transmission estimation.

Part II

Quantum Enhanced Transmission Estimation

Chapter 4

QCRB of Transmission with Gaussian States of Light

All real world systems, both classical and quantum, suffer from loss. This can be from heat or energy dissipation; reflections from a mismatch in potential, resistance, or mode; or some other sort of irreversible transfer of part of the state into the inaccessible environment. These losses may need to be calibrated, such as for photodetectors and the quantum efficiency of detection or for quantum interferometry, where the optimal state for phase sensing is calibrated based on the amount of loss in the interferometer[14]. As mentioned in the introduction, we focus on the uses of transmission for sensing instead of for calibration.

In sensing, it is important to know the value of the transmission, T, to high precision. This allows for the detection of small changes in the transmission parameter and also the ability to distinguish different possible values. This is useful for systems used as a sensor where a change in the environment can be readout via the change in the sensor transmission. For example, the plasmonic sensor mentioned in the introduction can be set up to detect a given protein in the blood[42]. As each protein molecule binds to the surface of the sensor, the transmission changes. While it may take many bound molecules to generate a detectable transmission change, but a quantum enhanced estimation of transmission can improve the sensitivity of the sensor[43].

4.1 Modeling transmission estimation

The theoretical setup for estimating the transmission of a system is shown in Fig. 4.1. A one or two mode Gaussian state is generated with the probe mode used to probe the system and, if there is a second mode, the conjugate mode used as part of the measurement to reduce the transmission uncertainty. After probing the system, a measurement is made in order to estimate the transmission of the system. For all cases, the number of photons interacting with the system, $\langle \hat{n}_p \rangle_r$, is taken as the sensing resource as this allows for a fair comparison between different states of light. We count the photons interacting with the system instead of the number generated or measured. This is done assuming that the limiting factor in

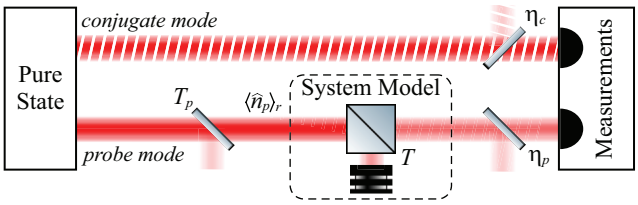


Figure 4.1: Setup for transmission estimation. A Gaussian state is generated and the probing mode is sent through a transmissive system. A measurement is made on the probe mode, and the conjugate mode for a two mode state, to estimate the transmission of the system. Imperfect transmissions are considered from the state generation to the system and from the system to the measurement for the probe mode as well as detection efficiency for the conjugate mode. © American Physical Society. Reproduced with permission. All rights reserved [22].

the estimation of transmission is the damage threshold, how much optical power can be used before damage, of the system under study. Extraneous losses, such as detection and propagation losses, and their effects on the QCRB will be considered later in section 4.3. For now, it will be assumed that the system is probed with pure states and the states can be perfectly detected.

Here, we specialize to a linear transmissive system, which can be modeled as a beam splitter [44]. Only one of the input ports and one of the output ports of the beam splitter is treated as accessible, while the second output port is inaccessible and the photons are lost to the environment. The second input port is the vacuum mode, such that the beam splitter is represented by the unitary operator [45]

$$\hat{B}(T) = e^{\cos^{-1}(\sqrt{T})\left(\hat{a}_p^\dagger \hat{a}_\nu - \hat{a}_p \hat{a}_\nu^\dagger\right)}, \tag{4.1}$$

where T is the transmission and the sub-index p represents the probe mode and ν the vacuum mode. The operator annihilates a photon from the probe mode and creates a photon that is lost to the environment with a given probability $(1-T)$, which transforms the probe field as [29]

$$\hat{B}^\dagger(T)\hat{a}_p\hat{B}(T) \to \sqrt{T}\hat{a}_p + \sqrt{1-T}\hat{a}_\nu. \tag{4.2}$$

This decreases the probe field strength as the probe photons are sent into the environment. Since the parameter of interest is the intensity transmission, any phase rotation due to dispersion or other similar effects have no impact and can be ignored without loss of generality. The beam splitter model for transmission is valid when the loss of a photon does not depend on the loss of any other photon before or after it and the loss of each photon is completely random, with the transmission giving the probability of a photon being lost to the environment. This model works for most lossy systems except for non-linear media [44], such as those that are used to implement the squeezing operation or an absorptive medium near saturation.

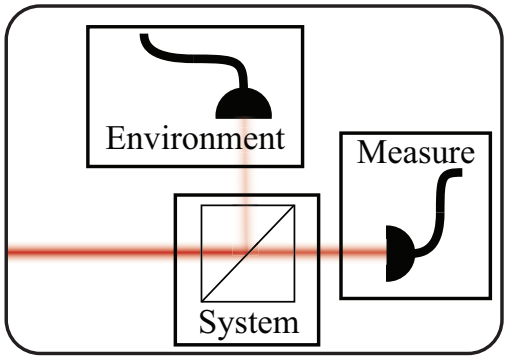


Figure 4.2: In order to derive the ultimate limit in precision for transmission estimation, we will treat the environment as a measurable port of the beam splitter. Normally, when using the beam splitter model for a transmissive system, only one port is accessible. However, allowing for the non-physical measurement of photons lost to the environment, we can calculate the maximum QFI possible for any probing state.

4.1.1 Classical and ultimate limit for transmission estimation

Before examining the different Gaussian states to estimate transmission, let us first set a range of possible uncertainties for a quantum enhanced estimation of transmission. By definition, the enhanced estimation will need to have less uncertainty than the classical limit[46], given by the coherent state QCRB, for at least some range of transmission values. On the other end, is there a limit to how low the QCRB can get for a probing state? For transmission, it turns out that the lowest possible bound can be calculated. This maximum precision that any state can achieve, the ultimate limit, is derived from a non-physical assumption to set a maximum possible QFI[47], as shown in Fig. 4.2. Physically, photons lost to the environment cannot be measured. However, access to these photons can only increase the QFI as these photons are the only other source of information, outside the transmitted photons. Thus, a bound derived from access to the photons lost to the environment gives a loose, due to the non-physical derivation, lower bound for the QCRB of any state. A state that has the same QCRB as this ultimate limit would have to contain all possible information about the system under study. The generator form of the QFI, Eq. (3.20), can be used to derive the ultimate limit using an arbitrary state as this form depends more on the dynamics of the system than the changes in the state. The generator, $\hat{G}$, for the beam splitter can be found using Eq. (3.21),

$$\hat{G} = i\left(\frac{\partial \hat{B}(T)^\dagger}{\partial T}\right)\hat{B}(T) \tag{4.3}$$

$$= \frac{i}{2}\frac{\hat{a}_p^\dagger \hat{a}_\nu - \hat{a}_p \hat{a}_\nu^\dagger}{\sqrt{T(1-T)}}. \tag{4.4}$$

The variance of the generator can be calculated using an initial arbitrary pure state $|\psi_p\rangle$ probing the system and the vacuum state $|0_\nu\rangle$ at the second input port such that

$$\left\langle \Delta^2 \hat{G} \right\rangle = \langle 0_\nu| \langle \psi_p| \hat{G}^2 |\psi_p\rangle |0_\nu\rangle - \langle 0_\nu| \langle \psi_p| \hat{G} |\psi_p\rangle |0_\nu\rangle^2 \tag{4.5}$$

$$= \frac{-1}{4} \frac{1}{T(1-T)} \Big[\langle 0_\nu| \langle \psi_p| \left(\hat{a}_p^\dagger \hat{a}_\nu - 0 \right) \left(0 - \hat{a}_p \hat{a}_\nu^\dagger \right) |\psi_p\rangle |0_\nu\rangle - 0 \Big] \tag{4.6}$$

$$= \frac{1}{4T(1-T)} \langle \psi_p| \hat{n}_p |\psi_p\rangle \langle 0_\nu|0_\nu\rangle \tag{4.7}$$

and $F^Q = 4\langle \Delta^2 \hat{G} \rangle$ for pure states. If the state was mixed, such that there is a classical probability of being in one of many different states, the extra terms on the right hand side of the generator QFI equation, Eq. (3.20), can only reduce the QFI[41] due to it always being negative. Only a pure state assumption is needed to set the lowest limit for the QCRB. Thus, the ultimate limit for the QCRB of any state used to estimate transmission is[20]

$$\left\langle \Delta^2 T \right\rangle^{(ult)} \geq \frac{T - T^2}{\langle \hat{n}_p \rangle_r}, \tag{4.8}$$

where $\langle n_p \rangle_r$ is the average number of photons probing the system.

It is known that the Fock state can saturate the ultimate bound[20]. This state changes with transmission as[45]

$$|n\rangle\langle n| \to \sum_{k=0}^{n} r_k |k\rangle\langle k| = \sum_{k=0}^{n} \frac{n!}{k!(n-k)!} T^k (1-T)^{n-k} |k\rangle\langle k| \equiv \rho_T^{\text{Fock}}, \tag{4.9}$$

such that the QFI can be found using Eq. (3.19),

$$F_{\text{Fock}}^Q(T) = \sum_{k=0}^{n} \frac{\left| \langle k| \frac{\partial \rho_T^{\text{Fock}}}{\partial T} |k\rangle \right|^2}{r_k} \tag{4.10}$$

$$= \frac{n}{T(1-T)}. \tag{4.11}$$

The saturation of the ultimate limit is due to the zero variance in the number of photons in the Fock state[20]. If a Fock state of N photons probes the transmissive medium and $M \leq N$ photons are measured then $N-M$ photons must have been lost to the environment. No information was lost due to not being able to measure the environment, which is why the Fock state has the maximum QFI and thus the minimum QCRB, reaching the ultimate limit.

Returning to finding the classical limit for transmission estimation, the Gaussian form of the QFI, Eq. (3.26), will be used to calculate the coherent state bound. The covariance matrix for the coherent state is unchanged after probing the transmissive system and is still $\boldsymbol{\sigma}$ =diag(1,1), but the displacement vector is reduced, due to the reduction in field amplitude, to

$$\vec{d} = \sqrt{T} \begin{pmatrix} \alpha \\ \alpha^* \end{pmatrix}, \tag{4.12}$$

such that the *field* displacement, $|\alpha|$, decreases by the square root of the *intensity* transmission. Since the covariance matrix is independent of transmission, the terms on the right hand side, other than the last one, of the Gaussian QFI, Eq. (3.26), are zero. Thus, the QFI for the coherent state can be derived as

$$F^Q_{\text{coh}} = 2\frac{\partial \vec{d}^\dagger}{\partial T}\boldsymbol{\sigma}^{-1}\frac{\partial \vec{d}}{\partial T} \tag{4.13}$$

$$= \frac{1}{2T}\begin{pmatrix}\alpha^* & \alpha\end{pmatrix}\begin{pmatrix}\alpha \\ \alpha^*\end{pmatrix} \tag{4.14}$$

$$= \frac{|\alpha|^2}{T}, \tag{4.15}$$

and therefore the classical limit for the QCRB is[21,19]

$$\left\langle \Delta^2 T \right\rangle^{(\text{coh})} \geq \frac{T}{\langle \hat{n}_p \rangle_r}, \tag{4.16}$$

where $|\alpha|^2 = \langle \hat{n}_p \rangle_r$ is the number of photons probing the system.

Both the ultimate and classical limit for the QCRB scale inversely with the number of probing photons, $\propto \frac{1}{\langle \hat{n}_p \rangle_r}$. The more photons probe the system, the lower the transmission uncertainty. For any system, it is always easier to lower the uncertainty by increasing the number of probing photons than it is to generate a quantum state of light to probe the system. However, many systems have a damage threshold and so we need to consider a finite number of resources, $\langle \hat{n}_p \rangle_r$, with which to probe the system. The maximum enhancement from using quantum states of light can be seen from how the bounds scale with transmission, that is linearly, T, for the coherent state and quadratically, $T - T^2$, for the ultimate limit. At high transmission a large enhancement is possible but as the transmission decreases so does the possible quantum advantage.

4.2 Quantum enhanced QCRB with squeezed states

The Fock state can reach the ultimate limit and thus have maximally enhanced measurement precision in the estimation of transmission over a classical state. However, it is hard to generate, especially at high powers[48]. In practice, a Fock state may not be the optimal state to measure transmission due to the $\frac{1}{\langle \hat{n}_p \rangle_r}$ scaling and due to the fact that Fock states cannot currently be generated with enough power to reach the damage threshold for most systems under study. Higher power states, with a QCRB below the classical limit but higher than the ultimate limit, can achieve a better overall estimation than a Fock state, even if these states are worse for an equal number of probing photons.

4.2.1 Single mode squeezed states

The first state we will look at is the bSMSS. This state, when squeezed in the amplitude quadrature, has a reduced variance in the number of photons compared to the coherent state.

Since the Fock state has no photon number variance, it can be expected that the reduced number variance of the amplitude squeezed bSMSS will lead to enhanced transmission estimation. The bSMSS, with level of squeezing s and squeezing angle θ, after probing the system has a covariance matrix that changes with transmission as [22]

$$\boldsymbol{\sigma} = \begin{pmatrix} T\cosh(2s) + 1 - T & -Te^{i\theta}\sinh(2s) \\ -Te^{-i\theta}\sinh(2s) & T\cosh(2s) + 1 - T \end{pmatrix} = T\boldsymbol{\sigma}_{\text{initial}} + (1-T)\boldsymbol{\sigma}_{\text{vacuum}}, \tag{4.17}$$

such that the average quadrature variance, the diagonal, decreases to one and the asymmetry, off-diagonal terms, reduces to zero as transmission decreases and the state becomes a photonless vacuum state. The displacement for the bSMSS changes as

$$\vec{d} = \sqrt{T}\begin{pmatrix} \alpha\cosh(s) - \alpha^* e^{i\theta}\sinh(s) \\ \alpha^*\cosh(s) - \alpha e^{-i\theta}\sinh(s) \end{pmatrix}, \tag{4.18}$$

which scales the same way as the coherent state. Thus, any quantum enhancement in the estimation of transmission must come from the covariance matrix.

As with the coherent state, the Gaussian QFI calculation, Eq. (3.26), for the bSMSS is dominated by the displacement term such that [22]

$$F^Q_{\text{bSMSS}} = 2\frac{\partial\vec{d}^\dagger}{\partial T}\boldsymbol{\sigma}^{-1}\frac{\partial\vec{d}}{\partial T} \tag{4.19}$$

$$= |\alpha|^2\frac{T + (1-T)\left[\cosh(2s) - \cos(\Theta)\sinh(2s)\right]}{T\left\{1 - 2T(1-T)\left[1 - \cosh(2s)\right]\right\}}, \tag{4.20}$$

where $\Theta = \theta - 2\arg(\alpha)$. The QFI per photon is maximized when the state is amplitude squeezed, which occurs when $\cos(\Theta) = 1$ such that $\langle\Delta^2\hat{n}_p\rangle = \langle\hat{n}_p\rangle e^{-2s}$. This gives a QCRB of [19,22]

$$\left\langle\Delta^2 T\right\rangle^{(\text{bSMSS})} \geq \frac{T - T^2\left(1 - e^{-2s}\right)}{\langle\hat{n}_p\rangle_r}, \tag{4.21}$$

where $\langle\hat{n}_p\rangle_r = |\alpha|^2\left[\cosh(2s) - \cos(\Theta)\sinh(2s)\right] = |\alpha|^2 e^{-2s}$. The $(1 - e^{-2s})$ coefficient for the quadratic term goes to one as $s \to \infty$, meaning that the QCRB for the bSMSS tends towards the ultimate bound with increased squeezing. However, if the state was squeezed along the phase quadrature, $\cos(\Theta) = -1$, and thus anti-squeezed along the amplitude, the QCRB would be

$$\left\langle\Delta^2 T\right\rangle^{(\text{bSMSS, phase})} \geq \frac{T - T^2\left(1 - e^{2s}\right)}{\langle\hat{n}_p\rangle_r}, \tag{4.22}$$

where $\langle\hat{n}_p\rangle_r = |\alpha|^2 e^{2s}$ and $\langle\Delta^2\hat{n}_p\rangle = \langle\hat{n}_p\rangle e^{2s}$. As such, increased photon number variance increases the bound in the uncertainty in transmission estimation, even making it higher than that of the coherent state. At extremely high levels of phase squeezing, the uncertainty in transmission would be dominated by the quadratic term and at infinite phase squeezing the transmission uncertainty would be infinite as well. It should be noted that this correlation between transmission estimation and photon number variance is not always the case, as the vSMSS has a higher photon number variance than the phase squeezed bSMSS but has been

shown to still reach the ultimate limit at high transmission, $T \approx 1$[19]. This is due to the photons being generated in pairs, such that the loss of a single photon is easily noticed via a parity, even or odd photon number, measurement. At lower transmission, however, the vSMSS is much worse than a coherent state due to having a photon number variance that is twice as large as that of a thermal state.

4.2.2 Two mode squeezed states

Switching to the two mode Gaussian state, the bTMSS has a conjugate mode that has a photon number correlated to the number of photons in the probe mode interacting with the system under study. This correlation allows for the inference of the number of photons lost to the environment, reducing the uncertainty in transmission estimation. The covariance matrix of the bTMSS changes with transmission as[22]

$$\boldsymbol{\sigma} = \begin{pmatrix} T\cosh(2s)+1-T & 0 & 0 & -\sqrt{T}e^{i\theta}\sinh 2s \\ 0 & \cosh(2s) & -\sqrt{T}e^{i\theta}\sinh 2s & 0 \\ 0 & -\sqrt{T}e^{-i\theta}\sinh 2s & T\cosh(2s)+1-T & 0 \\ -\sqrt{T}e^{-i\theta}\sinh 2s & 0 & 0 & \cosh(2s) \end{pmatrix}. \tag{4.23}$$

Unlike the single mode case, the asymmetry of the quadratures decreases with the square root of the transmission as only one of the modes is affected by the system under study and the asymmetry is in the combination of the two mode quadratures. The displacement vector changes as[22]

$$\vec{d} = \begin{pmatrix} \sqrt{T}\left[\alpha\cosh(s) - \beta^* e^{i\theta}\sinh(s)\right] \\ \beta\cosh(s) - \alpha^* e^{i\theta}\sinh(s) \\ \sqrt{T}\left[\alpha^*\cosh(s) - \beta e^{-i\theta}\sinh(s)\right] \\ \beta^*\cosh(s) - \alpha e^{-i\theta}\sinh(s) \end{pmatrix}, \tag{4.24}$$

such that only the probe mode, denoted by the first and third terms, has reduced displacement. With large displacement, such that the displacement term of the QFI dominates, we have found a bTMSS QCRB of[22]

$$\left\langle \Delta^2 T \right\rangle^{(\mathrm{bTMSS})} \geq \frac{T - T^2\left[1 - \mathrm{sech}(2s)\right]}{\left\langle \hat{n}_p \right\rangle_r}, \tag{4.25}$$

where $\left\langle \hat{n}_p \right\rangle_r = |\alpha|^2\cosh^2(s) + |\beta|^2\sinh^2(s) - |\alpha||\beta|\cos(\Theta)\sinh(2s)$, $\Theta = \theta - \arg(\alpha) - \arg(\beta)$, and $|\alpha|^2$ and $|\beta|^2$ are the mean number of seeding photons for the probe and conjugate modes, respectively.

As with the bSMSS, as the squeezing increases this bound tends towards the ultimate limit[22]. However, the bTMSS QCRB approaches the bound more slowly than the bSMSS QCRB, as can be seen by comparing Fig. 4.3a and Fig. 4.3b. In theory, the bSMSS would be better for measuring transmission; however, in practice this may not be the case. Since the bTMSS has a second mode that is correlated with the probing mode, technical noise from a real experiment can be canceled out. Since any technical noise would be correlated between

the two modes, a differential measurement can cancel the technical noise[44] due to the pair generation of photons.

If the two mode squeezed state had zero displacement, the number of photons in each mode would be perfectly correlated, leading to an increase in QFI per probe photon. For the vTMSS, the QFI is derived using the non-displacement terms of the Gaussian QFI[22], Eq. (3.26),

$$\begin{aligned} F^{Q}(T) &= \frac{1}{2\left(|\Sigma|-1\right)}\Bigg\{ |\Sigma|\,\mathrm{Tr}\left[\left(\Sigma^{-1}\dot{\Sigma}\right)^{2}\right] + \sqrt{|\mathbb{I}+\Sigma^{2}|}\mathrm{Tr}\left[\left(\left(\mathbb{I}+\Sigma^{2}\right)^{-1}\dot{\Sigma}\right)^{2}\right] \\ &\quad +4\left(\lambda_1^2-\lambda_2^2\right)\left(\frac{\dot{\lambda}_2^2}{\lambda_2^4-1}-\frac{\dot{\lambda}_1^2}{\lambda_1^4-1}\right)\Bigg\}. \end{aligned} \tag{4.26}$$

For the two mode squeezed state, the eigenvalues are

$$\lambda_1 = 1, \tag{4.27}$$

$$\lambda_2 = T+(1-T)\cosh(2s), \tag{4.28}$$

for the symplectic form of the covariance matrix

$$\Sigma = \begin{pmatrix} T\cosh(2s)+1-T & 0 & 0 & -\sqrt{T}e^{i\theta}\sinh 2s \\ 0 & \cosh(2s) & -\sqrt{T}e^{i\theta}\sinh 2s & 0 \\ 0 & \sqrt{T}e^{-i\theta}\sinh 2s & -T\cosh(2s)-(1-T) & 0 \\ \sqrt{T}e^{-i\theta}\sinh 2s & 0 & 0 & -\cosh(2s) \end{pmatrix}. \tag{4.29}$$

Since $\dot{\lambda}_1 = 0$, the term $\frac{\dot{\lambda}_1^2}{\lambda_1^4-1}$ in Eq. (3.26) is zero. Typically, a correction factor is needed when an eigenvalue of Σ is one[32], but for transmission estimation the correction factor is zero[22]. This correction factor is only ever needed for pure states as only those states have eigenvalues of ± 1. Thus, it is most likely due to the decoherence effect of the transmission parameter that the correction factor is zero for this problem.

Solving for the QFI, it can be shown that the QCRB for the vTMSS is the same as the ultimate limit[21],

$$\left\langle \Delta^2 T\right\rangle^{(\mathrm{vTMSS})} \geq \frac{T-T^2}{\left\langle \hat{n}_p\right\rangle_r}, \tag{4.30}$$

where $\left\langle \hat{n}_p\right\rangle_r = \sinh^2(s)$. Like the Fock state, there is no loss of information to the environment when probing the system since the conjugate mode acts as a reference for the number of photons in the probe mode. Also like the Fock state, these states can only be generated at a low power with current technology, though the vTMSS has higher photon number in the probe mode than what is possible for a Fock state. There has been work done to further increase the power of the vTMSS, creating so called bright vTMSS[49,50]. Being generated with more power increases the number of known systems in which the vTMSS can reach the damage threshold. This would make these states ideal, since they reach the ultimate

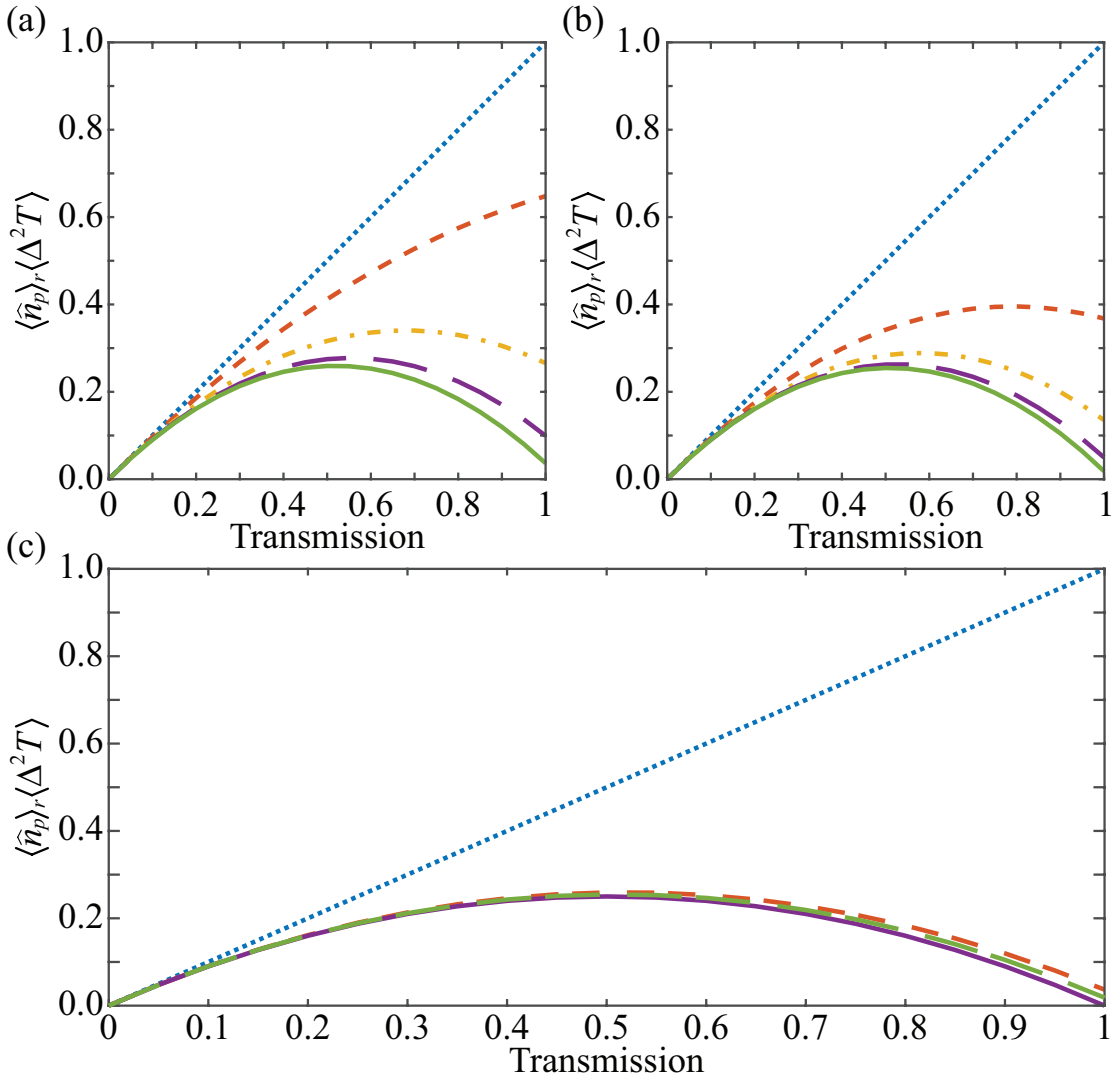


Figure 4.3: The uncertianty in the estimation of transmission decreases as s increases from 0 (blue dotted line), 0.5 (red dashed line), 1.0 (yellow dot-dashed line), 1.5 (purple long dashed line), to 2.0 (green solid line) for the bTMSS (a) and bSMSS (b). The plot in (c) compares the coherent state (blue dotted line) to the $s = 2$ bTMSS (red short dashed line), bSMSS (green long dashed line), and the ultimate limit (purple solid line). © American Physical Society. Reproduced with permission. All rights reserved[22].

limit, for transmission estimation. However, these state are not pure vTMSS and have lower correlations between the modes than the current state of the art for bTMSS generation and thus are currently not as good for transmission estimation.

Given that the QFI for the vTMSS is very large for a transmission near one, the assumption made for the bTMSS QFI being dominated by the displacement term needs to be examined further. Since the vacuum term of the bright two-mode squeezed state will always dominate at $T = 1$ where $F^Q_{\text{vTMSS}} = \infty$, the threshold for which the bTMSS dominates is transmission dependent. Momentarily removing the assumptuion of bright or vacuum domination, the total QFI in terms of generated photons for the two-mode squeezed state must be considered, that is

$$F^Q_{\text{TMSS}} = F^Q_{\text{vTMSS}} + F^Q_{\text{bTMSS}} \tag{4.31}$$

$$= \frac{\langle \hat{n}_p \rangle_{\text{vac}}}{T - T^2} + \frac{\langle \hat{n}_p \rangle_{\text{bright}}}{T - T^2\left[1 - \text{sech}(2s)\right]}, \tag{4.32}$$

where $\langle \hat{n}_p \rangle_{\text{vac}}$ is the number of photons spontaneously generated by the squeezing operation and $\langle \hat{n}_p \rangle_{\text{bright}}$ is the number of stimulated photons generated from the initial displaced state. For the bright QFI to dominate, and thus ignore the vacuum term contributions, the number of stimulated photons must be large enough such that

$$\langle \hat{n}_p \rangle_{\text{bright}} \gg \langle \hat{n}_p \rangle_{\text{vac}} + \frac{T\,\text{sech}(2s)}{1 - T} \langle \hat{n}_p \rangle_{\text{vac}}\,. \tag{4.33}$$

At low transmissions, $T < 50\%$, the bright limit is reached when there are many more bright photons than vacuum term photons. As the transmission increases, the second term on the right hand side of Eq. (4.33) dominates as it becomes very large as $T \to 1$. For large squeezing, a bright limit at high transmission can be set from

$$\lim_{s\to\infty} \text{sech}(2s)\sinh^2(s) \to \frac{1}{2}, \tag{4.34}$$

since $\langle \hat{n}_p \rangle_{\text{vac}} = \sinh^2(s)$, such that the bright limit can be obtained when [22]

$$\langle \hat{n}_p \rangle_{\text{bright}} \gg \frac{1}{2}\left(\frac{T}{1 - T}\right). \tag{4.35}$$

For a transmission of 99.95%, the bright portion of the probe mode with greater than an average of 1,000 photons is needed. Since bTMSS are generally generated with coherent states with a photon flux many orders of magnitude higher than that, the approximation of the displaced terms dominating is typically valid [51].

For zero squeezing for either the bSMSS or bTMSS, the state is a coherent state and the bound goes to the classical QCRB. This is the benefit of bright squeezed states, that the state starts with high photon number, like a classical state, and then is squeezed to get closer to the ultimate bound. Thus the state has a high photon number, to compete with a classical state with the $\frac{1}{\langle \hat{n}_p \rangle_r}$ scaling, and quantum enhancement that gives a lower QCRB

for the same number of probing photons. As shown in Fig. 4.3, for currently accessible levels of squeezing, $s = 2$[52,23], the difference between the low power Fock and vTMSS and the higher power bSMSS and bTMSS QCRBs is small. This is especially true when compared to the enhancement from the coherent state bound.

It should also be noted for the two mode states that if the conjugate mode of the vTMSS is undetected the probe mode is the same as a thermal state, as mentioned in Chapter 2. Similar to the quantum states, the QCRB for the thermal state is quadratic,

$$\left\langle \Delta^2 T \right\rangle^{(\text{Thermal})} \geq \frac{T + T^2 \left\langle \hat{n}_p \right\rangle}{\left\langle \hat{n}_p \right\rangle_r}, \tag{4.36}$$

but the quadratic term is positive, similar to the bSMSS when phase squeezed, Eq. (4.22), which can be rewritten as

$$\left\langle \Delta^2 T \right\rangle^{(\text{bSMSS, phase})} \geq \frac{T + T^2 \left(e^{2s} - 1\right)}{\left\langle \hat{n}_p \right\rangle_r} \tag{4.37}$$

to make the comparison easier. For the bTMSS the probe mode by itself would be a displaced thermal state. As will be shown in the next section, losses in the conjugate mode can undo the quantum advantage of the two mode squeezed state, even making these states worse than a coherent state with sufficient conjugate loss such that the bTMSS tends towards a thermal state. Thus, the choice of using the bSMSS or the bTMSS depends on the limitations of the physical setup of the sensing scheme.

4.3 QCRB with extraneous losses and imperfect detection

For a real experiment, it is not currently possible to probe the system without any propagation loss from the source to the system under study or to perfectly detect the state after interaction with the system. For practical applications, the QCRB for the states should be expanded to include transmissions both before, T_p, and after, η_p, probing the system and, for the two mode states, detection efficiencies of the conjugate mode, η_c, as shown in Fig. 4.1. The resources for probing a system under study considered here are still the number of photons interacting with the system $\left\langle \hat{n}_p \right\rangle_r = T_p \left\langle \hat{n}_p \right\rangle_0$, where $\left\langle \hat{n}_p \right\rangle_0$ are the number of probe photons generated and T_p is the transmission between the pure state generation and the system under study. As a detector with a quantum efficiency less than 100% can be modeled as a perfect detector and a beam splitter with a transmission equal to the quantum efficiency of the actual detector[44], the term η_p is given as the probe transmission between the system under study and a perfect detector. The covariance matrices for the various states are the same as before except with $T \to T_p T \eta_p$. For the bTMSS, additional considerations must be taken into account for the covariance matrix and displacement vector due to the losses in the conjugate mode. In general, the covariance matrix and displacement vector take the

form [22]

$$\boldsymbol{\sigma} = \begin{pmatrix} T_pT\eta_p\cosh(2s)+1-T_pT\eta_p & 0 & 0 & -\sqrt{T_pT\eta_p\eta_c}e^{i\theta}\sinh(2s) \\ 0 & \eta_c\cosh(2s)+1-\eta_c & -\sqrt{T_pT\eta_p\eta_c}e^{i\theta}\sinh(2s) & 0 \\ 0 & -\sqrt{T_pT\eta_p\eta_c}e^{-i\theta}\sinh(2s) & T_pT\eta_p\cosh(2s)+1-T_pT\eta_p & 0 \\ -\sqrt{T_pT\eta_p\eta_c}e^{-i\theta}\sinh(2s) & 0 & 0 & \eta_c\cosh(2s)+1-\eta_c \end{pmatrix}, \tag{4.38}$$

$$\vec{d} = \begin{pmatrix} \sqrt{T_pT\eta_p}\left[\alpha\cosh(s) - \beta^* e^{i\theta}\sinh(s)\right] \\ \sqrt{\eta_c}\left[\beta\cosh(s) - \alpha^* e^{i\theta}\sinh(s)\right] \\ \sqrt{T_pT\eta_p}\left[\alpha^*\cosh(s) - \beta e^{-i\theta}\sinh(s)\right] \\ \sqrt{\eta_c}\left[\beta^*\cosh(s) - \alpha e^{-i\theta}\sinh(s)\right] \end{pmatrix}, \tag{4.39}$$

where the conjugate transmission, η_c, is added to the conjugate terms of the covariance matrix and displacement vector and the asymmetry term in the covariance matrix in addition to the changes to the probe transmission from losses before and after the system. We have found the QCRBs for the lossy coherent state, bSMSS, bTMSS, and Fock state to be, following the same procedures as before for the lossless cases, [22]

$$\left\langle \Delta^2 T \right\rangle^{(\mathrm{coh})} \geq \frac{T}{\eta_p \left\langle \hat{n}_p \right\rangle_r}, \tag{4.40}$$

$$\left\langle \Delta^2 T \right\rangle^{(\mathrm{bTMSS})} \geq \frac{T}{\eta_p \left\langle \hat{n}_p \right\rangle_r} - \frac{T^2}{\left\langle \hat{n}_p \right\rangle_r} T_p H_c[1 - \mathrm{sech}(2s)], \tag{4.41}$$

$$\left\langle \Delta^2 T \right\rangle^{(\mathrm{bSMSS})} \geq \frac{T}{\eta_p \left\langle \hat{n}_p \right\rangle_r} - \frac{T^2}{\left\langle \hat{n}_p \right\rangle_r} T_p(1 - e^{-2s}), \tag{4.42}$$

$$\left\langle \Delta^2 T \right\rangle^{(\mathrm{Fock})} \geq \frac{T}{\eta_p \left\langle \hat{n}_p \right\rangle_r} - \frac{T^2}{\left\langle \hat{n}_p \right\rangle_r} T_p, \tag{4.43}$$

where

$$H_c = \frac{(2\eta_c - 1)\left[1 + 2\sinh^2(s)\right]}{1 + 2\eta_c \sinh^2(s)} \tag{4.44}$$

contains all the loss terms for the conjugate mode. For $\eta_c > 0.5$, H_c is positive but for $\eta_c < 0.5$ it is negative. When H_c is negative, the quadratic term of the bTMSS QCRB changes sign and the QCRB of the lossy bTMSS is worse than the coherent state bound. At $\eta_c = 0.5$, $H_c = 0$ and the bTMSS QCRB is exactly the same as the one for the coherent state, independent of the level of squeezing. For $\eta_c = 0$, H_c is maximally negative and the bTMSS QCRB is the same as a displaced thermal state QCRB [22].

For each quantum state bound, the second term on the right hand side of Eqs. (4.41)-(4.43), the quadratic term, gives the enhancement in the transmission measurement. The term deceases linearly with transmission, T_p, between state generation and the system as the probe mode for these states tends towards a coherent state as losses increase. In particular, for the bTMSS

$$\frac{\left\langle \Delta^2 T \right\rangle^{(\mathrm{bTMSS})}}{\left\langle \Delta^2 T \right\rangle^{(\mathrm{coh})}} = 1 - \eta_p T T_p H_c[1 - \mathrm{sech}(2s)] \xrightarrow[T_p \to 0]{} 1. \tag{4.45}$$

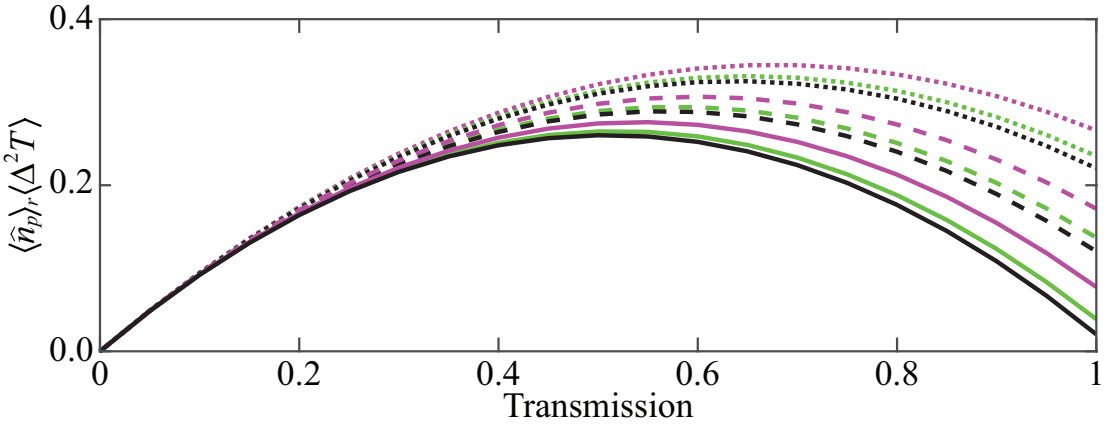


Figure 4.4: Effects of loss on the QCRB for the Fock state (black), bSMSS (green), and bTMSS (magenta). For each state the detection efficiency is $\eta_c = \eta_p = 0.98$ and $T_p = 1$ (solid), $T_p = 0.9$ (dashed), and $T_p = 0.8$ (dotted). © American Physical Society. Reproduced with permission. All rights reserved[22].

However, the coherent state QCRB does not depend on T_p as the state is already a coherent state and the number of probing photons is held constant. The effects of loss on the Fock, bSMSS, and bTMSS state are shown in Fig. 4.4 where we can see that the bound increases rapidly at high transmission and more slowly at low transmission.

For each bound, the linear term is the same for all the states considered and is inversely proportional to the probe transmission after interacting with the system, η_p. This linear term is also the only term that the coherent state has, thus it can be considered as the term corresponding to the classical limit. As the detection efficiency, η_p, of the probe mode goes to zero, the classical term becomes larger and dominates the quantum bounds considered here such that the enhancement due to the use of a quantum states becomes negligible. For example, for the bTMSS

$$\frac{\langle \Delta^2 T \rangle^{(\text{bTMSS})}}{\langle \Delta^2 T \rangle^{(\text{coh})}} = 1 - \eta_p T T_p H_c [1 - \text{sech}(2s)] \xrightarrow[\eta_p \to 0]{} 1. \tag{4.46}$$

This is true for the bSMSS and Fock state as well. As can be seen from Eq. (4.46) and Eq. (4.45), the quantum enhancement decreases linearly with the probe transmission, including the transmission to be estimated.

4.4 Measurements that saturate the QCRB for transmission estimation

The QCRB sets the limit for how precise a measurement can be when estimating a parameter value, but it does not state what measurement will saturate it. Mathematically, it is possible to build a POVM from the SLD[39], introduced in Chapter 3, but those measurements are not

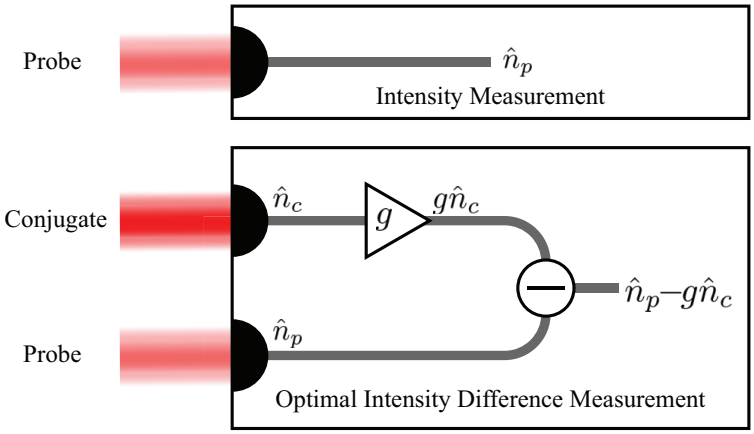


Figure 4.5: Measurements that saturate the QCRB for transmission estimation for the analyzed states. The top diagram is the intensity, or photon counting, measurement that saturates the bound of the single mode states considered; that is, the coherent, bSMSS, and Fock states. On the bottom is the optimized intensity difference measurement that saturates the bound of the bTMSS. For this measurement, an electronic gain, $g \geq 0$, is applied to the intensity measurement of the conjugate mode before subtracting the intensities of the two modes. The electronic gain is set to maximize the cancellation of the intensity fluctuations of the probe mode. If the conjugate mode is uncorrelated to the probe mode, the optimal gain is zero and the measurement simplifies to an intensity measure. Thus, the optimized intensity difference measurement also saturates the bound for the coherent, bSMSS, and Fock states. © American Physical Society. Reproduced with permission. All rights reserved[22].

always physical. The search for measurements that can actually be performed and saturate the QCRB is non-trivial. Here, we will identify measurements that saturate the QCRB for transmission for states with pure generation and extraneous propagation and detection losses.

For the single mode states given by Eqs. (4.40), (4.42), and (4.43), it can be shown that the intensity measurement, or photon counting measurement, shown in Fig. 4.5, saturates the QCRB for each of the single mode states considered [22]. The variance of the measurement is given by

$$\begin{aligned}
\left\langle \Delta^2 \hat{n}_p \right\rangle &= \left\langle \hat{B}_p^\dagger(T_p T \eta_p)\, \hat{n}_p^2\, \hat{B}_p(T_p T \eta_p) \right\rangle - \left\langle \hat{B}_p^\dagger(T_p T \eta_p)\, \hat{n}_p\, \hat{B}_p(T_p T \eta_p) \right\rangle^2 && (4.47)\\
&= \left\langle \left[\left(\sqrt{T_p T \eta_p}\hat{a}_p^\dagger + \sqrt{1 - T_p T \eta_p}\hat{a}_\nu^\dagger \right) \left(\sqrt{T_p T \eta_p}\hat{a}_p + \sqrt{1 - T_p T \eta_p}\hat{a}_\nu \right) \right]^2 \right\rangle \\
&\quad - \left\langle \left(\sqrt{T_p T \eta_p}\hat{a}_p^\dagger + \sqrt{1 - T_p T \eta_p}\hat{a}_\nu^\dagger \right) \left(\sqrt{T_p T \eta_p}\hat{a}_p + \sqrt{1 - T_p T \eta_p}\hat{a}_\nu \right) \right\rangle^2 && (4.48)\\
&= (T_p T \eta_p)^2 \left\langle \hat{n}_p^2 \right\rangle + T_p T \eta_p (1 - T_p T \eta_p) \left\langle \hat{n}_p \right\rangle - (T_p T \eta_p)^2 \left\langle \hat{n}_p \right\rangle^2 && (4.49)\\
&= (T_p T \eta_p)^2 \left\langle \Delta^2 \hat{n}_p \right\rangle_0 + T_p T \eta_p (1 - T_p T \eta_p) \left\langle \hat{n}_p \right\rangle_0 , && (4.50)
\end{aligned}$$

where $\langle \hat{n}_p \rangle_0$ and $\langle \Delta^2 \hat{n}_p \rangle_0$ are the expectation value and variance for the initially generated probe photon number, respectively. Error propagation into transmission uncertainty, shows that

$$\begin{aligned}
\left\langle \Delta^2 T \right\rangle &= \frac{\left\langle \Delta^2 \hat{n}_p \right\rangle}{\left| \frac{\partial \langle T_p T \eta_p \hat{n}_p \rangle_0}{\partial T} \right|^2} && (4.51)\\
&= \frac{T}{\eta_p \left\langle \hat{n}_p \right\rangle_r} - \frac{T^2}{\left\langle \hat{n}_p \right\rangle_r} T_p \left(1 - \frac{\left\langle \Delta^2 \hat{n}_p \right\rangle_0}{\left\langle \hat{n}_p \right\rangle_0} \right), && (4.52)
\end{aligned}$$

where $\frac{\langle \Delta^2 \hat{n}_p \rangle_0}{\langle \hat{n}_p \rangle_0}$ is the Fano factor [44] for the generated state. For each single mode state, the Fano factor is given by

$$\frac{\left\langle \Delta^2 \hat{n}_p \right\rangle_0}{\left\langle \hat{n}_p \right\rangle_0} = \begin{cases} 1 & \text{coherent state} \\ e^{-2s} & \text{bSMSS} \\ 0 & \text{Fock state.} \end{cases} \qquad (4.53)$$

Substituting each Fano factor into Eq. (4.52), shows that this measurement saturates the corresponding QCRBs given in Eqs. (4.40), (4.42), and (4.43), for those states,

$$\begin{aligned}
\left\langle \Delta^2 T \right\rangle^{(\text{coh})} &= \frac{T}{\eta_p \left\langle \hat{n}_p \right\rangle_r}, && (4.54)\\
\left\langle \Delta^2 T \right\rangle^{(\text{bSMSS})} &= \frac{T}{\eta_p \left\langle \hat{n}_p \right\rangle_r} - \frac{T^2}{\left\langle \hat{n}_p \right\rangle_r} T_p (1 - e^{-2s}), && (4.55)\\
\left\langle \Delta^2 T \right\rangle^{(\text{Fock})} &= \frac{T}{\eta_p \left\langle \hat{n}_p \right\rangle_r} - \frac{T^2}{\left\langle \hat{n}_p \right\rangle_r} T_p. && (4.56)
\end{aligned}$$

For the bTMSS, the measurement needs to be expanded to include the second mode. We have found that a modified form of the intensity difference measurement of the two modes, shown in the bottom of Fig. 4.5, saturates the bTMSS QCRB. The modified intensity difference measurement adds an electronic gain g to the conjugate mode detection[22],

$$\begin{aligned}
\left\langle \Delta^2 \hat{n}_- \right\rangle &= \left\langle (\hat{n}_p - g\hat{n}_c)^2 \right\rangle - \langle \hat{n}_p - g n_c \rangle^2 && (4.57)\\
&= \left\langle \hat{n}_p^2 + g^2 \hat{n}_c^2 - 2g\hat{n}_p\hat{n}_c \right\rangle - \left(\langle \hat{n}_p \rangle^2 + g^2 \langle \hat{n}_c \rangle^2 - 2g \langle \hat{n}_p \rangle \langle \hat{n}_c \rangle \right) && (4.58)\\
&= \left\langle \Delta^2 \hat{n}_p \right\rangle + g^2 \left\langle \Delta^2 \hat{n}_c \right\rangle - 2g \left(\langle \hat{n}_p \hat{n}_c \rangle - \langle \hat{n}_p \rangle \langle \hat{n}_c \rangle \right) && (4.59)\\
&= (T_p T \eta_p)^2 \left\langle \Delta^2 \hat{n}_p \right\rangle_0 + T_p T \eta_p (1 - T_p T \eta_p) \langle \hat{n}_p \rangle_0 \\
&\quad + g^2 \left[\eta_c^2 \left\langle \Delta^2 \hat{n}_c \right\rangle_0 + \eta_c (1 - \eta_c) \langle \hat{n}_c \rangle_0 \right] \\
&\quad - 2g T_p T \eta_p \eta_c \left(\langle \hat{n}_p \hat{n}_c \rangle_0 - \langle \hat{n}_p \rangle_0 \langle \hat{n}_c \rangle_0 \right). && (4.60)
\end{aligned}$$

The electronic gain is optimized for the minimum intensity difference measurement uncertainty, with

$$g_{\text{opt}} = \frac{T_p T \eta_p \left(\langle \hat{n}_p \hat{n}_c \rangle_0 - \langle \hat{n}_p \rangle_0 \langle \hat{n}_c \rangle_0 \right)}{\eta_c \left\langle \Delta^2 \hat{n}_c \right\rangle_0 + (1 - \eta_c) \langle \hat{n}_c \rangle_0}, \tag{4.61}$$

such that the optimized intensity difference uncertainty is given by

$$\left\langle \Delta^2 \hat{n}_-^{g_{\text{opt}}} \right\rangle = (T_p T \eta_p)^2 \left\langle \Delta^2 \hat{n}_p \right\rangle_0 + T_p T \eta_p (1 - T_p T \eta_p) \langle \hat{n}_p \rangle_0 - T_p^2 T^2 \eta_p^2 \frac{\left(\langle \hat{n}_p \hat{n}_c \rangle_0 - \langle \hat{n}_p \rangle_0 \langle \hat{n}_c \rangle_0 \right)^2}{\eta_c \left\langle \Delta^2 \hat{n}_c \right\rangle_0 + (1 - \eta_c) \langle \hat{n}_c \rangle_0}. \tag{4.62}$$

Error propagation of the optimal intensity difference variance for the measurement of an amplitude difference squeezed bTMSS into transmission uncertainty gives

$$\begin{aligned}
\left\langle \Delta^2 T \right\rangle &= \frac{\left\langle \Delta^2 \hat{n}_-^{g_{\text{opt}}} \right\rangle}{\left| \frac{\partial \langle \hat{n}_p - g_{\text{opt}} \hat{n}_c \rangle}{\partial T} \right|^2} && (4.63)\\
&= \frac{\left\langle \Delta^2 \hat{n}_-^{g_{\text{opt}}} \right\rangle}{\left| \frac{\partial T_p T \eta_p \langle \hat{n}_p \rangle_0}{\partial T} \right|^2} && (4.64)\\
&= \frac{T}{\eta_p \left\langle \hat{n}_p \right\rangle_r} - \frac{T^2}{\left\langle \hat{n}_p \right\rangle_r} T_p H_c [1 - \operatorname{sech}(2s)], && (4.65)
\end{aligned}$$

which saturates the QCRB for transmission estimation. The error propagation using only the probe mode, $T_p T \eta_p \langle \hat{n}_p \rangle_0$, is the same as taking the derivative of the total measurement, $\langle \hat{n}_p - g_{\text{opt}} \hat{n}_c \rangle$, as only the probe mode is explicitly dependent on the parameter of interest. While the optimal electronic gain on the conjugate mode does change with transmission, the gain is set independently of it. This is due to the optimal gain being defined as the gain that minimizes the intensity difference noise, not the transmission, and thus it can be found without knowing the transmission value.

The quantum enhancement offered by these quantum states are readily available for current state-of-the-art devices as the measurements listed here are readily accessible with

current technology. When estimating transmission using 100 coherent state photons, for a transmission of 99%, it would take ∼4.6 bTMSS probe photons, ∼2.8 bSMSS photons, or 1 Fock state photon to achieve the same uncertainty, assuming no extraneous losses and $s = 2$ for the squeezed state. Since the bright states are generated with orders of magnitude higher power than the Fock state, they can estimate transmission with orders of magnitude less uncertainty. The next chapter will show that it is possible to saturate the bTMSS QCRB experimentally and therefore enhance the transmission estimation with currently available devices.

Chapter 5

Experimental Saturation of the Transmission QCRB with a bTMSS

Reaching the QCRB for real sensing applications is not a trivial matter. In practical applications there exist many different sources of noise that can increase the estimation uncertainty and the bound can only be saturated by measurements dominated by quantum statistics. Laser systems have technical noise that scales inversely with frequency[53], meaning they do not correspond perfectly to a coherent state. Photodetectors have electronic noise from the thermal effects of resistors[54] that add uncertainty to the measurement. The power output of a laser slowly changes over time as internal components shift and settle in part due to slowly heating up during continual use[55,56]. These and other noise sources increase the uncertainty when trying to estimate transmission.

Saturating the QCRB experimentally requires tight control over the various components of the experiment to correct for technical noise and imperfections as well as finding the estimators and measurements that can saturate the bound. Here, we will show that we can saturate the bTMSS QCRB for transmission estimation. This required us to lock many aspects of our state generation and system properties and precise calibration of every device in the experiment.

5.1 Overview of the experiment

A diagram of the experimental setup is shown in Fig. 5.1. The bTMSS is generated in a ^{85}Rb vapor cell. The probe mode, red, is used to probe the system and the conjugate mode, green, is used as part of the measurement. Just as in the QCRB calculations from the last chapter, the probe mode has imperfect transmission, T_p, between state generation and the system under study and imperfect detection efficiency, η_p. The conjugate mode also has imperfect detection efficiency, η_c. Each of these need to be calibrated to set the QCRB. Due to the way in which we are generating the bTMSS, the theory from the previous chapter needs to be expanded upon in order to include absorption of the probe mode by the Rb atoms during the state generation.

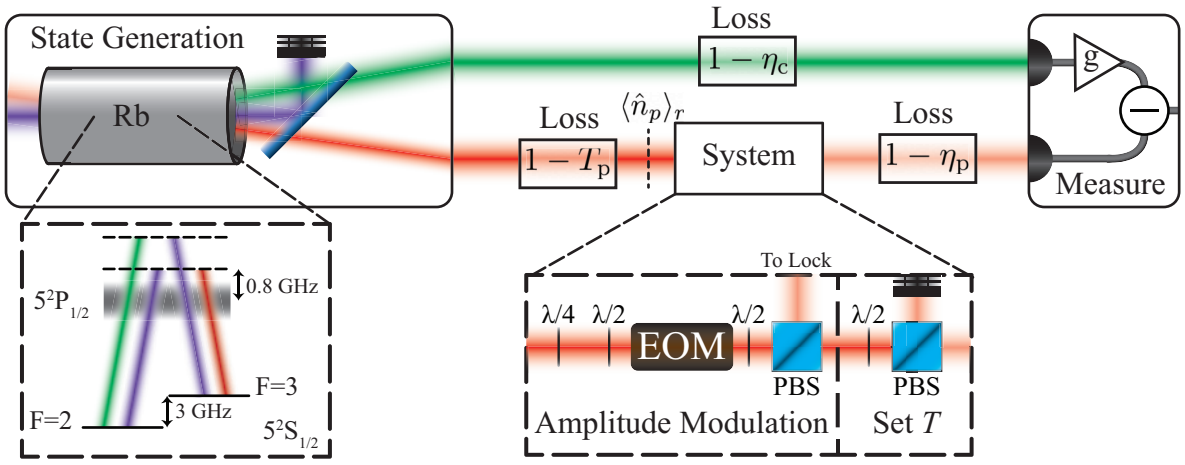


Figure 5.1: For the experiment a bTMSS is generated in a hot ^{85}Rb vapor cell via a four-wave mixing process. As shown in the inset for the state generation, during this process two pump photons, purple, are absorbed and a probe, red, and conjugate, green, photon are generated simultaneously. The probe photons are used to probe the system and the conjugate photons are used as part of the measurement. The probe mode suffers loss before, $1-T_p$, and after, $1-\eta_p$, probing the system; while the conjugate mode suffers loss as well, $1-\eta_c$. The number of photons interacting with the system, $\langle\hat{n}_p\rangle_r$, is taken as the resource for the transmission estimation. The system under study consists of a polarizing beam splitter (PBS) and a half waveplate to set the transmission as well as an electro-optical modulator (EOM) to modulate the transmission. After probing the system, an optimized intensity difference measurement is made. The modulation from the EOM is then used to convert the variance of the measurement into the uncertainty in the estimation of transmission.

The optimized intensity difference measurement, shown in Fig. 4.5 and given by Eq. (4.62), is used to estimate the transmission of the system under study. The system consists of a variable transmission, to show saturation of the bound for a wide range of transmissions, and a transmission modulator, to convert the variance of the measurement into uncertainty in the estimation. As will be explained in further detail later, the change in transmission due to the modulation can be used to find the uncertainty in the estimation of transmission by comparing the measured modulation to the measurement variance.

5.1.1 State generation

For generation of the bTMSS to probe the system and estimate transmission, the squeezing operation, Eq. (2.49), requires a non-linear process such that multiple electric fields interact [30,57]. This allows for the simultaneous generation (absorption) of two photons in different fields. The process used here to generate the bTMSS is four-wave mixing (FWM) [58,51]. The FWM process uses two strong fields, called the pump fields, which act as a photon reservoir. For our work, the pump fields are implemented with a single mode such that the energy for the probe and conjugate photons are taken from this single mode in pairs of photon. Since the pump has much more power then the probe and conjugate modes, it is treated classically

and the statistics of the pump are ignored.

For our experiment, the FWM process is implemented in the D1 line of ^{85}Rb in a hot vapor cell[58,51]. As shown in the energy level inset of Fig. 5.1, the pump field (purple) excites the electrons from the F=2 and F=3 ground energy levels into energy levels, virtual in this case, near the $5^2P_{1/2}$ energy level. Virtual energy levels are short lived and the electrons quickly transition back to the F=2,3 ground energy levels after emitting a probe photon and a conjugate photon. Due to the non-linear nature of this parametric process, both the electron transitions F=2 $\rightarrow$ virtual level $\rightarrow$ F=3 (probe emission) and F=3 $\rightarrow$ virtual level $\rightarrow$ F=2 (conjugate emission) happen simultaneously.

Energy and momentum conservation keep the FWM process dominant over a single lambda transition, such as just the F=2 $\rightarrow$ virtual level $\rightarrow$ F=3 (probe emission). To offset the energy imbalance from a single transition, the atom would receive a momentum kick to add kinetic energy equal to the F=2 to F=3 energy level difference such that the total momentum of the probe photon emitted, pump photon absorbed, and the atom kick conserved momentum. Proper angling of the laser fields and frequency tuning, photon energy, allows for the FWM process to dominate as it is tuned to best match the energy and momentum conservation which does not require the atom to compensate for the energy or momentum mismatch.

To reduce the absorption of each mode, particularly the probe mode, the virtual energy levels need to be set as far away as possible from the $5^2P_{1/2}$ energy level. In principle, the double Lambda configuration of the energy levels should reduce the absorption, but it is not perfect. Care needs to be taken when detuning, as detuning too far from a real energy level reduces the light-atom interaction. Luckily, the absorption process decreases faster with detuning than the FWM process, such that there exists an optimal frequency for high gains from FWM and small losses from atomic absorption. Another complication to reducing absorption comes from vaporizing a large amount of Rb for high squeezing. This is done by heating the atoms in the cell, which unfortunately broadens the atomic energy levels due to the Doppler effects of the fast moving hot vapor. The optimal density of Rb atoms, for maximum squeezing, occurs when our cell is heated to around 120° C. This temperature results from a balance between having enough atoms for the FWM process but not having the atoms so hot that the Doppler broadened probe absorption reduces the squeezing.

To generate a bright squeezed state, we displace only the probe mode to stimulate the FWM process, also known as seeding the process. The seed probe is generated by picking off a portion of the pump mode and is detuned from the pump by 3.04 GHz via double passing through an acousto-optical modulator (AOM), see Fig. 5.2(a). Since the wavelength of the modes change slightly due to the frequency dependence of the Rb refractive index, the momentum conservation changes as

$$\hbar\vec{k}^{\mathrm{Rb}}_{\mathrm{probe}} + \hbar\vec{k}^{\mathrm{Rb}}_{\mathrm{conj}} = 2\hbar\vec{k}^{\mathrm{Rb}}_{\mathrm{pump}} \tag{5.1}$$

$$\hbar n_{\mathrm{probe}}\vec{k}^{0}_{\mathrm{probe}} + \hbar n_{\mathrm{conj}}\vec{k}^{0}_{\mathrm{conj}} = 2\hbar n_{\mathrm{pump}}\vec{k}^{0}_{\mathrm{pump}}, \tag{5.2}$$

where $\vec{k}^{\mathrm{Rb}}_{\mathrm{mode}}$ is the wavenumber for the mode in Rb, $\vec{k}^{\mathrm{Rb}}_{\mathrm{mode}}$ for vacuum, and n_{mode} is the refractive index for the mode in light. As shown in Fig 5.2(b), this causes the angle between

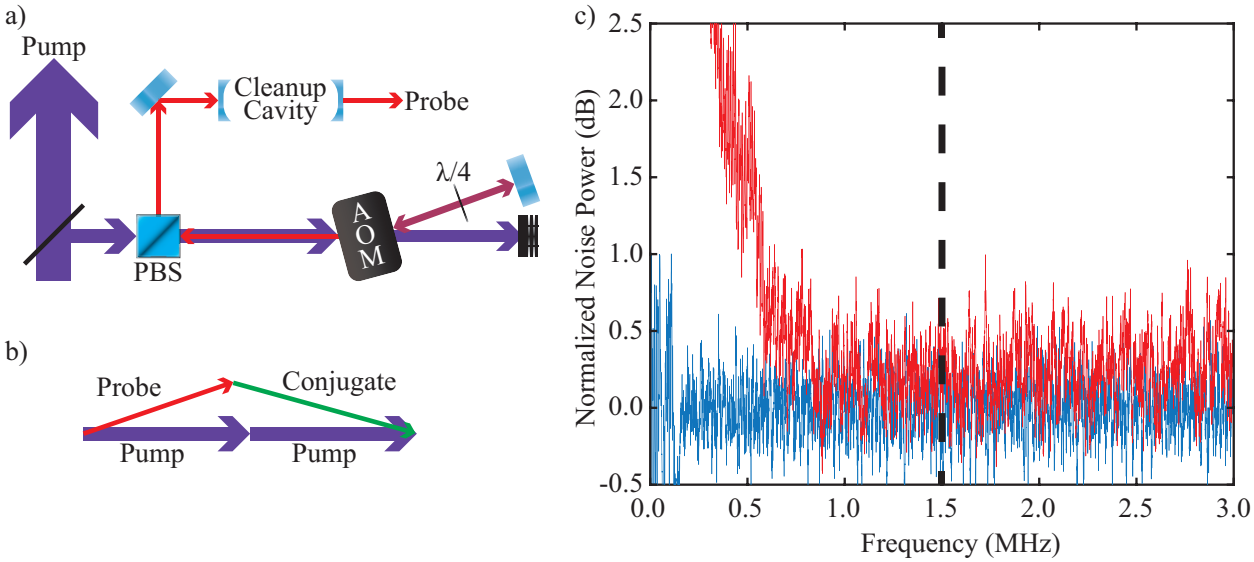


Figure 5.2: The probe is detuned from the pump by double passing through an acousto-optical modulator (AOM) as shown in (a). In the Rb cell, the probe, conjugate, and pump have slightly different refractive indices due to being close to atomic resonance with the fields at slightly different frequencies. Thus, the probe and pump modes cross at an angle as shown in (b) in order to conserve momentum. After the AOM, the seeding for the probe mode is passed through a cleanup cavity in order to reduce the intensity noise of the beam to the shot noise level at 1.5 MHz. This is shown in (c) where the shot noise (blue) and the seed noise (red) noise power is plotted. The noise power is normalized by shot noise and shown on a log scale such that 0 dB corresponds to the shot noise.

the pump and probe mode in the ^{85}Rb cell to be 0.4° for momentum conservation.

For the FWM process, the pump mode has a power of 600 mW and $1/e^2$ waist radius of 700 μm. The probe mode has an initial power of 7 μW and $1/e^2$ waist radius of 400 μm. The waist of each mode crosses at the center of the cell. The laser waist is the location of the smallest beam size and is also the location of a flat wavefront, such that the mode approximates a plane wave. The cell is kept to 1/2 in (13 mm) in length, so the relative phases of the pump, probe, and generated conjugate beam do not change and the squeezing angle is constant throughout the cell. Propagation through a long cell would cause the squeezing angle to rotate due to the small difference in refractive index for each mode and eventually fully reverse the FWM process such that photons are absorbed in pairs, one each from the probe and conjugate modes, and added to pump mode.

Unlike in the theory, the probe mode seed is not a perfect coherent state due to technical noise fluctuations from the laser. However, the noise fluctuations of a laser can approximate a coherent state at a high enough analysis frequency. This occurs when the analysis frequency is well outside the bandwidth of any technical noise sources and only the quantum fluctuations of the light remain. To suppress the noise on the probe mode, and effectively reduce the frequency at which the technical noise dominates, the probe is filtered through a cleanup cavity (Newport SuperCavity model SR-140-C) after the AOM. The cavity acts like a low

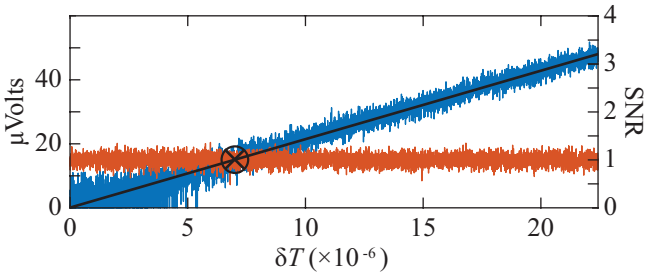


Figure 5.3: Sample noise trace from the measurement of the optimized intensity difference, red, and the modulation from the signal trace, blue, plotted in standard deviation, μVolts, as the transmission modulation standard deviation is ramped. The traces are recorded using a spectrum analyzer with zero span, *i.e.* time trace of a single frequency, at an analysis frequency of 1.5 MHz and resolution bandwidth of 51 kHz. The signal to noise ratio (SNR) of the two plots is shown on the right and a linear fit of the signal is shown in black. At the circled X, the measured modulation voltage is equal to the noise voltage of the measurement. The transmission modulation that creates a signal of the same voltage as the noise gives the transmission estimation standard deviation for our measurement.

pass filter with a linewidth of <0.6 MHz. After the cavity, the probe mode approximates a coherent state at an analysis frequency of 1.5 MHz as shown in Fig. 5.2(c).

All together, the FWM process achieves a probe gain of 11.4 for ∼80 μW of probe power with which to probe the system under study. The balanced intensity difference noise of the generated bTMSS is squeezed 8.0 dB below an equivalent coherent state noise at the analysis frequency of 1.5 MHz.

5.1.2 Converting variance of measurement to transmission uncertainty

To find the uncertainty in transmission estimation, the measurement variance is compared to a ramped transmission modulation in order to find a change in transmission equal to our measurements limit in estimating such changes. As we will show, this is equivalent to error propagating our measurement variance into transmission uncertainty. However, we use an external modulation in order to make a strong argument that our measurement is at the QCRB for transmission estimation. Since the modulation is unrelated to our measurement apparatus, we can compare to our measurement results as an external reference. The transmission modulation in our system is completely independent of our measurement and the settings of the photodiodes and spectrum analyzer used to record the measurement results. How this modulation is generated is covered in the next subsection. Here, we shall cover how the transmission modulation is used to find the transmission uncertainty.

For each set at each transmission, two traces are recorded on the spectrum analyzer. A noise trace of measurement noise power, which is proportional to the variance, of the state without modulation and a signal trace that records the measurement with an additional ramped transmission modulation power. These two traces are used to error propagate the

noise power of the measurement into transmission uncertainty. This is done by finding the point at which the noise power of the measurement is equal to the power of the modulation, as shown in Fig. 5.3. The transmission modulation variance at that point is the same as the transmission uncertainty using the measurement.

To show this mathematically[37], let us examine how a transmission modulation, δT, creates a modulation on the measurement, M,

$$\delta M = \delta T \left| \frac{\partial M}{\partial T} \right|, \tag{5.3}$$

where δM is the modulation measured on the signal trace and $\frac{\partial M}{\partial T}$ is the dependence of the measurement on the transmission. Since the amplitude of the transmission modulation is ramped linearly over time, we define the signal-to-noise ratio (SNR) as the ratio of the modulation standard deviation, δT, to the standard deviation of the measurement. The SNR for the measurement is the same as the one for the tranmission modulation, that is

$$\mathrm{SNR} = \frac{\delta M}{\langle \Delta M \rangle} = \frac{\delta T \left| \frac{\partial M}{\partial T} \right|}{\langle \Delta M \rangle} = \frac{\delta T}{\langle \Delta T \rangle}, \tag{5.4}$$

where $\langle \Delta M \rangle$ and $\langle \Delta T \rangle$ are the standard deviations of the measurement and transmission estimation, respectively. As can be seen from Eq. (5.4), when the SNR= 1, the modulation standard deviation is equal to the estimation standard deviation,

$$\frac{\delta T|_{\mathrm{SNR}=1}}{\langle \Delta T \rangle} = 1 \tag{5.5}$$

$$\delta T|_{\mathrm{SNR}=1} = \langle \Delta T \rangle \,. \tag{5.6}$$

In this way, it can also be shown that finding the modulation that gives a SNR=1 is equivalent to error propagation of the measurement noise into estimation uncertainty[37]. We can see this by squaring Eq. (5.4) such that

$$\frac{\delta T^2|_{\mathrm{SNR}=1} \left| \frac{\partial M}{\partial T} \right|^2}{\langle \Delta^2 M \rangle} = 1 \tag{5.7}$$

$$\delta T^2|_{\mathrm{SNR}=1} = \langle \Delta^2 T \rangle = \langle \Delta^2 M \rangle \left| \frac{\partial M}{\partial T} \right|^{-2}. \tag{5.8}$$

Thus, in Fig. 5.3, the transmission modulation where the blue signal is equal the mean noise in red, marked with a circled X, is the point where the modulation variance is the same transmission uncertainty of the measurement.

For each transmission, the measurement variance is converted into transmission uncertainty using the SNR. For each signal trace, the modulation is set the maximum amplitude for 2 seconds to stabilize the modulation due to ringing. This is due to a large change in the driving power of the system modulation causing extraneous fluctuation in the transmission modulation. The modulation is then ramped down over 14 seconds to scan over multiple SNR values.

When the signal trace is recorded, it does not contain just the modulation power, but the measurement noise power as well. Since the signal and noise of the measurement are not correlated, to get just the modulation power the mean of the noise trace is subtracted from the signal trace. At low SNR, the signal trace can dip below the mean of the noise trace due to the signal trace being dominated by the noise power fluctuations. At this point, the signal trace and jump above and below the mean of the noise trace, just as the points of the noise trace jump above and below. Thus, we take the SNR as the real part of the square root of the pure signal power divided by the mean noise power with the electronic noise power subtracted out. It should be noted that in order to get the correct SNR, the traces must be recorded in power as the pure signal and measurement noise only add in power. If the traces are recorded in log-power or voltage, a correction factor must be applied to the traces to get the correct SNR[59,60].

The SNR is fitted to a line as a function of the transmission modulation standard deviation, to find the transmission modulation where the SNR= 1. Only the slope of the line is a free parameter to fit as the intercept is set to zero since there should be no signal when there is no modulation. The modulation standard deviation at SNR= 1 is given by the inverse of the slope,

$$\begin{aligned} \mathrm{SNR} &= \mathrm{slope} \times \delta T, & (5.9)\\ 1 &= \mathrm{slope} \times \delta T|_{\mathrm{SNR}=1}, & (5.10)\\ \frac{1}{\mathrm{slope}} &= \delta T|_{\mathrm{SNR}=1}. & (5.11) \end{aligned}$$

Using the inverse of the slope instead of the point of the trace closest to the SNR= 1 value removes the digitization noise from the data points. The fitting also allows for every point in the modulation ramp to be used in calculating the transmission uncertainty since a SNR= x for any value of x can be used to find the transmission uncertainty as

$$\delta T^2|_{\mathrm{SNR}=x} = x \left\langle \Delta^2 T \right\rangle . \tag{5.12}$$

Thus, all points along the ramp of the signal trace can in principle be used to find the transmission uncertainty. However, the points where the signal trace had values below the mean noise power are excluded as they bias the slope fitting towards zero due to taking the real part in the SNR.

5.1.3 System

To simulate the transmissive system under study, we use a half waveplate and PBS to set the transmission and an electro-optical modulator (EOM) in the amplitude modulation configuration to modulate it. The half waveplate and PBS are used to show the transmission dependence of the estimation uncertainty and saturation of the QCRB over a wide range of transmission values. The EOM adds the transmission modulation used to convert the measurement variance into transmission uncertainty.

The EOM crystal creates a phase delay between two polarization components of light defined by the EOM crystal axes[61]. A voltage applied along one of the crystal axes changes the refractive index for light polarized along that axis. This difference in refractive index between the two crystal axes adds a phase delay between the polarization axes of the indecent light, changing the polarization of the input light. Modulating the applied voltage also applies a modulation to the polarization. A half waveplate and PBS after the EOM crystal transforms the polarization modulation between the two polarization into amplitude, and thus transmission, modulation.

The transmission through the EOM in the amplitude modulation configuration changes with an applied voltage, V, as[61]

$$T(V) = T_{\max} - (T_{\max} - T_{\min}) \sin^2(C_\lambda V) \tag{5.13}$$

$$= T_{\max} - \frac{T_{\max} - T_{\min}}{2}[1 - \cos(2C_\lambda V)], \tag{5.14}$$

where $T_{\max(\min)}$ is the maximum (minimum) transmission through the EOM and C_λ is an optical wavelength dependent constant that characterizes the response of the EOM crystal to the applied voltage. To set the maximum and minimum transmission of the amplitude configuration, a quarter and a half waveplate are placed before the EOM crystal to give complete control of the polarization of the light into the EOM crystal. Thus, the maximum and minimum transmission through the EOM can be set and the response of the EOM to the applied voltage can be controlled as shown in Fig. 5.4.

For a transmission modulation to have a linear response to an applied voltage modulation, the EOM needs to operate near the mean transmission $\bar{T} = \frac{T_{\max}+T_{\min}}{2}$ where $\cos(2C_\lambda V) \approx 2C_\lambda V$. The greater the difference between the maximum and minimum transmission, the larger the transmission modulation for the same voltage signal. The red line in Fig. 5.4 is the linear response of the EOM around the mean transmission. If the applied voltage modulation is too large, the response becomes nonlinear. This occurs for voltages for which the red line no longer lines up with the blue line of the full response. When applying a sinusoidal voltage to the EOM in the linear regime, the transmission can be modeled as

$$T_{\text{EOM}} = \bar{T} + \sqrt{2}\,\bar{T}\delta_T \sin(2\pi f t), \tag{5.15}$$

where f is the frequency of the applied voltage modulation and thus of the transmission modulation while in the linear regime, and t is time. The δ_T term is the modulation "kernel" such that the standard deviation is given by $\bar{T}\delta_T$. The response of the EOM to a voltage modulation is shown in black in Fig. 5.4. The kernel depends linearly on the amplitude of the voltage modulation and is used to control the transmission modulation.

For the experiment, we wish to show saturation of the QCRB for transmission estimation for a wide range of transmissions. To maximize this range, the mean transmission of the EOM must to be as high as possible as it sets the maximum mean transmission for the system. The waveplate and PBS are then used to lower the mean transmission through the system. However, if the mean transmission of the EOM is too high, *i.e.* nearly equal to the maximum EOM transmission, then the linear regime will be extremely small and

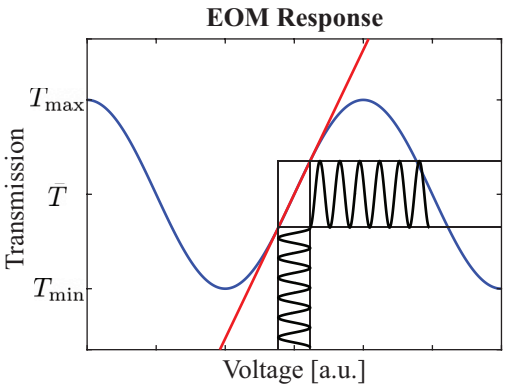


Figure 5.4: The EOM transmission response to an applied voltage. The blue line is the full sinusoidal response of the transmission as a function of the applied voltage, while the red line indicates the linear approximation of the response. The range over which the red and blue lines overlap is the linear regime. A voltage modulation applied in the linear regime creates a transmission modulation at the same frequency. The amplitude of the transmission modulation depends linearly on the amplitude of the voltage modulation and the slope of the response.

a detectable transmission modulation will need to be outside the linear regime. Thus we need to balance between having a high mean transmission through the EOM and having a sufficiently large linear regime over which to modulate the transmission. For this experiment we have found that $T_{\max} = 0.848$ and $T_{\min} = 0.832$ allows for the EOM modulation needed for the experiment to be well within the linear regime while still maximizing the possible transmission values.

As part of the measurement process, the transmission modulation needs to be well known at all times. To keep a tight control, the modulation kernel is locked, as explained in the next subsection, and the transmission modulation is calibrated such that δ_T is known at all points along the signal trace. For each transmission value, the standard deviation of the modulation is the modulation kernel times measured transmission of the system, T,

$$\delta T = T\delta_T, \tag{5.16}$$

where $T = \bar{T}T_{\text{adj}}$ and T_{adj} is the transmission through the waveplate and PBS after the EOM used to adjust the system transmission. This change in modulation with the system transmission is due to transmissions combining multiplicatively.

5.1.4 Results

The results of the experiment are shown in Fig. 5.5. Here, we looked at the mean transmission from $\sim$ 85% to 10% in steps of 5%. At 84% transmission, the absolute transmission uncertainty when probing with a bTMSS is $1.11 \pm 0.01 \times 10^{-10}$ for our measurement. In order to build the statistics for this data, twenty sets of measurements are taken for each transmission. To rule out drifts in the state over time, the transmission uncertainty measurements are made from $\sim$ 85% transmission to 10% transmission then back to $\sim$ 85% for the next set instead of all measurements of one transmission done at once then moving to the next. This greatly reduces the possibility that the change in transmission uncertainty is due to

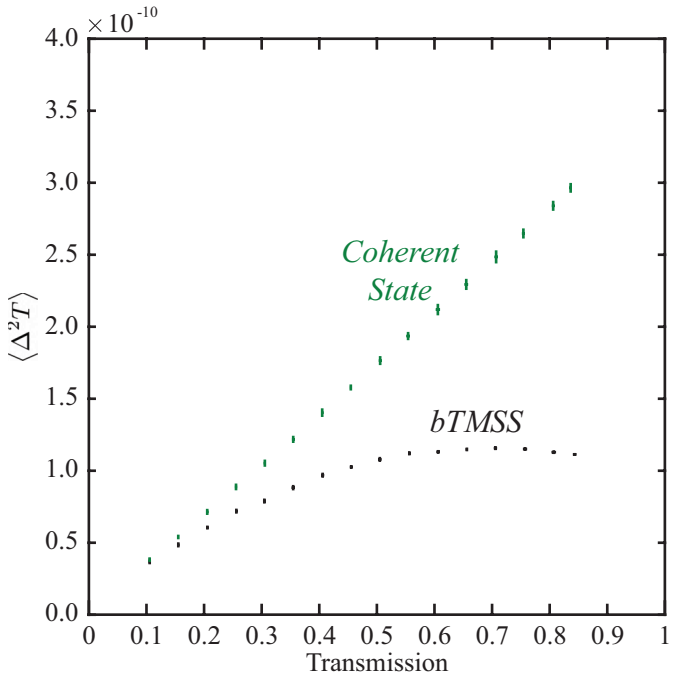


Figure 5.5: Results of the bTMSS transmission estimation uncertainty experiment. Here we plot the transmission uncertainty against the mean transmission of the system. The black points are the bTMSS measurement results with one standard deviation horizontal error bars for the mean transmission and vertical error bars for the transmission uncertainty. Similarly, the green points are for the coherent state with error bars in the mean transmission and the uncertainty in the transmission estimation.

changes in the generated state instead of changes in the transmission value. The experiment is repeated with a coherent state, green data points and dashed orange line QCRB. This is done as a check on the experimental procedure and to show the quantum enhancement from using the bTMSS. At the maximum transmission through the system of 84% the bTMSS is able to estimate the transmission with 62% less uncertainty than the coherent state with the same number of probing photons.

To consistently return to the same transmission set after set, the transmission for each data point was set using an electronically controlled rotation mount to rotate the waveplate in the "Set T" part of the system, see Fig. 5.1. After setting the transmission, the probe beam was sent on a path around the system to measure the initial probe power. The ratio of the probe power around the system and through the system sets the transmission for the measurement. This is done for every transmission for every set and is also used to check that the probe power is consistent throughout the experiment.

For the optimized intensity difference measurement, the optimal electronic gain is dependent on the transmission of the system under study, Eq. (4.61). Thus, for each transmission, the electronic gain is set during the first set of transmissions and is returned to for all subsequent sets. To find the optimal gain, a series of quick unbalanced intensity difference measurements are made with guessed gain values to find a range of possible optimal gains. Then, for each possible optimal gain, a careful measurement is made and the electronic noise power for that measurement, previously calibrated for each gain, is subtracted from the measurement. The noise power of the measurement and the noise power of the electronics of the detection apparatus are uncorrelated and thus can be subtracted out to leave the noise power of the measurement itself. This process is repeated until the optimal gain is

determined when the lowest unbalanced intensity difference measurement noise is achieved. That gain is recorded and used again for each repeat of the transmission value for all 20 sets. The gain is found 16 times, once for each mean transmission of the experiment.

In the next section, we will go over how we are able to keep control over our state and system to take the data in Fig. 5.5. Afterwards, we will show how the system is calibrated such that we were able to find the transmission uncertainty. Next, we will calibrate the measurement to also count the number of photons used to collect the data such that we can compare our results to theory like in Fig. 4.4. Finally, we will show how to calculate the QCRB for our state and show that our measurement results saturate the bound

5.2 Control

It takes many measurements to get the data to build statistics of the transmission estimation and show that the estimation uncertainty saturates the QCRB. To probe the same system under study with the same state over the 20+ hours needed to perform the experiment, we use multiple feedback controllers to lock the pump power, probe seed power, cell temperature, and laser frequency. This keeps the bTMSS probing power and squeezing level consistent over a long period of time, *i.e.* same covariance matrix and displacement vector. The transmission modulation is kept repeatable as well such that the transmission modulation to find the SNR is never out of calibration during the experiment.

5.2.1 Transmission modulation control

To lock the transmission kernel, see Eq. (5.15), to a specific value, the reflection from the amplitude modulation configuration PBS is measured, as shown in Fig. 5.6. The detected signal is split into two parts, a low frequency DC portion and a high frequency AC portion. The DC portion of the detected reflection is used keep the EOM response at the center of the linear regime by applying a voltage offset while the AC portion is used to lock the modulation amplitude by adjusting the applied modulation voltage amplitude.

The AC portion is used to control the modulation kernel. We lock the modulation kernel and not the modulation amplitude as the kernel does not change with mean transmission like the modulation amplitude. To generate an error signal, the AC portion is demodulated at 1.5 MHz, the frequency of the transmission modulation. This is done by mixing the AC signal with an electronic local oscillator such that

$$V_{LO}\cos(2\pi f_{LO}t+\phi)\times V_{AC}\cos 2\pi ft=\frac{V_{LO}V_{AC}}{2}\left\{\cos([f-f_{LO}]t-\phi)+\cos([f+f_{LO}]t+\phi)\right\} \tag{5.17}$$

where V_{LO} and V_{AC} are the voltage amplitudes of the local oscillator and AC signal, respectively and f_{LO} is the frequency and ϕ the phase of the local oscillator. The phase is with respect to the AC signal. Using a low pass filter to remove the frequency sum term and setting the frequency and phase of the local oscillator to be the same as the AC signal gives an output that is proportional to the transmission modulation kernel, $\frac{V_{LO}V_{AC}}{2}$. The lockpoint

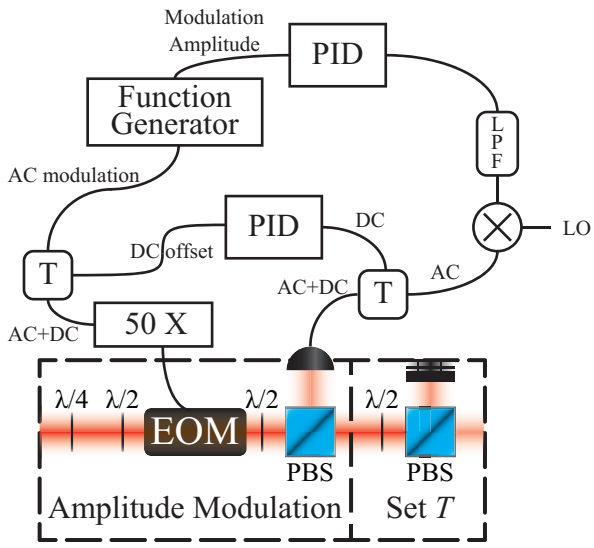


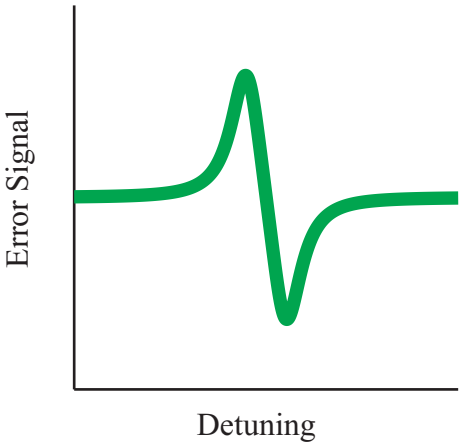
Figure 5.6: Diagram for the locking of the EOM. Expanding on the "System" inset of Fig. 5.1, the detected light from the EOM reflection is split into AC and DC components using a bias T. The AC portion is mixed down with a LO and passed through a low pass filter (LPF) to create an error signal that is proportional to the transmission modulation amplitude. A PID lock, which stands for Proportional-Integral-Derivative, uses this error signal to control the modulation amplitude of the input voltage into the EOM. The DC portion of the reflection is sent directly to the PID lock to generate a DC offset to keep the EOM at the center of the linear regime. The AC modulation and DC offset are combined with another bias T and amplified 50 X before being sent to the EOM.

for the modulation kernel is set via a function generator such that it can be controllably changed during the experiment to find the uncertainty in the transmission estimation, see Sect. 5.1.2. The feedback control output is sent to the voltage modulator to control the amplitude of the modulation output going to the EOM.

The DC portion of the detected reflection is also the error signal for the linear regime lock. The feedback control is used to shift the voltage offset of the modulation to keep the EOM at the center of the linear regime, shown in Fig. 5.4. When shifted away from the center, the transmission modulation decreases for a given voltage amplitude due to a change in the slope response. Since the EOM lock is from the reflection, the DC voltage needs to be constant throughout the experiment in order for the transmission modulation to be repeatable. If we had picked off a bit of the transmission from the EOM to do the lock, a shift in the DC portion, and thus a change in the EOM response, could be correctly compensated for by increasing or decreasing the modulation amplitude. However, using the reflection the AC lock will compensate in the opposite direction that it should for changes in the DC portion. On the other hand, the reflection gives a much greater AC error signal than picking off part of the transmission and allows for a greater maximum mean transmission for the experiment.

PID control boxes are used to lock both the AC and DC signals and a bias T is used to combine the output from the DC lock and the voltage modulation. This offset modulation is then amplified by 50x using a high power amplifier and sent to the EOM. With this lock system, the transmission modulation is repeatable from measurement to measurement and the amplitude of the transmission modulation is known at all times.

Figure 5.7: Error signal from the PDH. Due to the phase difference between the left and right detuned modulation, the detected modulation flips sign across zero detuning. This generates a derivative like error signal used to lock the cavity to the laser.



5.2.2 State control

For the bTMSS, the pump and probe seed powers are locked by sampling part of each beam before the Rb cell. The probe power is sampled using a beam splitter and controlled via the AOM used to detune it from the pump beam. By decreasing the amplitude of the acoustic modulation of the AOM, the efficiency of the frequency conversion is reduced, lowering the probe power. Increasing its amplitude increases the probe power. To lock the pump power, part of the pump is picked up via a beam sampler. The detected power is kept steady by using a polarizing beam splitter (PBS) and a half waveplate in an electronically controlled rotation mount. Rotating the waveplate with the mount changes the transmission through the PBS and thus the pump power. This method is much slower than the probe power control, however the FWM process is not sensitive to fast pump power fluctuations and this feedback scheme was quick enough to compensate for the slow thermal drift of the pump power.

The cell temperature controls the density of Rb atoms in the vapor cell. Higher temperature leads to a higher density, which allows for higher gain of the FWM process, but also increases the rate of other processes as well, such as probe absorption. The squeezing of our bTMSS is optimal at around 120° C and we controlled the cell temperature to < 0.1° C using a PID temperature controller.

The laser frequency is locked by measuring the conjugate power after the Rb vapor cell. Since the pump, probe seed power, and cell temperature are locked, the only way the gain of the FWM process can change is from frequency drift of the involved fields. The probe frequency is shifted by 3.04 GHz from the pump frequency by the AOM and thus only the pump frequency needs to be locked. Changes in the conjugate power serves as the error signal for frequency shifts, as the FWM gain, and thus the conjugage power, will change with frequency. The probe power could also be used, but the change in the system transmission would need to be compensated for. Thus, the conjugate is the better choice for locking the laser frequency.

The cleanup cavity, used to make the probe seed resemble a coherent state, is locked to the probe frequency using the Pound-Drever-Hall (PDH) technique[62]. This technique

is used as the cavity needs to be locked where the power out is maximized. As such, a shift in the cavity resonance frequency in either direction lowers the transmission. The PDH technique creates a derivative error signal that can differentiate the direction of the frequency shift. To generate the derivative signal from the cavity reflection, an EOM applies a phase modulation at 10 MHz to the probe beam. This modulation is an order of magnitude outside the linewidth of the cavity, < 0.6 MHz, and is not transmitted. The reflection from the cavity is then detected and is mixed with a 10 MHz electronic local oscillator (LO) to demodulate similarly to what is done for the EOM AC lock, see Eq. (5.17). After filtering out the frequency sum term, the error signal is

$$\text{error signal} = \frac{V_{\text{LO}} V_{ref}}{2} \cos(\phi_{\delta f}) \tag{5.18}$$

where V_{ref} is the voltage amplitude of the detected modulation and $\phi_{\delta f}$ is the phase difference between the modulation and the LO. This phase depends on the difference in frequency, δf, between the resonance frequency of the cavity and the frequency of the incident light up to a difference of π between the light frequency well above and well below the resonance frequency of the cavity. As shown in Fig. 5.7, this is what gives the derivative like error signal. As the frequency of the light moves away from resonance with the cavity, shifting higher or lower, shifts the phase in the opposite direction and gives a positive or negative error signal voltage.

5.3 Calibration

With tight control over the state and system, the next step is calibrating exactly what modulation amplitude or what bTMSS are being generated throughout the experiment. In addition, in order to compare the experimental results to the expectations from the theory, we need a way to count the number of photons used in the measurement.

5.3.1 EOM calibration

To calibrate the modulation kernel for a given AC lockpoint, the measured oscillating probe power is read on an oscilloscope and the lockpoint is changed from 300% of the maximum lockpoint during the experiment to 40% in steps of 20%. At each lockpoint, multiple oscillations of the modulation are recorded. The probe power during the calibration is given by

$$\begin{aligned} P(t) &= P_{in} T_{\text{EOM}} T_{\text{adj}} \eta_p & (5.19) \\ &= P_{in} \left[\bar{T} T_{\text{adj}} \eta_p + \sqrt{2} \bar{T} T_{\text{adj}} \eta_p \delta_T^{(lp)} \sin(2\pi f t) \right], & (5.20) \end{aligned}$$

where P_{in} in the input power, η_p is the detection efficiency of the probe mode, and $\delta_T^{(lp)}$ is the kernel for a given lockpoint. During the analysis, the mean power of the probe mode is

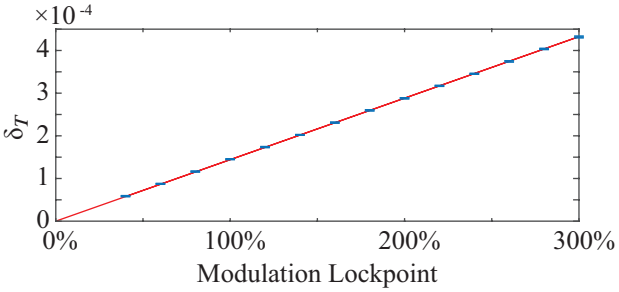


Figure 5.8: The EOM transmission modulation kernel, δ_t, is calibrated as a function of the EOM modulation lockpoint. The lockpoint is scanned from 300% of the maximum lockpoint used in the measurement to 40%. The blue data points show the 1 standard deviation error bars for the calibration and the red line is the linear fit. The transmission modulation is well within the linear regime of the EOM voltage response since a lockpoint 3x higher than the experimental value is still linearly related to the modulation kernel.

calculated for each trace and subtracted from the recorded trace. The remaining modulation term is then divided by the mean value such that the trace is

$$\text{trace}(t) = \sqrt{2}\delta_T^{(lp)} \sin(2\pi f t). \tag{5.21}$$

The amplitude of the trace is calculated using a fast fourier transform (FFT). Using an FFT instead of fitting parameters to the function allowed for a more precise estimation of the modulation kernel that is not affected by oscillations or noise at other frequencies. The results of the calibration are shown in Fig. 5.8 with the one sigma vertical error bars for the kernel shown in blue and the linear fit for the modulation kernel as a function of the lockpoint shown in red. The modulation is well within the linear regime as the linear fit matches for a lockpoint three times higher than what is used in the experiment.

5.3.2 Photon flux to photon number conversion

The QCRB sets the lower bound for a given *number* of probing photons. For the experiment, the state generated is a continuous wave with a set photon *flux* in the probe mode. In order to compare the transmission estimation results with the bound, the photon flux of our state must be converted into a photon number given an effective detection time.

For a given photon flux Φ, the power, P, of the light beam is[29,30]

$$P = \Phi \frac{hc}{\lambda}, \tag{5.22}$$

where c is the speed of light, h is Plank's constant, and λ is the wavelength of the laser. When the light is detected on a photodiode, the photodetector gives a voltage reading with a linear relation to the power such that $V_{\text{pd}} = mP$, where m is the conversion factor. The conversion factor, m, is calibrated using a power meter on a flip mount moved in and out of the probe detected by the photodetector for multiple different powers. The number of photons used in a measurement is then

$$\langle \hat{n}_p \rangle_r = \Phi_p t_e = \frac{\lambda_p}{hc} \frac{t_e}{m} V_{\text{pd}}, \tag{5.23}$$

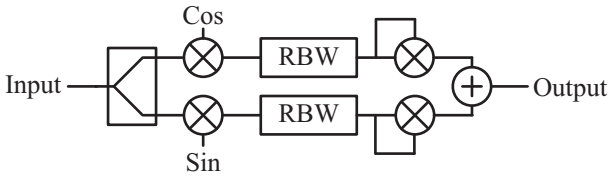


Figure 5.9: Spectrum analyzer model used in the calculations. The Input is split into the in-phase and out-of-phase paths to be mixed with a Sine wave or Cosine wave LO, respectively. After mixing, each path is filtered by the RBW filter and then squared via a mixer. The two paths are summed and the output of the spectrum analyzer is the variance of the input, up to some scaling factor k.

where t_e is the effective time of the measurement.

The effective measurement time is based on the bandwidths of the various parts of the measurement apparatus. Each point on the noise and signal traces from the spectrum analyzer depend on the photon flux at the time of recording and the response time of the measurement apparatus. For an ideal apparatus, the response time for a point in the spectrum analyzer trace would have a sharp cutoff at the detection $\pm t/2$[63]. However, a real response does not sharply end but instead steadily reduces to zero. The effective time, t_e, of a measurement is defined as the width of a rectangular, sharp cutoff measurement response time equivalent to the response time of the actual measurement, such that the total number of photons for the measurement is the same for each response.

For our experiment, the effective time is dominated by the resolution bandwidth (RBW) of the spectrum analyzer. This is due to the RBW being much smaller, and thus have a longer response time, than any other bandwidths, such as the photodetector bandwidth or the spectrum analyzer analog-to-digital conversion bandwidth. It should be noted that we do not consider the video bandwidth (VBW) smoothing of the trace. This smoothing is turned off to simplify the time calculations as the VBW would correlate the points in the trace, increasing the effective measurement time[59,60].

To find the effective measurement time, we will use the photon number statistics of the coherent state. The noise power of a coherent state intensity measurement will be error propagated into photon number variance. As will be shown below, this error propagation will give the effective time as a function of the RBW. The first part of the calculation is to find the electronic gain of the spectrum analyzer, such that it can be removed and the output of the spectrum analyzer is the actual variance of the input.

Deterministic signal to remove electronic gain

The basic operation of a spectrum analyzer is given in Fig. 5.9. An input signal is split into two paths, an in-phase path, I, and an out-of-phase path, Q. The in-phase path is the upper one in Fig. 5.9 and is mixed with a LO of a set phase. The out-of-phase path mixes the signal with a LO 90° out of phase with the in-phase LO. These LOs are represented by the sin and cos inputs into the mixers shown in Fig. 5.9. After mixing with the LO in either path, the signal passes through a low pass filter, the RBW filter, and is then squared. Both paths are then summed together to create the output. The output $I^2 + Q^2$ scales

with the variance of the input signal. Unlike the measurement response time, this scaling of the output with the input variance has no effect on the number of photons used in the measurement as multiplying the signal and noise traces by a scalar value after measurement does not change the number of photons used to generate the traces. However, the scaling factor can affect our calculations, and so needs to be found. This can be done by calculating the output of a deterministic signal through the spectrum analyzer.

For an arbitrary, deterministic signal, $A\sin(2\pi ft+\phi)$, with variance $\frac{A^2}{2}$, the output will be $k\frac{A^2}{2}$, where k is some scaling factor. Going through the spectrum analyzer, the input signal is first split by a factor z such that the amplitude is A/z for I and Q. The splitting is kept arbitrary such that the effects of the splitter can be examined.

After mixing with the local oscillator, path I is

$$\begin{aligned} I &= \frac{A}{z}\sin(2\pi ft+\phi)\sin(2\pi f_L t) && (5.24)\\ &= \frac{A}{2z}\Big\{\,[\cos(2\pi f_- t)-\cos(2\pi f_+ t)]\cos(\phi)-[\sin(2\pi f_- t)-\sin(2\pi f_+ t)]\sin(\phi)\Big\}, && (5.25)\end{aligned}$$

and similarly path Q is

$$Q = \frac{A}{2z}\Big\{\,[\sin(2\pi f_- t)+\sin(2\pi f_+ t)]\cos(\phi)+[\cos(2\pi f_- t)+\cos(2\pi f_+ t)]\sin(\phi)\Big\}, \quad (5.26)$$

where $f_\pm = f \pm f_L$ are the sum and difference frequencies from the mixer and f_L is the frequency of the LO. The paths then are convolved in the time domain with the RBW filter with a frequency response $H(f)$. The impulse response of the filter is given by

$$h(t)=\int_{-\infty}^{\infty} H(f)e^{2\pi ift}df. \quad (5.27)$$

Note that we are working with linear frequencies instead of radial, $2\pi f$, such that there is no $\frac{1}{2\pi}$ term to consider for the Fourier transform. The in-phase path after convolution with the RBW is

$$\begin{aligned} I &= \frac{A}{2z}\int_{-\infty}^{\infty} d\tau\Big\{\,[\cos(2\pi f_- t)-\cos(2\pi f_+ t)]\cos(\phi)\\ &\qquad -[\sin(2\pi f_- t)-\sin(2\pi f_+ t)]\sin(\phi)\Big\}h(t-\tau) && (5.28)\\ &= \frac{A}{4z}\int_{-\infty}^{\infty} df\Big\{\big[\delta(f_- -f)H(f)e^{2\pi ift}+\delta(f_- +f)H(f)e^{2\pi ift}\\ &\qquad -\delta(f_+ -f)H(f)e^{2\pi ift}-\delta(f_+ +f)H(f)e^{2\pi ift}\big]\cos(\phi)\\ &\qquad -\frac{1}{i}\big[\delta(f_- -f)H(f)e^{2\pi ift}-\delta(f_- +f)H(f)e^{2\pi ift}\\ &\qquad -\delta(f_+ -f)H(f)e^{2\pi ift}+\delta(f_+ +f)H(f)e^{2\pi ift}\big]\sin(\phi)\Big\} && (5.29)\end{aligned}$$

Let us assume that $H(f_+) = 0$ so that the RBW filter filters out the frequency sum term from the LO mixer. In this way, the spectrum analyzer picks out only the terms near the LO frequency. With this assumption, the in-phase path simplifies to

$$\begin{aligned} I &= \frac{A}{4z}\Big\{ \left[H(f_-)e^{2\pi i f_- t} + H(-f_-)e^{-2\pi i f_- t}\right]\cos(\phi) \\ &\quad -\frac{1}{i}\left[H(f_-)e^{2\pi i f_- t} - H(-f_-)e^{-2\pi i f_- t}\right]\sin(\phi)\Big\}, \end{aligned} \tag{5.30}$$

and the out-of-phase path can be shown to be

$$\begin{aligned} Q &= \frac{A}{4z}\Big\{ \frac{1}{i}\left[H(f_-)e^{2\pi i f_- t} - H(-f_-)e^{-2\pi i f_- t}\right]\cos(\phi) \\ &\quad +\left[H(f_-)e^{2\pi i f_- t} + H(-f_-)e^{-2\pi i f_- t}\right]\sin(\phi)\Big\}. \end{aligned} \tag{5.31}$$

Finally, squaring and adding Eqs. (5.30) and (5.31) to find the output of the spectrum analyzer gives

$$I^2 + Q^2 = \frac{A^2}{4z^2}\left|H(f_-)\right|^2. \tag{5.32}$$

For the output of the spectrum analyzer to be the variance of the deterministic input signal, the LO frequency must be at the same as the input frequency such that $f_- = 0$. At this LO frequency, the output is maximum and equal to

$$I^2 + Q^2 = \frac{A^2}{2}k, \tag{5.33}$$

where the scaling term is given by

$$k = \frac{\left|H(0)\right|^2}{2z^2}. \tag{5.34}$$

This scaling is taken into account to obtain the variance from the output of the spectrum analyzer when looking at the intensity measurement noise of a coherent state.

Coherent state power fluctuations

For calculating the coherent state power fluctuations, we will use the continuous wave notation where $\hat{a}$ is now time dependent. In this notation, $|\alpha|^2$ for the coherent state is the mean photon flux instead of the mean photon number. Furthermore, to get the variance of the measurement, we only need to look at the fluctuations of the operators[44],

$$\delta\hat{a} = \hat{a} - \langle\hat{a}\rangle = \hat{a} - \alpha, \tag{5.35}$$

where $\delta\hat{a}$ represents the fluctuations of the operator around the mean value. We will also assume α to be real. Using this notation, the power of the fluctuations, $\delta\hat{P}$, of the state are[44]

$$\delta\hat{P} = \alpha\left(\delta\hat{a}(t) + \delta\hat{a}^\dagger(t)\right) = \alpha\int_{-\infty}^{\infty}\left(\delta\hat{a}(f) + \delta\hat{a}(-f)^\dagger\right)e^{2\pi i f t}df, \tag{5.36}$$

where we are assuming the fluctuations are small compared to the mean value, such that terms of the order $\mathcal{O}(\delta\hat{a}^2)$ can be neglected. The noise power from the photodetector after measuring the state is $g\delta P$ where g is from the electronic gain of the detector. Since the RBW is significantly smaller that the bandwidth of the detector, the detector gain can be taken as constant over the frequency range of the RBW.

After detection of the state, it is sent into the spectrum analyzer. Similar to the deterministic signal, the input is split into the in-phase and out-of-phase paths. After mixing with the in-phase LO, the in-phase path is

$$I = \frac{\alpha g}{2iz}\int_{-\infty}^{\infty} df\left[\left(\delta\hat{a}(f_-) + \delta\hat{a}(-f_-)^\dagger\right)e^{2\pi i f_+ t} - \left(\delta\hat{a}(f_+) + \delta\hat{a}(-f_+)^\dagger\right)e^{2\pi i f_- t}\right], \tag{5.37}$$

and the out-of-phase path is

$$Q = \frac{\alpha g}{2z}\int_{-\infty}^{\infty} df\left[\left(\delta\hat{a}(f_-) + \delta\hat{a}(-f_-)^\dagger\right)e^{2\pi i f_+ t} + \left(\delta\hat{a}(f_+) + \delta\hat{a}(-f_+)^\dagger\right)e^{2\pi i f_- t}\right]. \tag{5.38}$$

To make dealing with the fluctuation terms easier, we deviate from the steps of the deterministic signal calculations, and next apply the RBW filter and square the in-phase and out-of-phase paths. Afterwards, we will take the expectation values of both paths and add them together. Starting with the in-phase path, the RBW filtering and squaring gives

$$\begin{aligned} I^2 \;=\; -\frac{\alpha^2 g^2}{4z^2}\int_{-\infty}^{\infty} df\int_{-\infty}^{\infty} d\omega H(\omega)H(f-\omega)\big[&\left(\delta\hat{a}(\omega - f_L) + \delta\hat{a}(-\omega + f_L)^\dagger\right)e^{2\pi i(\omega - f_L)t} \\ &- \left(\delta\hat{a}(\omega + f_L) + \delta\hat{a}(-\omega - f_L)^\dagger\right)e^{2\pi i(\omega + f_L)t}\big] \\ \times\big[&\left(\delta\hat{a}(f - \omega - f_L) + \delta\hat{a}(-f + \omega + f_L)^\dagger\right)e^{2\pi i(f - \omega - f_L)t} \\ &- \left(\delta\hat{a}(f - \omega + f_L) + \delta\hat{a}(-f + \omega - f_L)^\dagger\right)e^{2\pi i(f - \omega + f_L)t}\big], \end{aligned} \tag{5.39}$$

where ω is also a linear frequency and is used for integration. The expectation value of $\left\langle\delta\hat{a}(f)\delta\hat{a}(f')^\dagger\right\rangle = \delta(f - f')$, assuming $\mathcal{O}(\delta\hat{a}^2)$ can be neglected[44]. Using this relation, the expectation value of I^2 is

$$\left\langle I^2\right\rangle = -\frac{\alpha^2 g^2}{4z^2}\int_{-\infty}^{\infty} df H(f)\left[H(2f_L - f) - 2H(-f) + H(-2f_L - f)\right]. \tag{5.40}$$

For the out-of-phase term

$$\left\langle Q^2\right\rangle = \frac{\alpha^2 g^2}{4z^2}\int_{-\infty}^{\infty} df H(f)\left[H(2f_L - f) + 2H(-f) + H(-2f_L - f)\right]. \tag{5.41}$$

Adding the two paths together gives the output of the spectrum analyzer,

$$\left\langle I^2 + Q^2\right\rangle = \frac{\alpha^2 g^2}{z^2}\int_{-\infty}^{\infty} df\left|H(f)\right|^2. \tag{5.42}$$

Finally, dividing by k, Eq. (5.34), gives the variance of the detected coherent state input signal

$$\left\langle \Delta^2 \text{Input} \right\rangle = 2\alpha^2 g^2 \frac{\int_{-\infty}^{\infty} df\, |H(f)|^2}{|H(0)|^2}. \tag{5.43}$$

The splitting term from the initial splitting of the input is canceled out in this last step. How the input is split, either by power, $z = \sqrt{2}$, or voltage, $z = 2$, does not affect the variance of the input nor the number of photons used in the measurement.

Effective measurement time from error propagation of coherent state detection

The variance of the intensity detection in Eq. (5.43) can be error propagated into the photon number variance of the coherent state. To get the correct variance, the effective timing of the measurement will need to be set. Using $\langle \text{Input} \rangle = g\alpha^2 = g\frac{\langle \hat{n} \rangle}{t_e}$, where $\langle \hat{n} \rangle$ is the average number of photons detected in the effective detection time t_e, the photon number variance is

$$\begin{aligned} \left\langle \Delta^2 \hat{n} \right\rangle &= \frac{\left\langle \Delta^2 \text{Input} \right\rangle}{\left| \frac{\partial \langle \text{Input} \rangle}{\partial \langle \hat{n} \rangle} \right|^2} && (5.44) \\ &= 2 \langle \hat{n} \rangle t_e \frac{\int_{-\infty}^{\infty} df\, |H(f)|^2}{|H(0)|^2} && (5.45) \\ &= \langle \hat{n} \rangle , && (5.46) \end{aligned}$$

where the last equation comes from the photon number statistics of a coherent state. Setting Eq. (5.45) equal to Eq. (5.46) and solving for the effective time gives

$$t_e = \frac{|H(0)|^2}{2\int_{-\infty}^{\infty} df\, |H(f)|^2}. \tag{5.47}$$

For the spectrum analyzer used in the experiment, the RBW is the full-width at half-max of an approximate Gaussian filter. This response is for $|H(f)|^2$, not the actual low pass filter response. For a Gaussian RBW

$$\frac{|H(f)|^2}{|H(0)|^2} = e^{-\frac{4\ln(2) f^2}{\text{RBW}^2}} \tag{5.48}$$

and the effective time is

$$t_{\text{Gauss}} = \sqrt{\frac{\ln(2)}{\pi}} \frac{1}{\text{RBW}} \approx \frac{0.47}{\text{RBW}}. \tag{5.49}$$

Due to the RBW filter not being a perfect Gaussian [60], a correction factor of of ≈ 0.94 needs to be applied to the effective time such that for our system

$$t_e \approx \frac{0.44}{\text{RBW}}. \tag{5.50}$$

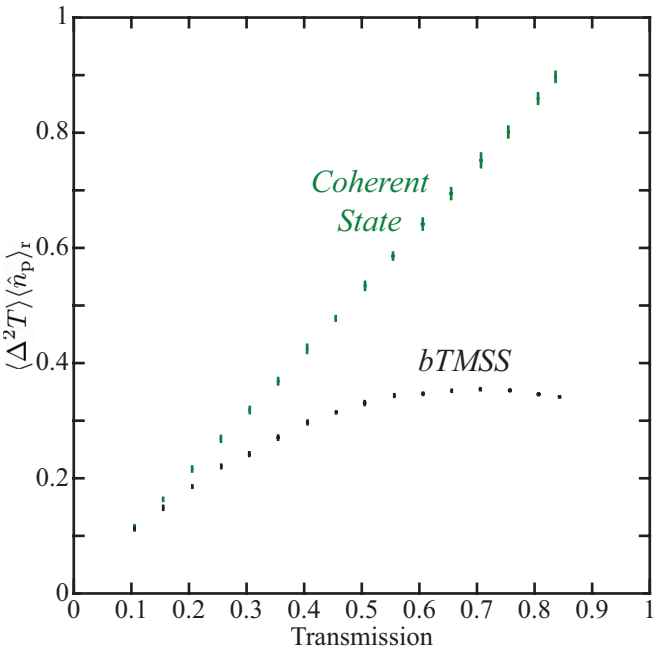


Figure 5.10: Results of the bTMSS transmission estimation uncertainty experiment. The transmission uncertainty is scaled by the number of photons used to probe the system. The black points are the bTMSS measurement results with one standard deviation horizontal error bars for the mean transmission and vertical error bars for the transmission uncertainty. Similarly, the green points are for the coherent state with error bars in the mean transmission and the uncertainty in the transmission estimation.

For our experiment, the RBW is 51 kHz and the effective time for the transmission estimation is 8.63 μs for a total of $\sim 10^9$ probe photons probing the system under study. As shown in Fig 5.10, this information allows us to rescale the transmission uncertainty from the experiment by the number of photons probing the system.

5.3.3 State characterization for determining the QCRB

For the actual bTMSS generated for our experiment, the previous approximation, see Sect. 4.3, of perfect state generation followed by loss does not hold in our case. Since the squeezing and beam splitter operators do not commute, the theory has to be expanded upon to include a absorptive generation, were there the state suffers loss during generation, of the bTMSS. A way to approximate the absorptive state generation is to distribute the loss throughout the generation process by splitting up the two mode squeezer into a series of smaller squeezers and apply a beam splitter operation in between each squeezer as shown in Fig. 5.11. The operations for the squeezing and loss operations can be broken up using [51,64]

$$\hat{S}_{p,c}(\xi) = \prod_{n=1}^{N} \hat{S}_{p,c}(\xi/N), \tag{5.51}$$

$$\hat{B}_p(T_x) = \prod_{n=1}^{N} \hat{B}_p(\sqrt[N]{T_x}), \tag{5.52}$$

$$\hat{B}_c(T_y) = \prod_{n=1}^{N} \hat{B}_c(\sqrt[N]{T_y}), \tag{5.53}$$



Figure 5.11: Model for squeezing generated in an absorptive medium. The squeezing operator is broken up into an infinite number of infinitesimal parts composed of a stage of loss in the probe from beam splitters after each stage of squeezing.

where T_x and T_y are the transmissions of the probe and conjugate mode, respectively. The total operation for the distributed loss during state generation is

$$\hat{S}_{p,c}(\xi; T_x, T_y|N) = \prod_{n=1}^{N} \hat{B}_c(\sqrt[N]{T_y})\hat{B}_p(\sqrt[N]{T_x})\hat{S}_{p,c}(\xi/N). \tag{5.54}$$

In the limit of $N \to \infty$, this was shown to be an accurate model for the absorptive generation of a bTMSS seeded with a coherent state[51]. The covariance matrix and displacement vector can be solved analytically following the work done by Jasperse *et. al*[64]. Working in the Heisenberg picture, the photon annihilation operators for the probe and conjugate modes transform as

$$\begin{aligned}
\hat{S}^\dagger_{p,c}(s)\hat{a}_p\hat{S}_{p,c}(s) &= \hat{a}_p\cosh(s) + \hat{a}^\dagger_c\sinh(s), && (5.55)\\
\hat{S}^\dagger_{p,c}(s)\hat{a}_c\hat{S}_{p,c}(s) &= \hat{a}_c\cosh(s) + \hat{a}^\dagger_p\sinh(s), && (5.56)\\
\hat{B}^\dagger_p(T_x)\hat{a}_p\hat{B}_p(T_x) &= \sqrt{T_x}\hat{a}_p + \sqrt{1-T_x}\hat{a}_x, && (5.57)\\
\hat{B}^\dagger_c(T_y)\hat{a}_c\hat{B}_c(T_y) &= \sqrt{T_y}\hat{a}_c + \sqrt{1-T_y}\hat{a}_y, && (5.58)\\
& && (5.59)
\end{aligned}$$

where the squeezing angle is set to decrease the variance of the amplitude difference quadrature, T_x and T_y are the transmissions for the probe and conjugate, respectively, and the operators $\hat{a}_x$ and $\hat{a}_y$ are vacuum mode operators. The operators at the $n+1$ step can be written as

$$\begin{aligned}
\hat{a}^{(n+1)}_p &= \sqrt{T_x}\left[\hat{a}^{(n)}_p\cosh(s) + \hat{a}^{\dagger(n)}_c\sinh(s)\right] + \sqrt{1-\sqrt[N]{T_x}}\hat{a}^{(n+1)}_x && (5.60)\\
\hat{a}^{\dagger(n+1)}_c &= \sqrt{T_y}\left[\hat{a}^{(n)}_p\sinh(s) + \hat{a}^{\dagger(n)}_c\cosh(s)\right] + \sqrt{1-\sqrt[N]{T_y}}\hat{a}^{(n+1)\dagger}_y. && (5.61)
\end{aligned}$$

Recursively applying each step, the final Nth step operators can be expressed as a matrix transform of the form

$$\begin{pmatrix}\hat{a}^{(N)}_p\\ \hat{a}^{\dagger(N)}_c\end{pmatrix} = \mathbf{A}^N\begin{pmatrix}\hat{a}^{(0)}_p\\ \hat{a}^{\dagger(0)}_c\end{pmatrix} + \sum_{n=1}^{N}\mathbf{A}^{N-n}\begin{pmatrix}\sqrt{1-\sqrt[N]{T_x}}\hat{a}^{(n)}_x\\ \sqrt{1-\sqrt[N]{T_y}}\hat{a}^{(n)\dagger}_y\end{pmatrix}, \tag{5.62}$$

where

$$\mathbf{A} = \begin{pmatrix}\sqrt[N]{T_x}\cosh(s/N) & \sqrt[N]{T_x}\sinh(s/N)\\ \sqrt[N]{T_y}\sinh(s/N) & \sqrt[N]{T_y}\cosh(s/N)\end{pmatrix}. \tag{5.63}$$

It can be seen from Eq. (5.62) that as the state is generated through each step, the field strength of the EM wave is both decreased by the transmissions of each mode through the beam splitters and increased by the squeezers and the correlation between the two modes changes in the same way. The part of the field lost to the environment changes as the steps increase and some of the generated photons from previously applied squeezing operations are lost. As shown in Appendix A, the final operators can be solved for and a density matrix and displace vector can be found for a bTMSS with imperfect generation.

QCRB for the imperfect generation of the bTMSS

For only displacing the probe mode and having no absorption of the conjugate mode, we have calculated the QCRB using the Gaussian form of the QFI[23],

$$\left\langle \Delta^2 T \right\rangle^{(\text{Lossy bTMSS})} \geq \frac{T}{\eta_p \left\langle \hat{n}_p \right\rangle_r} - \frac{T^2}{\left\langle \hat{n}_p \right\rangle_r} T_p H_c' \frac{32 s^2 \sqrt{T_x} \sinh^2\left(\frac{\zeta}{4}\right)}{\zeta^2 \left(\sqrt{T_x} - 1\right) + \Gamma}, \tag{5.64}$$

where $\zeta = \sqrt{16 s^2 + \ln^2\left(T_x\right)}$,

$$\Gamma = \sqrt{T_x} \left\{ \cosh\left(\frac{\zeta}{2}\right) \left[\zeta^2 + \ln^2\left(T_x\right)\right] - \ln\left(T_x\right) \left[\ln\left(T_x\right) + 2\zeta \sinh\left(\frac{\zeta}{2}\right)\right] \right\}, \tag{5.65}$$

and

$$H_c' = \frac{2\eta_c - 1}{\eta_c} \left(1 + \frac{\zeta^2 \left(\eta_c - 1\right)}{\zeta^2 \left[1 + \eta_c \left(\sqrt{T_x} - 2\right)\right] + \eta_c \Gamma} \right). \tag{5.66}$$

The conjugate loss term, H_c', has the same relation with η_c as H_c in Eq. (4.44), such that the term is positive for $\eta_c > 0.5$ and negative for $\eta_c < 0.5$ and $H_c' = 1$ when $\eta_c = 1$. The linear term of the QCRB in Eq. (5.64) is the same as the other bounds given in Eqs. (4.40)-(4.43), as it is the quadratic term that contains the quantum advantage. Though the $(\sqrt{T_x} - 1)$ part in the denominator may suggest otherwise, the quadratic term does not change sign as $T_x \to 0$ due to the larger positive Γ. As before, the probe losses make the bound tend towards that of a coherent state,

$$\frac{\left\langle \Delta^2 T \right\rangle^{(\text{lossy bTMSS})}}{\left\langle \Delta^2 T \right\rangle^{(\text{coh})}} \xrightarrow[T_x \to 0]{} 1, \tag{5.67}$$

as less probe transmission through the squeezing medium would have the mode tend towards a coherent state, not a thermal state. Unlike with propagation and detection loss, see Eqs. (4.45) and (4.46), the quantum advantage does not decrease linearly with state generation loss.

State fitting

Different amounts of squeezing and different propagation and detection losses have different QCRBs. To set the QCRB, Eq. (5.64), for our experiment, the state and subsequent losses

must be characterized. The bTMSS generated in the experiment can be characterized using the predicted balanced intensity difference variance and single beam intensity variances from the theoretical values and comparing them to the actual measured values. As shown in Appendix A, the variances normalized by a coherent state of equal power are

$$\frac{\langle\Delta^2\left(\hat{n}_p-\hat{n}_c\right)\rangle_0}{\langle\hat{n}_p\rangle_0+\langle\hat{n}_c\rangle_0} = 1-\frac{2s\sinh^2(\frac{\zeta}{4})}{\zeta\cosh(\frac{\zeta}{2}+\varsigma)}-\sqrt{T_x}\frac{s\ln^2(T_x)\sinh^4(\frac{\zeta}{4})}{2\zeta^3\cosh(\frac{\zeta}{2}+\varsigma)}, \tag{5.68}$$

$$\frac{\langle\Delta^2\hat{n}_p\rangle_0}{\langle\hat{n}_p\rangle_0} = \frac{16s^2\left\{1-\sqrt{T_x}\left[1-\cosh(\frac{\zeta}{2})\right]\right\}+\ln^2(T_x)}{\zeta^2}, \tag{5.69}$$

$$\frac{\langle\Delta^2\hat{n}_c\rangle_0}{\langle\hat{n}_c\rangle_0} = \frac{2\sqrt{T_x}\left[8s^2+(\zeta^2-8s^2)\cosh(\frac{\zeta}{2})-\zeta\ln(T_x)\sinh(\frac{\zeta}{2})\right]-\zeta^2}{\zeta^2}, \tag{5.70}$$

where $\tanh(\varsigma)=\frac{\ln(T_x)}{\zeta}$. These are for the generated, not the measured, state and as such do not include the propagation and detection loss terms. For the individual mode intensity variances, the variances of the generated beams can be backtracked from the measured variance using

$$\left\langle\Delta^2\hat{n}\right\rangle_m = \eta^2\left\langle\Delta^2\hat{n}\right\rangle_0+\eta(1-\eta)\left\langle\hat{n}\right\rangle_0, \tag{5.71}$$

$$\left\langle\hat{n}\right\rangle_m = \eta\left\langle\hat{n}\right\rangle_0 \tag{5.72}$$

such that

$$\frac{\langle\Delta^2\hat{n}\rangle_0}{\langle\hat{n}\rangle_0}=\frac{\frac{\left\langle\Delta^2\hat{n}\right\rangle_m}{\left\langle\hat{n}\right\rangle_m}-(1-\eta)}{\eta}, \tag{5.73}$$

where η is the total transmission of the mode and the subscript m indicates the measured value. For the probe mode, $\eta=T_p\eta_p$ and $\eta=\eta_c$ for the conjugate mode.

Thus to characterize the state, the propagation and detection transmissions of the probe and conjugate mode must first be calibrated. To measure the transmissions, two power meters are set up. One power meter, PM1, is mounted before the Rb vapor cell on a flip mount and a second power meter, PM2, is moved around to measure different transmissions. To begin, the vapor cell is moved out of the beam path and PM2 is set directly behind PM1 to calibrate the difference in power readings between the two power meters. Next, PM2 is moved to before the system under study to measure the common path of both the probe and conjugate modes after the cell and is found to be $T_{\text{common}}=98.4\%\pm1\%$. Afterwards, the Rb vapor cell is put back and, with the probe far off any Rb resonance, the transmission of the cell windows is calculated. Each cell window is found to have a transmission of $T_{\text{window}}=98.8\%\pm1\%$. Only the output window of the cell is part of the probe propagation transmission and thus $T_p=T_{\text{common}}T_{\text{window}}=97.3\%\pm1\%$. The detection efficiency of the photodiodes is approximated from previous work with the same model of photodiodes which had a quantum efficiency of $\eta_p=94.5\%\pm2\%$[51]. The detection efficiency of the conjugate mode for our setup is the same as the total transmission of the probe mode, $\eta_c=T_p\eta_p=91.9\%\pm2\%$. Thus for both modes $\eta=91.9\%$. The intensity difference variance

from the generated state can also be backtracked from the measured state using

$$\begin{aligned}\left\langle \Delta^2(\hat{n}_p - \hat{n}_c)\right\rangle_m &= \eta^2\left\langle \Delta^2\hat{n}_p\right\rangle_0 + \eta(1-\eta)\left\langle \hat{n}_p\right\rangle_0 + \eta^2\left\langle \Delta^2\hat{n}_p\right\rangle_0 + \eta(1-\eta)\left\langle \hat{n}_p\right\rangle_0 \\ &\quad -2\eta^2\left(\left\langle \hat{n}_p\hat{n}_c\right\rangle_0 - \left\langle \hat{n}_p\right\rangle_0\left\langle \hat{n}_c\right\rangle_0\right) \qquad (5.74)\\ &= \eta^2\left\langle \Delta^2(\hat{n}_p - \hat{n}_c)\right\rangle_0 + \eta(1-\eta)\left(\left\langle \hat{n}_p\right\rangle_0 + \left\langle \hat{n}_c\right\rangle_0\right) \qquad (5.75)\end{aligned}$$

such that

$$\frac{\left\langle \Delta^2(\hat{n}_p - \hat{n}_c)\right\rangle_0}{\left\langle \hat{n}_p\right\rangle_0 + \left\langle \hat{n}_c\right\rangle_0} = \frac{\frac{\left\langle \Delta^2(\hat{n}_p - \hat{n}_c)\right\rangle_m}{\left\langle \hat{n}_p\right\rangle_m + \left\langle \hat{n}_c\right\rangle_m} - (1-\eta)}{\eta}, \qquad (5.76)$$

since the transmission of both modes is the same

With the generated state noises measured, the bTMSS used in the experiment can be characterized. To find the parameters for the generated state, the squeezing s and internal probe transmission T_x, the variance of the probe, conjugate, and balanced intensity difference measurements are compared to the theory for the variances, Eqs. (5.68)-(5.70). The goodness-of-fit, GoF, parameter for the fitting is[65]

$$\mathrm{GoF}(s, T_x) = \sum_i \frac{\left[\mathrm{Measurement}_i - \mathrm{Theory}_i(s, T_x)\right]^2}{\mathrm{Uncertainty\ of\ Measurement}_i}, \qquad (5.77)$$

where the sum is over each normalized measurement indexed by i. The values of s and T_x that minimized GoF minimize the difference between the measurements and the theoretical predictions. As explained in Appendix B, the parameter values are considered a good fit when the GoF ≤ 1.

The GoF minimization process involves a type of genetic algorithm, called differential evolution[66,67], to explore the parameter space of all possible s and T_x values to find the global minimum for the GoF. For the minimization, a collection of random values for the parameters are generated and then mixed based on the GoF for those parameter values. This process allows the algorithm to search the parameter space of the GoF and find the global minimum. The algorithm is explained in detail in Appendix B. The parameter values that best match the theory to the measurements are $s = 2.04 \pm 0.02$ and $T_x = 71\% \pm 2\%$ with a GoF$= 0.4563$.

These parameters are not used as part of the transmission estimation from the measurement, only for setting the QCRB for our state. To also keep the QCRB independent of the probing power, the bound is rescaled by the number of probing photons when comparing the experiment results to the bound. This keeps the photon number a property of the measurement and thus the fundamental bound for the measurement only uses the parameters from this section: T_p, η_p, η_c, T_x and s. Therefore the bound calculations and experiment analysis are completely independent of each other and the bound cannot be adjusted to better match the experimental results as there are no free parameters in setting the QCRB for our state.

5.4 Final results

The final results[23] are shown in Fig. 5.12. The solid orange line is the QCRB for the bTMSS generated for the experiment. The calculation of the bound is done using measurements not part of the uncertainty measurements. These measurements are of the individual probe and conjugate intensity variance and the balanced intensity difference variance of the two modes and they are used to find and characterize the state parameters. These measurements are only used to find the bound for our state and do not contribute to the transmission uncertainty calculations. The gray region is the one standard deviation error in the QCRB due to the uncertainty in the calibration of the parameters of the bound; s, T_x, T_p, η_p, and η_c. In black is the measured transmission uncertainty scaled by the number of probing photons with 1 standard deviation horizontal error bars in the mean transmission and vertical error bars for the transmission uncertainty. The number of photons is recorded for every transmission measurement, as is the uncertainty in the transmission estimation. The data points are well within the uncertainty range for the theoretical QCRB, indicating that the optimized intensity difference measurement does saturate the bound. Because of the tight control of the state and system are we able to build these statistics and because of the calibrations of the measurement and system can we compare our results to the theory and show saturation of the bound.

Also shown in blue in Fig. 5.12 is the ultimate limit for transmission estimation. While our state does not reach this limit, even when taking into account losses in the probe mode, our state is close. With improved technology to increase squeezing and reduce absorption during state generation, the gap between our state and the ultimate bound will be reduced.

These results not only show that the optimized intensity difference measurement saturates the QCRB for transmission estimation, but also that the bound can be saturated with currently available technology. The estimation variance is dominated by quantum statistics and not fluctuations from the measurement or laser system. With the transmission estimation uncertainty set by the state probing the system under study, further enhancement of the measurement cannot be done by designing better measurements and must be done by improving the generation of quantum states.

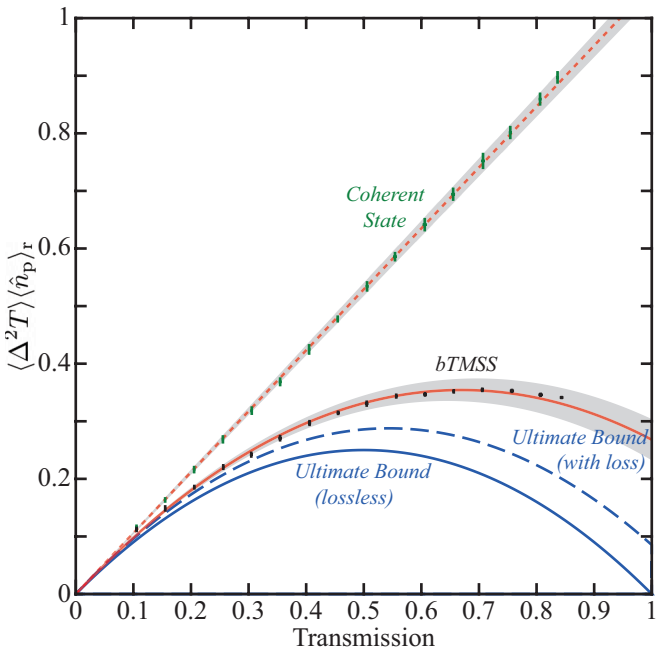


Figure 5.12: Results of the bTMSS transmission estimation uncertainty experiment. The orange lines show the QCRB for the bTMSS (solid) and coherent state (dashed) and the gray regions are the one standard deviation errors in the theoretical bounds. The transmission uncertainty is scaled by the number of photons used to probe the system. The black points are the bTMSS measurement results with one standard deviation horizontal error bars for the mean transmission and vertical error bars for the transmission uncertainty. Similarly, the green points are for the coherent state with error bars in the mean transmission and the uncertainty in the transmission estimation. Also plotted in blue is the ultimate limit (solid) and the ultimate limit with the same propagation and detection losses as the probe mode (dashed). The lossy ultimate limit is assumed to be the same as the Fock state QCRB.

Chapter 6

Resonance Sensors: Comparison of Sensitivity Limits Based on Phase and Transmission Measurements

In the previous chapters, the phase of the system model is ignored as it had no effect on the transmission estimation. In this chapter, we will expand the system model to include the phase change, *i.e.* dispersion, introduced by the system under study as the probe mode is transmitted, allowing for two different parameters to be estimated in order to sense a change in the system. Intrinsically, there is a link between transmission and phase changes for a system as, due to causality, a system is not able to respond to any driving force, *i.e.* an EM field, instantaneously. To do so would involve reacting to the driving force before being affected by it. Since the system cannot respond instantaneously, the delayed response time causes a phase delay between the input and output EM fields. Thus, for a system with a transmission dependent on the optical frequency, there must exist a frequency dependent phase change as well. The frequency dependent transmission and phase are set by the complex system transfer function, $\tau(f)$, such that transmission $T = |\tau|^2$ and phase $\phi = \arg(\tau)$.

There exists a common type of sensor, the resonance sensor, that has a frequency dependent transmission and phase responses such as those shown in Fig. 6.1(a). These devices have a transfer function with a relatively large change in magnitude centered around a resonance frequency. When the resonance frequency shifts, so does the transmission and phase response of the system. The plasmonic sensor[68,69] mentioned previously falls into this category as do optical cavities[70], whispering-gallery mode resonators[71,72], and photonic crystals[73] all of which have a resonance frequency shift caused by changes in temperature, stress or strain, or local refractive index. When probing the sensor with light at a given frequency, a change in the resonance frequency can be sensed using either the change in transmission or phase. Thus, a comparison of phase and transmission measurements can be done using frequency estimation as it is not a simple question as to which parameter, transmission or phase, gives

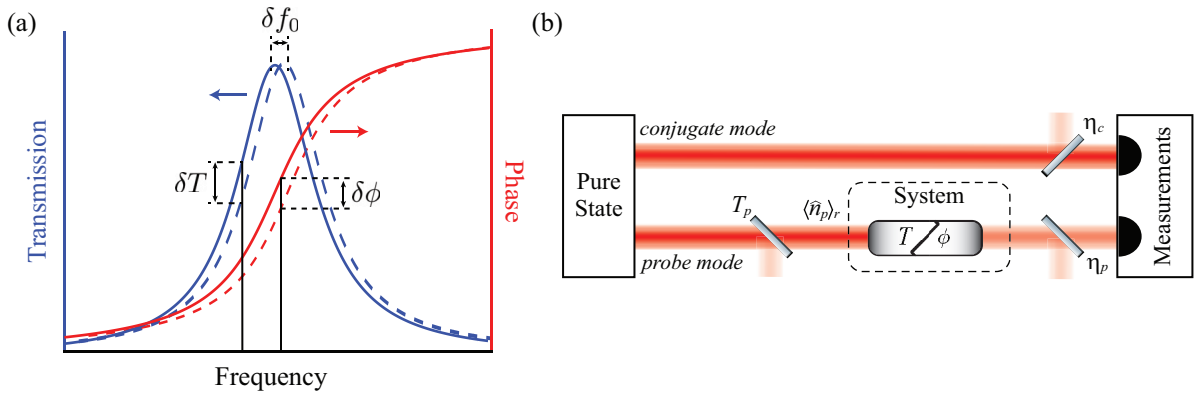


Figure 6.1: Response of a resonance sensor. (a) The transmission and phase for a Lorentzian lineshape transfer function. A resonance frequency shift causes the transmission and phase to change. Thus, a measurement of the transmission or phase can be used to estimate the change in frequency. (b) Setup for probing the resonance sensor. As before, the bTMSS is generated, suffers loss before and after the system on the probe mode and losses on the conjugate mode, and the transmission or phase of the state is measured to estimate the change in frequency. © IOP Publishing. Reproduced with permission. All rights reserved [75].

a better estimation of the shift in resonance frequency since it is dependent on the form of the transfer function. For clarity, the frequency shift, as the parameter of interest, will be "estimated" through the transmission or phase, which will be considered "measured". So we will be doing phase or transmission measurements to estimate the frequency shift.

It has been shown that the bTMSS, in addition to transmission measurements, can also be used to measure phase with a quantum enhancement over a classical state. The uncertainty in the measurement of phase has a known QCRB for the lossless case given by [74]

$$\left\langle \Delta^2\phi \right\rangle^{(\mathrm{bTMSS})} \geq \frac{\operatorname{sech}(2s)}{4\left\langle \hat{n}_p \right\rangle_r}. \tag{6.1}$$

Thus, the comparison between phase and transmission measurements will be done as fair as possible. That is, using the same state, probe power, and QCRB saturating measurement, as it will be shown below that a quadrature measurement, the optimized homodyne detection, can saturate both the transmission and phase QCRB.

Figure 6.1(b) shows the setup for the resonance sensor parameter estimation, which is similar to the setup for transmission estimation except the system of interest changes the phase and transmission of the incident light. For simplicity, let us first assume the resonance sensor has a Lorentzian lineshape, as shown in Fig. 6.1(a), such that the system response has a transfer function of the form

$$\tau(f) = \frac{1}{1 - i\left(\frac{f-f_0}{\Delta_f}\right)}, \tag{6.2}$$

where f_0 is the resonance frequency and Δ_f is the half-width at half-max (HWHM).

The real and imaginary parts of the transfer function are Hilbert transforms of each other, also known as the Kramers-Kronig relations[76,77], which arise from causality for a system responding to a driving force.

The Lorentzian transfer function has a transmission and phase response of the form

$$T(f) = \frac{1}{1+\left(\frac{f-f_0}{\Delta_f}\right)^2} = |\tau(f)|^2 \tag{6.3}$$

$$\phi(f) = \arctan\left(\frac{f-f_0}{\Delta_f}\right) = \arg\big(\tau(f)\big), \tag{6.4}$$

respectively. Shifting either the probing frequency, f, or the resonance frequency, f_0, leads to the same change in magnitude for either the transmission or phase of the system, governed by the HWHM. We define a unitless parameter $F = \frac{f-f_0}{\Delta_f}$ to make the analysis independent of the resonance frequency or HWHM of a particular resonance sensor. This also allows for our analysis to include resonance sensor where the HWHM changes instead of, or in addition to, the resonance frequency. The variance in either parameter can be recovered from the unitless parameter via[37]

$$\left\langle \Delta^2 f_0 \right\rangle = \Delta_f^2 \left\langle \Delta^2 F \right\rangle \tag{6.5}$$

$$\left\langle \Delta^2 \Delta_f \right\rangle = \frac{\Delta_f^2}{F^2} \left\langle \Delta^2 F \right\rangle. \tag{6.6}$$

The resonance frequency uncertainty is just a rescaling by the HWHM from the unitless frequency uncertainty but a resonance sensor with a changing HWHM is different. On resonance a change in HWHM is undetectable, as neither the resonant phase nor transmission changes with HWHM. Hence, the $1/F^2$ term in the variance conversion. For this chapter, the discussions will typically assume a shift of the resonance frequency, but will mention HWHM changes the when significant. It should be noted that near resonance, sensitivities will be much lower for HWHM estimation , while they will be much higher far off resonance.

The sensitivity for changes in F using transmission or phase measurements is defined as

$$S(F|X) = \left[\left(\frac{\partial X}{\partial F}\right)^{-2} \left\langle \Delta^2 X \right\rangle\right]^{-1}, \tag{6.7}$$

where X is either transmission or phase. Here we will assume that the measurements in transmission or phase are performed at the QCRB. As such, Eq. 6.7 is the fundamental limit to the sensitivity in estimating F using either transmission or phase measurements. It should be noted that the sensitivity used here is not the same as the QFI for the estimation of F, as Birchall *et. al*[78] have shown it to be equal to the sum of the phase and transmission measurement sensitivities. However, since transmission is inherently a photon number type measurement, it does not commute with phase measurements. Thus, phase and transmission cannot be estimated at the QCRB simultaneously.

6.1 Lossy phase estimation with a bTMSS

The QCRB for phase estimation with a bTMSS is known only for the ideal lossless case, Eq. (6.1). It has also been shown that optimized homodyne detection saturates the lossless bound for phase estimation [74]. Here, we will expand on those previous works by deriving the lossy phase estimation QCRB for the bTMSS and show, as well as define, the optimized homodyne detection that saturates the lossy bound, for both phase and transmission estimation.

For the lossy phase system, we split the system into a beam splitter, as used in the previous chapters, and a phase rotation operator. The order of these operations does not matter in our case since the environment that the beam splitter couples to is traced out and the information lost, but in general the order would matter. The phase rotation operator $\hat{\Phi}_p(\phi) = e^{i\hat{n}_p\phi}$ changes the probe field as

$$\hat{\Phi}^\dagger(\phi)\hat{a}_p\hat{\Phi}(\phi) \to \hat{a}_p e^{i\phi}, \tag{6.8}$$

adding a phase rotation ϕ. This rotation changes the covariance matrix and displacement vector of the lossy bTMSS, see Eqs. (4.38) and (4.39), to

$$\boldsymbol{\sigma} = \begin{pmatrix} \mathcal{T}\cosh(2s)+1-\mathcal{T} & 0 & 0 & -\sqrt{\mathcal{T}\eta_c}e^{i(\theta+\phi)}\sinh(2s) \\ 0 & \eta_c\cosh(2s)+1-\eta_c & -\sqrt{\mathcal{T}\eta_c}e^{i(\theta+\phi)}\sinh(2s) & 0 \\ 0 & -\sqrt{\mathcal{T}\eta_c}e^{-i(\theta+\phi)}\sinh(2s) & \mathcal{T}\cosh(2s)+1-\mathcal{T} & 0 \\ -\sqrt{\mathcal{T}\eta_c}e^{-i(\theta+\phi)}\sinh(2s) & 0 & 0 & \eta_c\cosh(2s)+1-\eta_c \end{pmatrix}, \tag{6.9}$$

$$\vec{d} = \begin{pmatrix} \sqrt{\mathcal{T}}\left[\alpha\cosh(s) - \beta^* e^{i\theta}\sinh(s)\right]e^{i\phi} \\ \sqrt{\eta_c}\left[\beta\cosh(s) - \alpha^* e^{i\theta}\sinh(s)\right] \\ \sqrt{\mathcal{T}}\left[\alpha^*\cosh(s) - \beta e^{-i\theta}\sinh(s)\right]e^{i\phi} \\ \sqrt{\eta_c}\left[\beta^*\cosh(s) - \alpha e^{-i\theta}\sinh(s)\right] \end{pmatrix}, \tag{6.10}$$

where $\mathcal{T} = T_p T\eta_p$ and T is the transmission through the system. The phase rotation affects both the direction of the displacement of the probe mode, in $\vec{d}$, and the angle of asymmetry of the squeezed quadrature correlation, in $\boldsymbol{\sigma}$, see Ch. 2.

The same Gaussian form for the QFI when only the displaced terms, as in Eq. (4.19), which are dominant for the bTMSS, is used to find

$$F_Q(\phi) = 2\frac{\partial\vec{d}^\dagger}{\partial\phi}\boldsymbol{\sigma}^{-1}\frac{\partial\vec{d}}{\partial\phi}. \tag{6.11}$$

Using this, we derived the bTMSS lossy phase estimation QCRB to be [75]

$$\left\langle\Delta^2\phi\right\rangle^{(\text{bTMSS})} \geq \frac{1}{4T\eta_p\left\langle\hat{n}_p\right\rangle_r} - \frac{1}{4\left\langle\hat{n}_p\right\rangle_r}T_p H_c[1-\text{sech}(2s)] \tag{6.12}$$

where

$$H_c = \frac{(2\eta_c-1)\left[1+2\sinh^2(s)\right]}{1+2\eta_c\sinh^2(s)}. \tag{6.13}$$

This bound is very similar to the transmission bound, Eq. (4.41), differing only by a factor of $\frac{1}{4\mathcal{T}^2}$. Thus, similar to the transmission QCRB, the first term on the right hand side is the classical limit of the coherent state and the second term on the right hand side is the one that leads to the quantum advantage. This can be seen by setting $s = 0$ such that only the coherent state seed of the probe mode remains. As the squeezing, and thus the s parameter, increases, the quantum advantage term reduces the bound. As with the transmission bound, losses before the system in the probing mode increase the classical term while losses after decrease the quantum advantage. Losses in the conjugate mode will flip the quantum advantage into a disadvantage at $\eta_c < 0.5$, same as with transmission estimation.

With both the phase and transmission QCRB being closely related and the two measurements having very different ranges, 0 to 1 for transmission and 0 to 2π for phase, a parameter is needed to compare the two. The sensitivity to the frequency shift of the resonance sensors using either a phase or transmission measurement will provide such a comparison between the two approaches for sensing applications. Especially since, as will be shown below, both the transmission and phase QCRB for the bTMSS can be saturated by the same measurement, optimized homodyne detection.

6.1.1 Measurement to saturate phase bound

Optimized homodyne detection is a quadrature measurement, Eq. (2.7), that has been shown to saturate the QCRB for bTMSS phase estimation in the lossless case[74]. Similar to the optimized intensity difference, Eq. (4.62), this measurement has an electronic gain applied to the conjugate quadrature measurement to minimize the measurement noise, $\hat{Q}_p(\gamma_p) - g_{\text{opt}}\hat{Q}_c(\gamma_c)$, where $\gamma_{p(c)}$ selects the quadrature of the probe (conjugate). Here, we will show that this measurement also saturates the bound when there is imperfect transmission in propagating to the system, through the system, and after the system, as well as loss in the conjugate mode. The lossy measurement noise is given by

$$\begin{aligned}\left\langle \Delta^2\left[\hat{Q}_p(\gamma_p) - g\hat{Q}_c(\gamma_c)\right]\right\rangle &= \left\langle \Delta^2\hat{Q}_p(\gamma_p)\right\rangle + g^2\left\langle \Delta^2\hat{Q}_c(\gamma_c)\right\rangle \\ &\quad -2g\left[\left\langle \hat{Q}_p(\gamma_p)\hat{Q}_c(\gamma_c)\right\rangle \left\langle \hat{Q}_p(\gamma_p)\right\rangle \left\langle \hat{Q}_c(\gamma_c)\right\rangle\right] \qquad (6.14)\\ &= \mathcal{T}\cosh(2s) + 1 - \mathcal{T} \\ &\quad +g^2\left[\eta_c\cosh(2s) + 1 - \eta_c\right] \\ &\quad -2g\sqrt{\mathcal{T}\eta_c}\sinh(2s)\cos(\gamma_p + \gamma_c - \phi - \theta), \qquad (6.15)\end{aligned}$$

and optimizing the phase gives

$$\left\langle \Delta^2\left[\hat{Q}_p(\gamma_p) - g_{\text{opt}}\hat{Q}_c(\gamma_c)\right]\right\rangle = \mathcal{T}\cosh(2s) + 1 - \mathcal{T} - \frac{\mathcal{T}\eta_c\sinh^2(2s)\cos^2(\gamma_p + \gamma_c - \phi - \theta)}{\eta_c\cosh(2s) + 1 - \eta_c} \qquad (6.16)$$

where $g_{\text{opt}} = -\frac{\sqrt{\mathcal{T}\eta_c}\sinh(2s)\cos(\gamma_p+\gamma_c-\phi-\theta)}{\eta_c\cosh(2s)+1-\eta_c}$. While the measurement is denoted as a quadrature difference it should be noted that the sign of the optimal gain changes when $\gamma_p \to \gamma_p + \pi/2$

and $\gamma_c \to \gamma_c + \pi/2$. This is due to the two-mode squeezed state having reduced noise in the difference of one quadrature and the sum of the perpendicular quadrature, *i.e.* amplitude difference and phase sum. As such, we simplify the homodyne detection to only consider the same quadrature in both modes, setting $\gamma_p = \gamma_c \equiv \gamma$. The variance of the measurement is minimized when $\cos^2(2\gamma - \phi - \theta) = 1$ by setting $\gamma = (n\pi + \phi + \theta)/2$ where $n \in \mathbb{Z}$. Thus, the optimal quadrature measurement depends on the squeezing angle, θ, and the phase parameter of interest, ϕ.

Without loss of generality, the squeezing angle θ can be set to the sum of the probe seeding phase, χ, and conjugate seeding phase, ξ, $\theta = \chi + \xi$. This is due to the angle of the quadrature squeezing, compared to the angle of the displacement, being a sum of all three terms. Thus, the quadrature squeezing is controlled via the phase of the seeding modes. With the squeezing phase set this way, then γ with an even numbered n, γ_e, corresponds to the amplitude difference measurement and an odd numbered n, γ_o, corresponds to the phase sum measurement.

Using the mean value of the measured probe quadrature

$$\left\langle \hat{Q}_p(\gamma) \right\rangle = 2\sqrt{\mathcal{T}}\left[|\alpha|\cosh(s) + |\beta|\sinh(s)\right]\cos(\phi - \chi - \gamma) \tag{6.17}$$

it can be shown that when $\xi = \chi + \phi$

$$\begin{aligned}
\left\langle \Delta^2 \phi \right\rangle &= \frac{\left\langle \Delta^2 \left[\hat{Q}_p(\gamma_o) - g_{\text{opt}}\hat{Q}_c(\gamma_o)\right]\right\rangle}{\left|\frac{\partial\left\langle \hat{Q}_p(\gamma_o)\right\rangle}{\partial\phi}\right|^2} && (6.18)\\
&= \frac{\mathcal{T}\cosh(2s) + 1 - \mathcal{T} - \frac{\mathcal{T}\eta_c \sinh^2(2s)}{\eta_c\cosh(2s)+1-\eta_c}}{4\mathcal{T}[|\alpha|\cosh(s) + |\beta|\sinh(s)]^2} && (6.19)\\
&= \frac{1}{4T\eta_p\left\langle \hat{n}_p\right\rangle_r} - \frac{1}{4\left\langle \hat{n}_p\right\rangle_r} T_p H_c[1 - \text{sech}(2s)], && (6.20)
\end{aligned}$$

which saturates the phase QCRB[75]. The same measurement, but for the amplitude difference quadrature, γ_e, will saturate the transmission QCRB[75]

$$\begin{aligned}
\left\langle \Delta^2 T \right\rangle &= \frac{\left\langle \Delta^2 \left[\hat{Q}_p(\gamma_e) - g_{\text{opt}}\hat{Q}_c(\gamma_e)\right]\right\rangle}{\left|\frac{\partial\left\langle \hat{Q}_p(\gamma_e)\right\rangle}{\partial T}\right|^2} && (6.21)\\
&= \frac{\mathcal{T}\cosh(2s) + 1 - \mathcal{T} - \frac{\mathcal{T}\eta_c \sinh^2(2s)}{\eta_c\cosh(2s)+1-\eta_c}}{\frac{T_p\eta_p}{T}[|\alpha|\cosh(s) + |\beta|\sinh(s)]^2} && (6.22)\\
&= \frac{T}{\eta_p\left\langle \hat{n}_p\right\rangle_r} - \frac{T^2}{\left\langle \hat{n}_p\right\rangle_r} T_p H_c[1 - \text{sech}(2s)]. && (6.23)
\end{aligned}$$

When comparing the frequency sensitivity from measuring either transmission or phase, it will be assumed the measurement is being done via homodyne detection. Comparing

transmission or phase using either the QCRB or the same measurement to estimate frequency gives a fair comparison. While it may seem odd at first to require a measurement to be able to say that we have a fair comparison, Jarzyna *et. al.*[79] pointed out that there exist "hidden" resources in QCRB calculations and that finding a measurement that saturates the bound illuminates what these resources are. For homodyne detection the hidden resource is the local oscillator (LO) used as a phase reference to set γ, the phase of the quadrature[80]. This LO is used the same as an electronic LO is used in the previous chapter to demodulate a signal, see Eq. (5.17). Instead of a mixer to multiply the electronic LO with a signal, we use a beam splitter to mix the probe with an optical LO for $\hat{Q}_p$. Instead of zero phase difference for the electronic LO to measure the amplitude of the signal, we set the phase of the optical LO to γ_e to measure the amplitude quadrature. Being able to set a phase for the probe or conjugate mode implies a phase reference, the LO, and thus a LO is a "hidden" resource as it is not explicitly stated. With how we are counting resources, probe photons interacting with the system, these hidden resources are free and do not create an advantage for the optimized homodyne measurement when compared to the optimized intensity difference measurement that has no hidden resources. However, other applications may count resources differently and thus comparing transmission and phase with the same measurement that saturates both QCRB's for the same state, as only γ changes between phase and transmission saturation, gives the most equivalent comparison of the two parameters for frequency estimation.

6.2 Frequency estimation

As shown in Fig. 6.2, for a generalized resonance sensor response, the transmission is defined as

$$T(F) = T_{\text{off}} + (T_{\text{res}} - T_{\text{off}})T_0(F), \tag{6.24}$$

where T_{res} is the transmission at the resonance frequency, $F = 0$, T_{off} is the far-off resonance transmission, $|F| \gg 1$, and $T_0(F)$ defines the lineshape of the transmission response. A sensor with $T_{\text{res}} > T_{\text{off}}$, see Fig. 6.2(a), will be labeled as having a peak response as the transmission peaks at the resonance frequency and a sensor with $T_{\text{res}} < T_{\text{off}}$, see Fig. 6.2(b), will be labeled as having a dip response. For a resonance sensor, one of the most common lineshapes is Lorentzian,

$$T_0(F) = \left|\frac{1}{1 - iF}\right|^2 = \frac{1}{1 + F^2}. \tag{6.25}$$

Following the Kramer-Kronig relations as shown in Appendix C, the transmission and phase response for a generalized Lorentzian response are given by

$$T(F) = T_{\text{off}} + \frac{T_{\text{res}} - T_{\text{off}}}{1 + F^2} \tag{6.26}$$

$$\phi(F) = \arctan\left[\frac{F\left(\sqrt{T_{\text{res}}} - \sqrt{T_{\text{off}}}\right)}{F^2\sqrt{T_{\text{off}}} + \sqrt{T_{\text{res}}}}\right]. \tag{6.27}$$

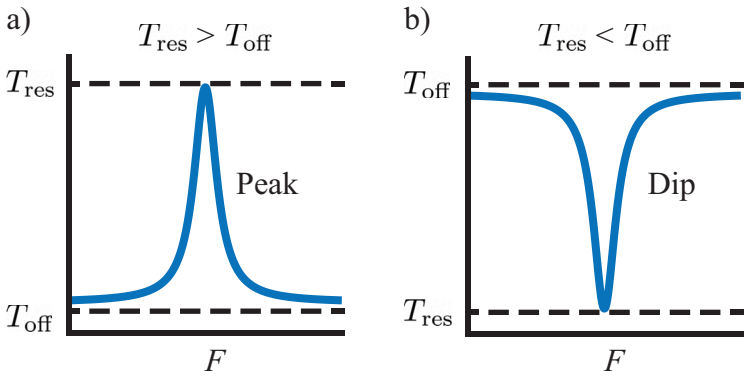


Figure 6.2: Plot of transmission versus frequency of the (a) peak resonance when $T_{\rm res} > T_{\rm off}$ and (b) dip resonance when $T_{\rm res} < T_{\rm off}$ for a Lorentzian line shape. By defining the on and far-off resonance transmission and lineshape we are able to create any arbitrary transmission response for the resonance system under study

Using Eq. (6.7), we find the sensitivity in estimating F using transmission or phase measurements to be[75]

$$S(F|T) = \langle \hat{n}_p \rangle_r \left\{ \frac{(1+F^2)^3 (F^2 T_{\rm off} + T_{\rm res})}{4F^2 \eta_p (T_{\rm off} - T_{\rm res})^2} - \frac{(1+F^2)^2 (F^2 T_{\rm off} + T_{\rm res})^2}{4F^2 (T_{\rm off} - T_{\rm res})^2} T_p H_c [1 - \mathrm{sech}(2s)] \right\}^{-1}, \tag{6.28}$$

$$S(F|\phi) = \langle \hat{n}_p \rangle_r \left\{ \frac{(1+F^2)^3 (F^2 T_{\rm off} + T_{\rm res})}{4\eta_p \left(\sqrt{T_{\rm off}} - \sqrt{T_{\rm res}}\right)^2 \left(F^2 \sqrt{T_{\rm off}} - \sqrt{T_{\rm res}}\right)^2} - \frac{(1+F^2)^2 (F^2 T_{\rm off} + T_{\rm res})^2}{4 \left(\sqrt{T_{\rm off}} - \sqrt{T_{\rm res}}\right)^2 \left(F^2 \sqrt{T_{\rm off}} - \sqrt{T_{\rm res}}\right)^2} T_p H_c [1 - \mathrm{sech}(2s)] \right\}^{-1}. \tag{6.29}$$

Just like for the transmission and phase estimation, the first term in the curly brackets is the classical limit and the second term is the quantum advantage obtained by using a bTMSS. Also, for both sensitivities, and due to how we wrote the terms, the numerators in the brackets are the same for the classical limit term and quantum advantage term. The difference in frequency sensitivity for transmission or phase measurements comes from the denominator. Figure 6.3 compares the sensitivity per probe photon incident with the system at different frequencies and transmissions for a peak and dip response. The plots are for the lossless case, $T_p = \eta_p = \eta_c = 1$, and with $s = 2$. In nearly every case, the optimal, *i.e.* maximum, phase sensitivity is higher than the optimal transmission sensitivity. Though transmission can be higher for a given frequency.

For transmission estimation, the uncertainty is minimized at transmission extremes of 1 or 0 at high levels of squeezing. However, the maximum frequency sensitivity using transmission does not occur at maximum transmission as the change in transmission is not the same at all frequencies. At resonance, the transmission response of the sensor has zero slope, $\left|\frac{\partial T}{\partial F}\right|$, while the maximum slope is at $F = \pm\frac{1}{\sqrt{3}} \approx \pm 0.577$. The maximum sensitivity is also not at the maximum slope either, as the sensitivity in frequency is a combination of the transmission uncertainty as well as the slope of the transmission response function. This is shown for the $T_{\rm res} = 1$ peak resonance in Table 6.1. The plot of Fig. 6.3(e) is an exception for the

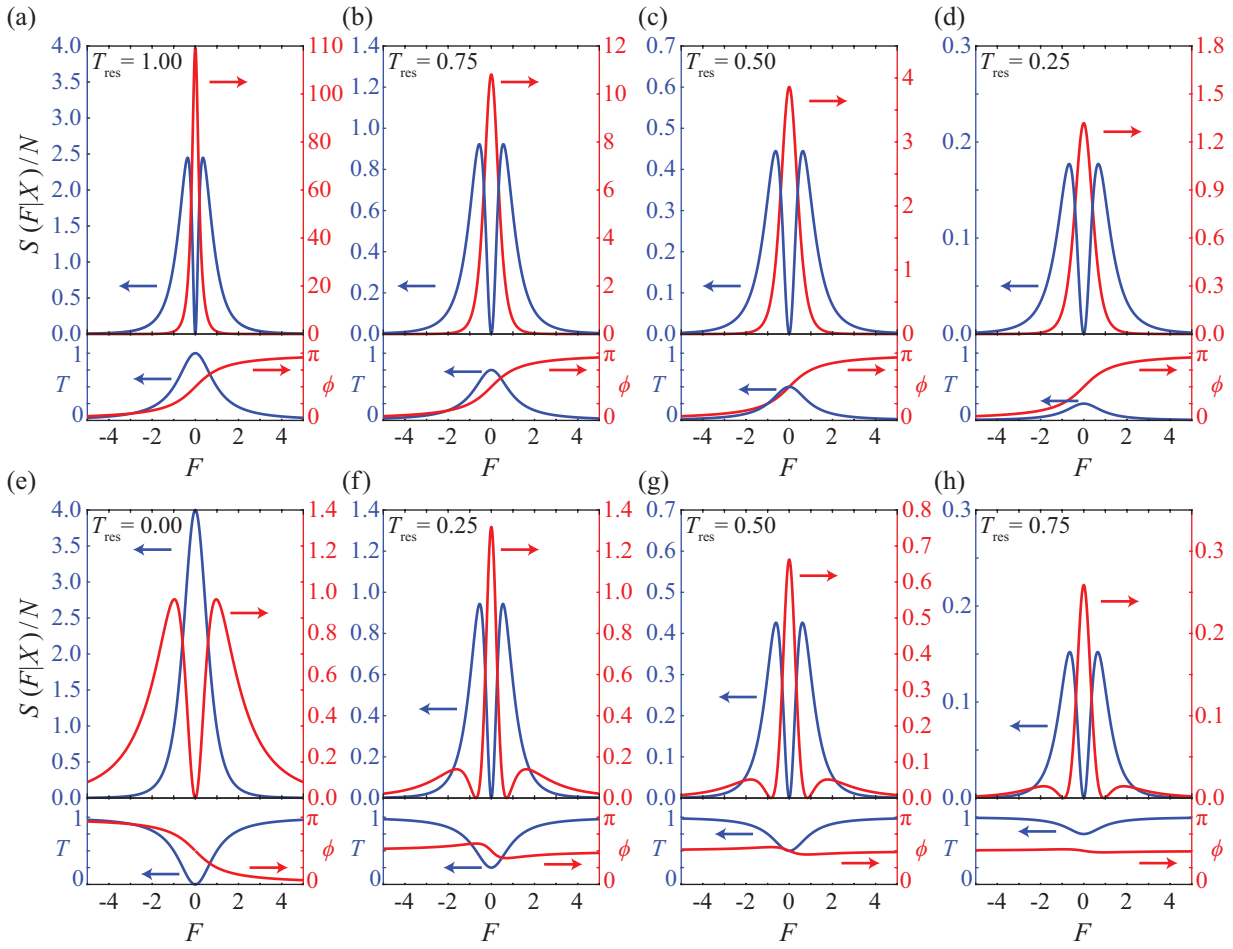


Figure 6.3: Comparison of the frequency sensitivity per photon for transmission (blue, left axis) and phase (red, right axis) measurements as a function of frequency. On the top plots (a-d) the off resonance transmission is 0% and the resonance transmission changes from 100% to 25% in steps of 25%. On the bottom plots (e-h) the off resonance transmission is 100% and the on resonance transmission changes from 0% to 75%. As such, each column has the same magnitude difference between the maximum and minimum transmissions. The lower subplots show the transmission and phase of the system for each set of resonance and far off resonance transmissions. © IOP Publishing. Reproduced with permission. All rights reserved [75].

Squeezing parameter (s)	F_{Opt} for $T_{\text{res}} = 1$, $T_{\text{off}} = 0$
0	$\approx \pm 0.71$
0.5	$\approx \pm 0.66$
1	$\approx \pm 0.55$
1.5	$\approx \pm 0.45$
2	$\approx \pm 0.36$
$\vdots$	
s	$\pm\frac{\sqrt{\sqrt{\text{sech}^2(2s)+8\,\text{sech}(2s)}-\text{sech}(2s)}}{2}$

Table 6.1: Optimal frequency, F_{Opt}, for transmission measurements of a peak resonance. As the squeezing parameter, s, increases, the optimal transmission frequency tends towards zero as the QCRB for transmission tends towards zero at $T = 1$.

sensitivity behavior for transmission based measurements. For a dip resonance with $T_{\text{res}} = 0$, the maximum sensitivity is at resonance where the uncertainty in transmission is zero but so is the slope. However, since the uncertainty approaches zero faster we have a non-zero sensitivity on resonance. This is due to any photon passing through the system signifying a change in transmission, from zero, and thus a shift in resonance frequency.

In the limit of infinite squeezing, where $\langle \Delta^2 T \rangle = T - T^2$, the transmission QCRB is symmetric around $T = 0.5$, *i.e.* $T = 0.5 \pm x$ for $0 \leq x \leq 0.5$ have the same transmission uncertainty. In this limit, there is also a symmetry to the frequency sensitivity such that flipping $T_{\text{res}} \to 1 - T_{\text{res}}$ and $T_{\text{off}} \to 1 - T_{\text{off}}$ does not change the sensitivity. The symmetry in sensitivity can be seen even at $s = 2$ in Figs. 6.3(b) and 6.3(f), Figs. 6.3(c) and 6.3(g), and Figs. 6.3(d) and 6.3(h), where the sensitivity from transmission measurements are nearly the same in each pair. In the infinite squeezing limit, the transmission measurement sensitivity in Fig. 6.3(a) would also peak at 4, just like Fig. 6.3(e). Assuming no internal loss, this can be interpreted as comparing the transmission and reflection of the sensor, like a cavity, where the top plots of Fig. 6.3 correspond to the transmission through, and the bottom plots the reflection from, the sensor. As such, both transmission and reflection give the same frequency sensitivity in the infinite squeezing limit. Below this limit, whichever has the lowest measured power at the optimal frequency will typically give the better sensitivity since at zero squeezing, high transmission has greater uncertainty than low transmission, see Fig 4.3.

Using phase measurements, the maximum slope and maximum sensitivity, for $T_{\text{res}} > 0$, both occur at the resonance frequency as shown by the red traces in Fig. 6.3. Unlike the transmission QCRB being dependent on transmission, the phase QCRB is not dependent on phase, thus only the phase slope and the losses from the sensor transmission affect the sensitivity, not the phase itself. For the dip response, Figs. 6.3(e-h), there are two lobes of local maxima sensitivity that appear. The lobs are most prevalent in Fig. 6.3(f). Looking at the phase response, shown in red in the lower plot, and starting from resonance and moving outwards, the phase reaches an extrema, reverses direction, and slowly tends to zero

at far off-resonance. This leads to three local maxima in the slope of the phase response and two zeros. The global maximum slope is on resonance and is much larger that the outer local maxima, leading to the on resonance maximum frequency sensitivity even though the transmission at that point is minimum. The maximum slope and maximum sensitivity occur at resonance in all cases, except for $T_{\text{res}} = 0$ in Fig. 6.3(e) where the phase uncertainty at that point is infinite due to zero transmission and thus only the two local maxima lobes remain. As squeezing increases, the lobes move outward to higher transmissions for all cases.

Between transmission and phase measurements, which one has highest sensitivity depends on the frequency. Other than for $T_{\text{res}} = 0$, the maximum sensitivity using phase measurements is greater than the maximum transmission sensitivity. A change in squeezing does not affect which measurement gives the maximum sensitivity as Fig. 6.4 shows from $s = 0$, coherent state, to $s = 2$. For most cases, the sensitivity nears an asymptote by $s = 2$ and further increases in squeezing typically offer little increase in sensitivity. However, for the $T_{\text{res}} = 1$ peak, the phase measurement sensitivity continuous to grow. Looking at Eq. (6.12), the phase uncertainty for zero extraneous loss and infinite squeezing is bounded by the transmission of the system

$$\left\langle \Delta^2 \phi \right\rangle \geq \frac{1}{4 \left\langle \hat{n}_p \right\rangle_r} \left(\frac{1}{T} - 1 \right). \tag{6.30}$$

For perfect transmission the uncertainty limit is zero but for imperfect transmission it is bounded, as we can see from Eq. (6.30). Thus, for a $T_{\text{res}} = 1$ the sensitivity from a phase estimation will continue to grow with increased squeezing but for other resonance transmissions it quickly approaches an asymptotic limit. However, since the sensitivity is only large on resonance, the phase measurement would not work well when it is the HWHM that is changing, due to the F^2 term when converting from F to Δ_f sensitivities, see Eq. (6.6). This bound, Eq. (6.30), also causes the lobes for the dip resonance to tend towards far off resonance frequencies as squeezing increases. For transmission, the measurement uncertainty is always limited by the ultimate bound for transmission estimation. Thus, the frequency sensitivity for infinite squeezing is limited by that ultimate bound as well. The dip resonance for $T_{\text{res}} = 0$ represents the maximum sensitivity from the transmission measurements and is the same for all squeezing, that is, it does not offer a quantum enhancement for any state, not just a bTMSS.

To show that phase measurement sensitivity is, in general, not always better than than the transmission measurement sensitivity, we consider other lineshapes, such as a Butterworth lineshape,

$$T_0 = \frac{1}{1 + F^{2N}}, \tag{6.31}$$

where N is the order of the Butterworth. For the Butterworth, we could not find a transfer function for arbitrary on and off resonance transmission. Luckly, when the transfer function is not known, the intensity transmission can be used to approximate the phase response, but there does not exist a unique solution for the phase for a given transmission. In this case, the Bode gain-phase relation[81] will give the minimum phase response[82] for a given transmission response.

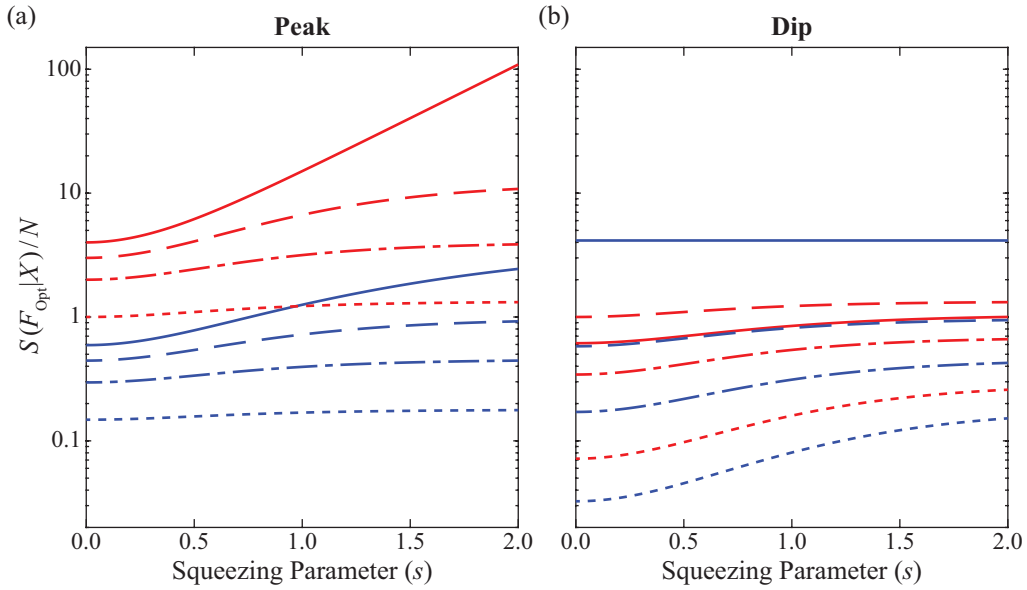


Figure 6.4: Sensitivity per photon at the optimal frequency F_{Opt} as the squeezing parameter changes for transmission (blue) and phase (red) measurements. The left plots (a) are for peak resonances and the right ones (b) are for a dip. Each plot corresponds to the max sensitivity in the plots in Fig. 6.3 for $|T_{\mathrm{res}} - T_{\mathrm{off}}| = 1$ (solid line) on the far left in Fig. 6.3, $|T_{\mathrm{res}} - T_{\mathrm{off}}| = 0.75$ (dashed line) center left, $|T_{\mathrm{res}} - T_{\mathrm{off}}| = 0.5$ (dashed-dotted line) center right, and $|T_{\mathrm{res}} - T_{\mathrm{off}}| = 0.25$ (dotted line) on the far right in Fig. 6.3. © IOP Publishing. Reproduced with permission. All rights reserved[75].

N	Max Slope	Approx	at F	Approx
1	$\pm\frac{3\sqrt{3}}{8}$	± 0.650	$\mp\sqrt{\frac{1}{3}}$	∓ 0.557
2	$\pm\frac{5\sqrt[4]{5\times 3^3}}{16}$	± 1.07	$\mp\sqrt[4]{\frac{3}{5}}$	∓ 0.880
3	$\pm\frac{6\sqrt[6]{3\times 5^5}}{32}$	± 1.29	$\mp\sqrt[6]{\frac{5}{7}}$	∓ 0.945
$\vdots$				
N	$\pm\frac{2N\left(\frac{2N-1}{2N+1}\right)^{1-\frac{1}{2N}}}{\left(1+\frac{2N-1}{2N+1}\right)^2}$	$\lim_{N\to\infty} = \pm\frac{N}{2}$	$\mp\sqrt[2N]{\frac{2N-1}{2N+1}}$	$\lim_{N\to\infty} = \mp 1$

Table 6.2: Maximum slope and frequency, F, at which it occurs for different orders of the Butterworth lineshape. As the order N increases, the frequency of the maximum slope tends towards the HWHM, $F = 1$, and the magnitude of the slope goes to infinity.

A first order Butterworth is the same as a Lorentzian and higher orders increase the maximum transmission slope, as shown in Table 6.2. Also, the transmission changes less between the maximum slope frequencies as the order increases. As can be seen in Fig. 6.5(d), this causes the phase to flatten out near resonance and thus have the largest slope slightly off resonance.

The Butterworth lineshape is more common in electronic filter design than in physics, but is useful to show the interplay between the transmission and phase slopes for frequency shift estimation. This will also give some insight into arbitrary response functions which may have a single sharp transmission slope on one side of resonance. To compare sensitivities from either transmission or phase measurements, we define a figure of merit (FOM) as

$$\text{FOM} = \frac{\max\limits_F S(F|\phi)}{\max\limits_F S(F|T)}, \tag{6.32}$$

such that FOM>1 means phase measurements are more sensitive and FOM<1 means that transmission measurements are. The FOM for the Lorentzian and third-order Butterworth are shown in Fig. 6.5. For the Butterworth, the phase response is solved for numerically, as explained in Appendix C, as the analytical solution is difficult to find for arbitrary on and off resonance transmissions. As shown in Fig. 6.5(b), there is a large parameter space between the red lines where transmission measurements give a higher sensitivity than phase measurements for the third-order Butterworth lineshape. While this does show that phase measurement is not always best, it should be noted that for a peak response with $T_{\text{off}} = 0$ phase measurements gave the highest sensitivity for both lineshapes shown here. However, for a dip resonance, the transmission measurement often has a higher sensitivity for the third-order Butterworth.

To examine the effect of extraneous loss, we return to the Lorentzian lineshape. At a single frequency, loss affects the frequency sensitivity, Eqs. (6.28) and (6.29), the same way it does the transmission and phase estimation, Eqs. (4.41) and (6.12) respectively. A linear

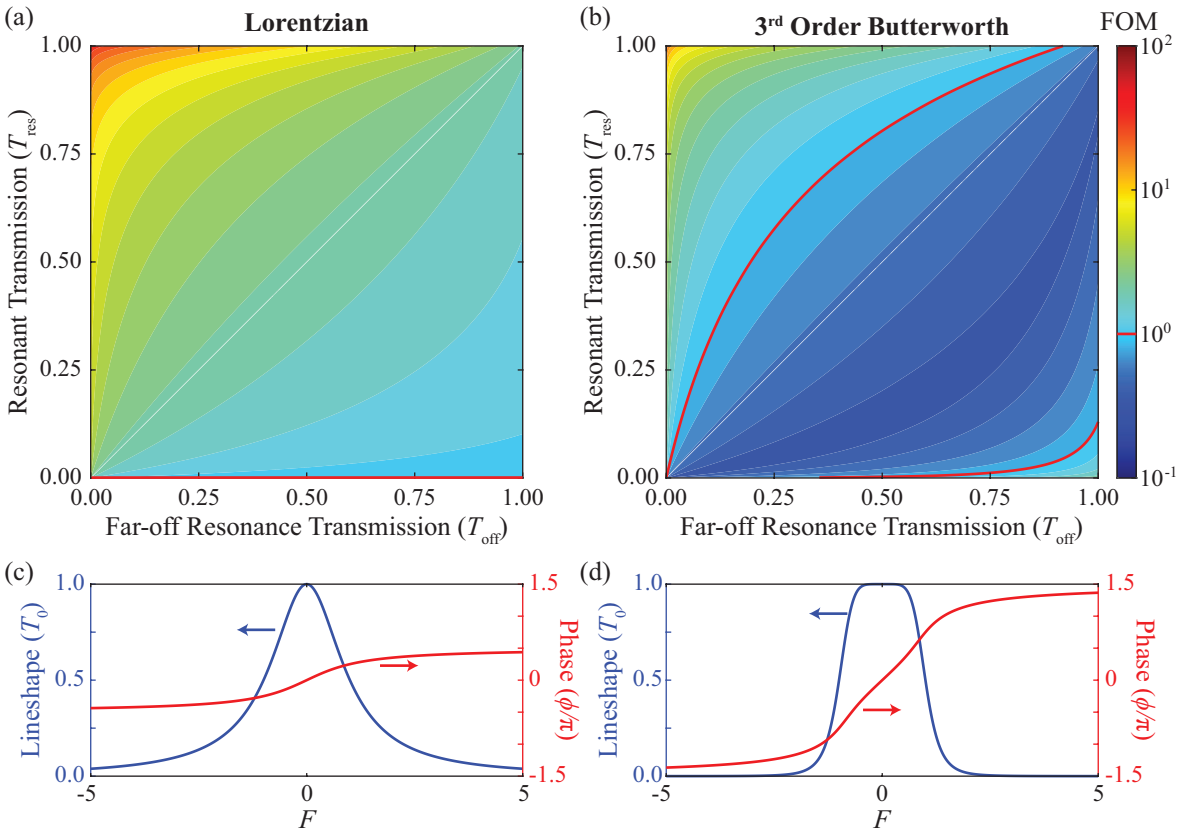


Figure 6.5: A comparison of the sensitivity obtained with phase and transmission measurements for different system transmissions with either a Lorentzian or third-order Butterworth lineshape. The top contour plots, (a) and (b), show the figure of merit (FOM) for each measurement and the bottom plots, (c) and (d), show the lineshape and phase for a peak transmission. The red line in (a) and (b) marks where the two measurements have the same frequency sensitivity. For the Butterworth lineshape (b), there is a larger parameter space between the red lines in which transmission outperforms phase measurements than there is for the Lorentzian lineshape. Reproduced with permission. All rights reserved [75].

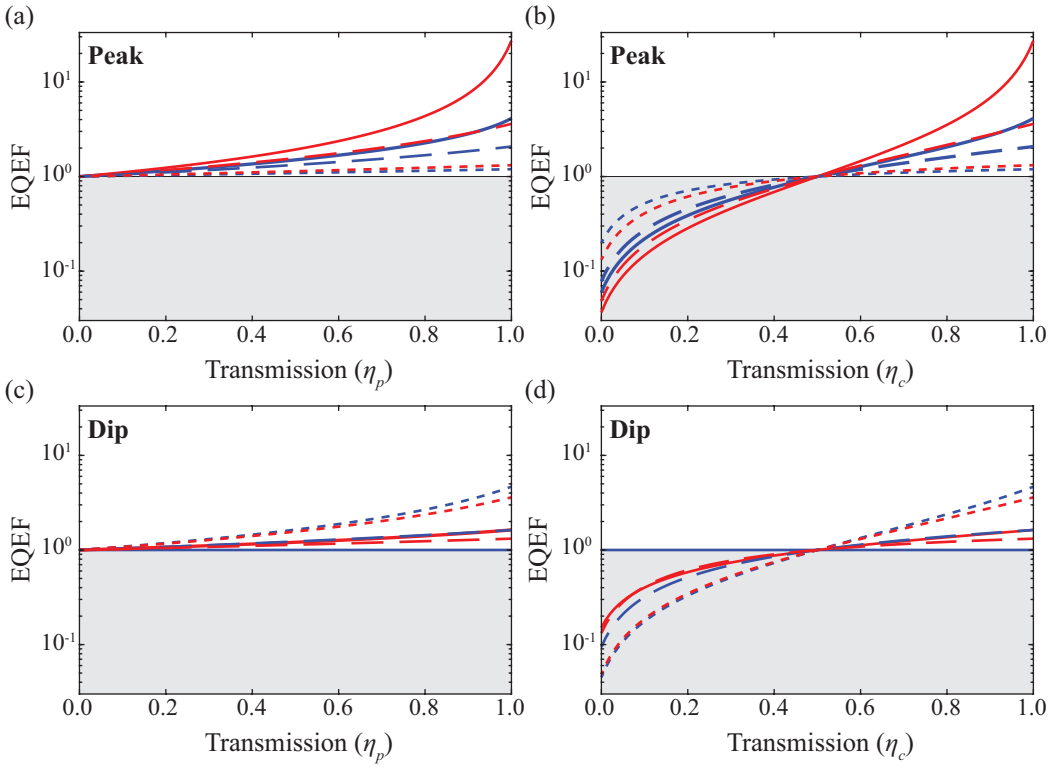


Figure 6.6: Effects of losses on degree of quantum enhancement (EQEF), top row for peak and bottom row for dip with probe on the left and conjugate on the right column, for a squeezing parameter of $s = 2$. Probe losses before or after the system have the same effect on the EQEF. The gray region is where the EQEF<1, marking the region where a coherent state outperforms the bTMSS. For both phase and transmission measurements, the bTMSS always has a quantum enhancement when $\eta_c > 50\%$. Each plot corresponds to the max sensitivity in the plots in Fig. 6.3 for $|T_{\text{res}} - T_{\text{off}}| = 1$ (solid line) on the far left in Fig. 6.3, $|T_{\text{res}} - T_{\text{off}}| = 0.75$ (dashed line) center left, and $|T_{\text{res}} - T_{\text{off}}| = 0.25$ (dotted line) on the far right in Fig. 6.3. The dashed-dotted line is omitted for figure clarity. © IOP Publishing. Reproduced with permission. All rights reserved[75].

decrease in the enhancement for probe losses, including the transmission to be measured such as in Eqs. (4.46) and (4.45). For conjugate loss there is a nonlinear change due to the loss in correlation between the probe and conjugate mode. Probe losses made the bTMSS QCRB more like the coherent state bound, conjugate loss more like the thermal state bound. Losses also change the frequency at which the maximum sensitivity occurs for both transmission and phase measurements. Thus the maximum sensitivity has a more complicated relationship with extraneous loss than transmission or phase estimation does.

Since the purpose of using quantum states is to have a quantum enhancement, we introduce an effective quantum enhancement factor (EQEF) consisting of the ratio of the bTMSS maximum sensitivity to the maximum sensitivity for a coherent state with the same

extraneous losses, that is

$$\mathrm{EQEF}(X) = \frac{\max\limits_{F} S(F|X)_{\mathrm{bTMSS}}}{\max\limits_{F} S(F|X)_{\mathrm{Coh}}}, \tag{6.33}$$

to quantify the enhancement when using a quantum state over a classical state and the effects of loss. Note that the frequency will be different for each state and also that a higher EQEF does not mean that one measurement is more sensitive than the other, only that the measurement has the greater enhancement from an optimal classical measurement. Fig. 6.6 plots the effects of probe and conjugate loss on the EQEF for a squeezing of $s = 2$. For probe loss, the effect is the same for loss being before or after the system, as the optimal frequency for the coherent state sensitivity is independent of extraneous loss. To show this, for transmission based measurements the coherent state sensitivity is

$$S(F|T)_{\mathrm{Coh}} = \langle \hat{n}_p \rangle_r \left\{ \frac{(1+F^2)^3 (F^2 T_{\mathrm{off}} + T_{\mathrm{res}})}{4F^2 \eta_p (T_{\mathrm{off}} - T_{\mathrm{res}})^2} \right\}^{-1}. \tag{6.34}$$

As η_p changes, it scales the sensitivity and thus will not change the optimal frequency. The transmission EQEF is then

$$\begin{aligned} \mathrm{EQEF}(T) \quad = \max_{F^{(\mathrm{bTMSS})}} \quad & \frac{(1+F_{\mathrm{opt}}^{(\mathrm{coh})2})^3 (F_{\mathrm{opt}}^{(\mathrm{coh})2} T_{\mathrm{off}} + T_{\mathrm{res}})}{F_{\mathrm{opt}}^{(\mathrm{coh})2}} \\ & \times \left\{ \frac{(1+F^{(\mathrm{bTMSS})2})^3 (F^{(\mathrm{bTMSS})2} T_{\mathrm{off}} + T_{\mathrm{res}})}{F^{(\mathrm{bTMSS})2}} \right. \\ & \left. - \frac{(1+F^{(\mathrm{bTMSS})2})^2 (F^{(\mathrm{bTMSS})2} T_{\mathrm{off}} + T_{\mathrm{res}})^2}{4F^{(\mathrm{bTMSS})2} (T_{\mathrm{off}} - T_{\mathrm{res}})^2} T_p \eta_p H_c [1 - \mathrm{sech}(2s)] \right\}^{-1}, \end{aligned} \tag{6.35}$$

where $F_{\mathrm{opt}}^{(\mathrm{coh})}$ is the optimal coherent state frequency and $F^{(\mathrm{bTMSS})}$ is the optimal frequency for the bTMSS sensitivity. The second term in the curly brackets contains $T_p \eta_p$ and only here does the extraneous probe loss appear. Since the transmissions are multiplied by each other, loss before or after probing the system gives the exact same EQEF. The frequency dependence with losses for the bTMSS comes from the quantum enhancement term having an extra $(F^2 T_{\mathrm{off}} + T_{\mathrm{res}})$ factor and one less $(1+F^2)$ factor compared to the classical limit term, for both measurements. Thus, the balance between the two terms shifts as losses increase, affecting the optimal frequency. As with transmission or phase estimation, probe losses do not affect whether there is a quantum advantage, just the degree of enhancement. However, conjugate losses at >50% make the bTMSS worse than the coherent state for frequency sensitivity.

Similarly, which measurement has a higher EQEF does not change for probe losses but it does for conjugate losses. At 50% conjugate loss, the measurement that without loss would

have the greater quantum enhancement becomes the worse measurement. This is due to the enhancement term switching sign and becoming negative, due to H_c, as the measurement that is farthest away from a EQEF=1 is always consistent. That is, the measurement with the highest EQEF at $> 50\%$ conjugate transmission has the lowest EQEF at $< 50\%$ conjugate transmission.

The frequency sensitivity, much like the phase and transmission uncertainty, only has a large quantum enhancement when transmissions are high. This is true both for the propagation and detection transmissions as well as the resonance transmissions, as shown in Fig. 6.6 and Fig. 6.4. The phase measurement typically has a higher frequency sensitivity for the Lorentzian lineshape. However, in general this is not always the case, as Fig. 6.5 shows. The sensitivity for each measurement is dependent on the slope of the measurement with frequency as well as the transmission at that point. The Lorentzian lineshape peak resonance has a large phase slope at the maximum transmission point, leading the phase measurements to have the highest frequency sensitivity. Increasing the slope of transmission by using the third-order Butterworth allows the transmission measurement to outperform the phase measurement. Thus, a detailed model of the actual resonance sensor is needed in order to determine which measurement is optimal.

Chapter 7

Conclusion

The enormous usefulness of mathematics in the natural sciences is something bordering on the mysterious and there is no rational explanation for it

— Eugene Wigner, *Philosophical Reflections and Syntheses*

In this thesis we have covered transmission estimation with Gaussian states of light. Transmission is an important parameter for metrology as it can be used as the readout of many sensors, *i.e.* resonance sensors, and is necessary for characterizing many optical systems, *i.e.* interferometers and communications. The work presented primarily focused on the bTMSS as the multimode nature of the state allows for differential detection, which reduces technical noise. Also, being a bright state, the bTMSS can compete with the coherent state and surpass the state-of-the-art for metrology.

In Chapters 2 and 3 we covered the basics of quantum metrology with Gaussian states of light by first introducing the Gaussian states and covering various ways to mathematically represent them. The Fisher information and Cramér-Rao bound were next introduced as well as the extension of both via quantum mechanics. It was discussed that the QFI and QCRB are not for quantum states specifically, but set lower bound for the uncertainty in estimating a parameter based on the quantum descriptions of states. This allows for parameter estimation bounds that are independent of the measurement used to extract the information.

Chapters 4 and 5 derived the theory for and showed saturation of the QCRB of the bTMSS in the presence of extraneous loss. While the bTMSS does not possess the same low QCRB as the Fock state or vTMSS for the same number of probing photons, it can have an overall lower bound due to being able to be generated with orders of magnitude more photons. We presented the experimental saturation of the QCRB for the bTMSS, and coherent state, using readily available measurement techniques, the optimized intensity difference measurement. This measurement saturates the QCRB both for a pure bTMSS and a lossy bTMSS with imperfect state generation. Thus, the high powered bTMSS can be used to enhance current cutting edge sensors.

Finally, in Chapter 6 we compared transmission estimation to phase estimation using the bTMSS. This state is able to enhance both estimations and the QCRB for both parameters is

saturated by optimized homodyne measurements. This allows for a fair comparison of phase and transmission estimation. Using resonance sensors, which have a simultaneous change in both phase and transmission, we were able to compare and contrast transmission and phase measurements for estimating a change in the resonance frequency. For the common Lorentzian lineshape, the phase measurement is more sensitive than the transmission measurement except in the extreme case of zero transmission on resonance. For a lineshape with a sharper transmission slope, as is the case with Butterworth lineshapes, the transmission measurement can achieve a higher sensitivity than the phase measurement for a larger set of on and off resonance transmission values of the resonance sensor.

Our work is only the initial building block for future works of greater complexity. I have worked with only a single parameter at a time. The expansion to multi-parameter estimation has many complexities including the QCRB becoming a covariance matrix for the set of parameters. One of the main concerns is that it is not always possible to saturate the quantum Cramér-Rao bound matrix and only a subset of parameters can have minimum uncertainty estimations at a time.

7.1 Future outlook: multiple transmissions

Since we have a two mode quantum state, one of the first expansions to measuring the transmission of one of the modes would be measuring transmission of both modes. Simultaneous transmission measurements of two parameters inherently have a speed up in the calibration or characterization of multiple systems. However, initial calculations have suggested that measuring two different transmissions with the bTMSS, one with the probe mode and the other with the conjugate mode, is worse than measuring them with two coherent states for all transmissions. This is probably due to each mode being a displaced thermal state when treated separately and the unknown transmission of each state removing any usable correlations. However it may be possible that, if both modes are seeded at the same power, the difference in transmission between the two modes may be estimated more precisely than with two coherent states of equal power. However, additional work needs to be done to check these preliminary results.

Another extension is to measure two transmissions that are functions of a single parameter. This is then a single parameter estimation problem even though it involves two transmissions. For such systems, both modes can be used to measure a transmission and then jointly used to estimate a third parameter.

7.1.1 Two transmission measurements for estimating a single parameter

For a system with two addressable transmissions that depend on the same parameter using a bTMSS there can be an improvement in probing the system with the probe and conjugate mode, one mode for each transmission. For example, a resonance sensor with a different resonance for orthogonal polarizations or angles of incidence that have resonance frequencies

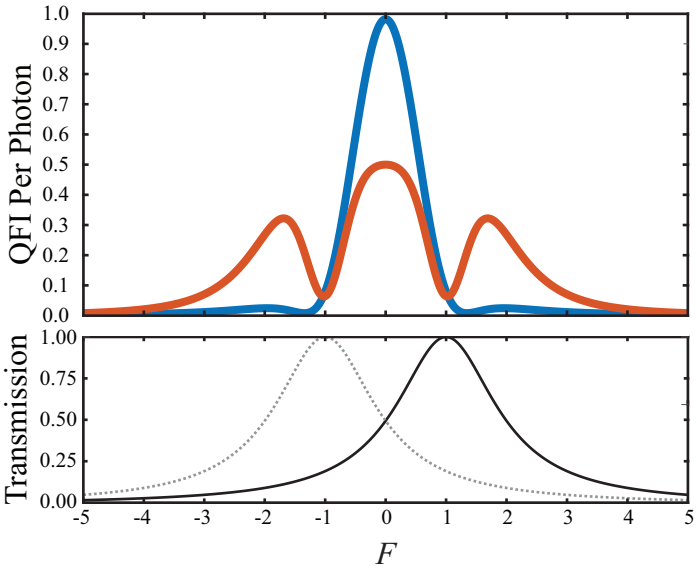


Figure 7.1: Plot of the QFI per probing photon, thus probe plus conjugate photons, for the bTMSS (blue) and coherent state (red) probing a resonance sensor with two resonances. The bottom plot shows the transmission of the resonance sensor with a Lorentzian line shape shifted by one HWHM left (grey dotted) or right (black solid). For regions in which the transmission slope has an opposite sign for each resonance, the bTMSS has a higher QFI per photon than the coherent state. To determine if this is always true requires further analysis.

that shift simultaneously due to some external parameter of interest. This is an improvement over probing either one transmission with the probe mode of the bTMSS or probing both transmissions with two coherent states. The main issue with probing with both modes of the bTMSS is the loss of correlation between the two modes due to the loss of conjugate photons. To overcome this issue, there needs to be a cross term in the QFI where probing with correlated modes gives additional information than probing with uncorrelated modes. This information needs to be large enough such that probing with both modes gives more information than that which is lost from the conjugate mode loss.

Figure 7.1 shows the results of some initial calculations for the bTMSS with $s = 2$ and equal seeding power for the probe and conjugate. Both modes are used to probe Lorentzian lineshape resonance systems. The results are compared with two coherent states, one probing each transmission. We can see that there is a cross term for the bTMSS that helps increase the information gained when the transmission slopes of each resonance of the sensor are in opposite directions, one positive and the other negative, and a reduction in information when the slopes are in the same direction. This cross term information does allow the bTMSS to have a higher QFI per photon than a pair of coherent states. However, more analysis needs to be done to see in which parameter space the quantum enhancement of the bTMSS holds true. Such as an imbalance in on-resonance transmissions or one of the resonances being a dip instead of a peak.

Part III

Appendices

Appendix A

Covariance Matrix for bTMSS Generated in an Absorptive Medium

To analytically solve for the covariance matrix of a bTMSS generated in an absorptive medium, the generation process can be split into an infinite series of infinitesimal squeezers and beamsplitters. To simplify the calculation, the phases of all the fields and operators are chosen such that the operators have real coefficients. This will always create an intensity difference squeezed bTMSS, such as the one used in the experiment described in Chapter 5. As stated previously, the squeezing and beam splitter operations can be broken up using [51,64]

$$\hat{S}_{p,c}(\xi) = \prod_{n=1}^{N} \hat{S}_{p,c}(\xi/N), \tag{A.1}$$

$$\hat{B}_{p}(T_x) = \prod_{n=1}^{N} \hat{B}_{p}(\sqrt[N]{T_x}), \tag{A.2}$$

$$\hat{B}_{c}(T_y) = \prod_{n=1}^{N} \hat{B}_{c}(\sqrt[N]{T_y}), \tag{A.3}$$

where T_x and T_y are the transmissions of the probe and conjugate mode, respectively. The total operation for the distributed loss during state generation is

$$\hat{S}_{p,c}(\xi; T_x, T_y|N) = \prod_{n=1}^{N} \hat{B}_{c}(\sqrt[N]{T_y})\hat{B}_{p}(\sqrt[N]{T_x})\hat{S}_{p,c}(\xi/N). \tag{A.4}$$

Here, the covariance matrix and displacement vector will be solved for following the work done by Jasperse *et. al* [64]. Working in the Heisenberg picture, the photon annihilation

operators for the probe and conjugate modes transform as

$$\hat{S}^{\dagger}_{p,c}(s)\hat{a}_p\hat{S}_{p,c}(s) = \hat{a}_p\cosh(s)+\hat{a}^{\dagger}_c\sinh(s), \tag{A.5}$$

$$\hat{S}^{\dagger}_{p,c}(s)\hat{a}_c\hat{S}_{p,c}(s) = \hat{a}_c\cosh(s)+\hat{a}^{\dagger}_p\sinh(s), \tag{A.6}$$

$$\hat{B}^{\dagger}_p(T_x)\hat{a}_p\hat{B}_p(T_x) = \sqrt{T_x}\hat{a}_p+\sqrt{1-T_x}\hat{x}_i, \tag{A.7}$$

$$\hat{B}^{\dagger}_c(T_y)\hat{a}_c\hat{B}_c(T_y) = \sqrt{T_y}\hat{a}_c+\sqrt{1-T_y}\hat{y}_i, \tag{A.8}$$

where $\hat{x}_i$ and $\hat{y}_i$ are vacuum mode operators. As shown in Fig. A.1, the operators for each step of the process recursively rely on the previous step as,

$$\hat{a}^{(n+1)}_p = \sqrt{T_x}\left\{\hat{a}^{(n)}_p\cosh(s)+\hat{a}^{\dagger(n)}_c\sinh(s)\right\}+\sqrt{1-\sqrt[N]{T_x}}\hat{x}_{n+1} \tag{A.9}$$

$$\begin{aligned}\hat{a}^{(n+1)}_p = \sqrt{T_x}\Bigg\{&\left[\sqrt{T_x}\left[\hat{a}^{(n-1)}_p\cosh(s)+\hat{a}^{\dagger(n-1)}_c\sinh(s)\right]+\sqrt{1-\sqrt[N]{T_x}}\hat{x}_n\right]\cosh(s)\\ &+\left[\sqrt{T_y}\left[\hat{a}^{(n-1)}_p\sinh(s)+\hat{a}^{\dagger(n-1)}_c\cosh(s)\right]+\sqrt{1-\sqrt[N]{T_y}}\hat{y}^{\dagger}_n\right]\sinh(s)\Bigg\}\\ &+\sqrt{1-\sqrt[N]{T_x}}\hat{x}_{n+1}\end{aligned} \tag{A.10}$$

$$\hat{a}^{\dagger(n+1)}_c = \sqrt{T_y}\left\{\hat{a}^{(n)}_p\sinh(s)+\hat{a}^{\dagger(n)}_c\cosh(s)\right\}+\sqrt{1-\sqrt[N]{T_y}}\hat{y}^{\dagger}_{n+1} \tag{A.11}$$

$$\begin{aligned}\hat{a}^{\dagger(n+1)}_c = \sqrt{T_y}\Bigg\{&\left[\sqrt{T_x}\left\{\hat{a}^{(n-1)}_p\cosh(s)+\hat{a}^{\dagger(n-1)}_c\sinh(s)\right\}+\sqrt{1-\sqrt[N]{T_x}}\hat{x}_n\right]\sinh(s)\\ &+\left[\sqrt{T_y}\left\{\hat{a}^{(n-1)}_p\sinh(s)+\hat{a}^{\dagger(n-1)}_c\cosh(s)\right\}+\sqrt{1-\sqrt[N]{T_y}}\hat{y}^{\dagger}_n\right]\cosh(s)\Bigg\}\\ &+\sqrt{1-\sqrt[N]{T_y}}\hat{y}^{\dagger}_{n+1}.\end{aligned} \tag{A.12}$$

This can be written as

$$\hat{a}^{(N)}_p = \mathcal{A}_1\hat{a}^{(0)}_p+\mathcal{A}_2\hat{a}^{\dagger(0)}_c+\mathcal{A}_3\hat{x}_1+\mathcal{A}_4\hat{y}^{\dagger}_1+\cdots+\mathcal{A}_{2N+1}\hat{x}_N+\mathcal{A}_{2N+2}\hat{y}^{\dagger}_N \tag{A.13}$$

$$= \mathcal{A}_1\hat{a}^{(0)}_p+\mathcal{A}_2\hat{a}^{\dagger(0)}_c+\sum_{i=1}^{N}\mathcal{A}_{2i+1}\hat{x}_i+\sum_{i=1}^{N}\mathcal{A}_{2i+2}\hat{y}^{\dagger}_i \tag{A.14}$$

$$\hat{a}^{\dagger(N)}_c = \mathcal{B}_1\hat{a}^{(0)}_p+\mathcal{B}_2\hat{a}^{\dagger(0)}_c+\mathcal{B}_3\hat{x}_1+\mathcal{B}_4\hat{y}^{\dagger}_1+\cdots+\mathcal{B}_{2N+1}\hat{x}_N+\mathcal{B}_{2N+2}\hat{y}^{\dagger}_N \tag{A.15}$$

$$= \mathcal{B}_1\hat{a}^{(0)}_p+\mathcal{B}_2\hat{a}^{\dagger(0)}_c+\sum_{i=1}^{N}\mathcal{B}_{2i+1}\hat{x}_i+\sum_{i=1}^{N}\mathcal{B}_{2i+2}\hat{y}^{\dagger}_i. \tag{A.16}$$

The displacement vector for this state when seeding only the probe mode is given by

$$\vec{d} = \begin{pmatrix}\mathcal{A}_1\alpha\\ \mathcal{B}_1\alpha\\ \mathcal{A}_1\alpha\\ \mathcal{B}_1\alpha\end{pmatrix}, \tag{A.17}$$

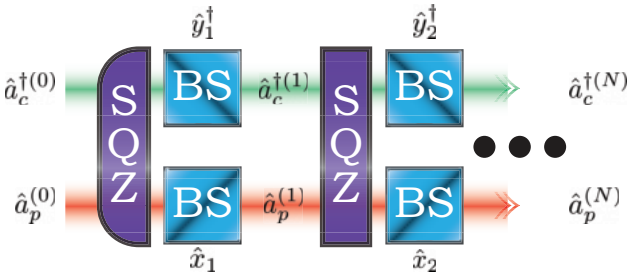


Figure A.1: Schematic of the model of the absorptive medium used as a source of squeezed light. The initial probe and conjugate fields are squeezed (SQZ) and then each mode is mixed with a vacuum mode, $\hat{x}_1$ for probe and $\hat{y}_1^\dagger$ for the conjugate, via beam splitters (BS) to generate the field due to the first iteration. The process is repeated again for the next iteration and so on until the Nth iteration.

since $\langle \hat{a}_c \rangle = \langle \hat{x}_i \rangle = \langle \hat{y}_i \rangle = 0$ due to initially being vacuum modes. To solve for the covariance matrix, $\boldsymbol{\sigma}$, the terms can be solved in a similar fashion. For the diagonal probe term, σ_{11},

$$\begin{aligned}
\left\langle \hat{a}_p^{\dagger(N)} \hat{a}_p^{(N)} \right\rangle &= \left\langle \left(\mathcal{A}_1 \hat{a}_p^{\dagger(0)} + \mathcal{A}_2 \hat{a}_c^{(0)} + \sum_{i=1}^{N} \mathcal{A}_{2i+1} \hat{x}_i^\dagger + \sum_{i=1}^{N} \mathcal{A}_{2i+2} \hat{y}_i \right) \right. \\
&\quad \left. \times \left(\mathcal{A}_1 \hat{a}_p^{(0)} + \mathcal{A}_2 \hat{a}_c^{\dagger(0)} + \sum_{i=1}^{N} \mathcal{A}_{2i+1} \hat{x}_i + \sum_{i=1}^{N} \mathcal{A}_{2i+2} \hat{y}_i^\dagger \right) \right\rangle \qquad \text{(A.18)} \\
&= \left\langle \mathcal{A}_1^2 \hat{a}_p^{\dagger(0)} \hat{a}_p^{(0)} + \mathcal{A}_2^2 + \sum_{i=1}^{N} \mathcal{A}_{2i+2}^2 \right\rangle \qquad \text{(A.19)} \\
\left\langle \hat{a}_p^{(N)} \hat{a}_p^{\dagger(N)} \right\rangle &= \left\langle \mathcal{A}_1^2 \left(\hat{a}_p^{\dagger(0)} \hat{a}_p^{(0)} + 1 \right) + \sum_{i=1}^{N} \mathcal{A}_{2i+1}^2 \right\rangle, \qquad \text{(A.20)}
\end{aligned}$$

where the vacuum terms appear in either normal or anti-normal ordering of the operators and the summations are over only one index due to the commutation relation or the annihilation operator. The covariance matrix term is then

$$\sigma_{11} = \sigma_{33} = \left\langle \hat{a}_p^{\dagger(N)} \hat{a}_p^{(N)} + \hat{a}_p^{(N)} \hat{a}_p^{\dagger(N)} \right\rangle - 2d_1^2 = \sum_{i=1}^{2N+2} \mathcal{A}_i^2. \qquad \text{(A.21)}$$

Thus, it can be shown that

$$\boldsymbol{\sigma} = \begin{pmatrix} \sum_{i=1}^{2N+2} \mathcal{A}_i^2 & 0 & 0 & \sum_{i=1}^{2N+2} \mathcal{A}_i \mathcal{B}_i \\ 0 & \sum_{i=1}^{2N+2} \mathcal{B}_i^2 & \sum_{i=1}^{2N+2} \mathcal{A}_i \mathcal{B}_i & 0 \\ 0 & \sum_{i=1}^{2N+2} \mathcal{A}_i \mathcal{B}_i & \sum_{i=1}^{2N+2} \mathcal{A}_i^2 & 0 \\ \sum_{i=1}^{2N+2} \mathcal{A}_i \mathcal{B}_i & 0 & 0 & \sum_{i=1}^{2N+2} \mathcal{B}_i^2 \end{pmatrix}. \qquad \text{(A.22)}$$

To find the displacement vector and covariance matrix, the solution to the coefficients $\mathcal{A}_i$ and $\mathcal{B}_i$ must be found.

To this end, Eqs. (A.14) and (A.16) can be rewritten as a single matrix equation of the form

$$\begin{pmatrix} \hat{a}_p^{(N)} \\ \hat{a}_c^{\dagger(N)} \end{pmatrix} = \mathbf{A}^N \begin{pmatrix} \hat{a}_p^{(0)} \\ \hat{a}_c^{\dagger(0)} \end{pmatrix} + \sum_{i=1}^{N} \mathbf{A}^{N-i} \begin{pmatrix} \sqrt{1 - \sqrt[N]{T_x}} \hat{x}_i \\ \sqrt{1 - \sqrt[N]{T_y}} \hat{y}_i^\dagger \end{pmatrix}, \qquad \text{(A.23)}$$

where

$$\mathbf{A} = \begin{pmatrix} \sqrt[2N]{T_x}\cosh(s) & \sqrt[2N]{T_x}\sinh(s) \\ \sqrt[2N]{T_y}\sinh(s) & \sqrt[2N]{T_y}\cosh(s) \end{pmatrix}. \tag{A.24}$$

Thus the first two $\mathcal{A}$'s and $\mathcal{B}$'s are given by

$$\begin{pmatrix} \mathcal{A}_1 & \mathcal{A}_2 \\ \mathcal{B}_1 & \mathcal{B}_2 \end{pmatrix} = \mathbf{A}^N. \tag{A.25}$$

The vacuum coefficients can be found by taking the expectation value of the inner product of the second term on the right of Eq. (A.23),

$$\begin{aligned} &\left\langle \left[\sum_{i=1}^{N} \mathbf{A}^{N-i} \begin{pmatrix} \sqrt{1-\sqrt[N]{T_x}}\hat{x}_i \\ \sqrt{1-\sqrt[N]{T_y}}\hat{y}_i^\dagger \end{pmatrix} \right] \left[\sum_{j=1}^{N} \mathbf{A}^{N-j} \begin{pmatrix} \sqrt{1-\sqrt[N]{T_x}}\hat{x}_j \\ \sqrt{1-\sqrt[N]{T_y}}\hat{y}_j^\dagger \end{pmatrix} \right]^\dagger \right\rangle \\ = &\sum_{i=1}^{N}\sum_{j=1}^{N} \mathbf{A}^{N-i} \begin{pmatrix} 1-\sqrt[N]{T_x}\delta_{ij} & 0 \\ 0 & 1-\sqrt[N]{T_y}\delta_{ij} \end{pmatrix} \mathbf{A}^{N-j} \qquad \text{(A.26)} \\ = &\sum_{i=1}^{N} \mathbf{A}^{N-i} \begin{pmatrix} 1-\sqrt[N]{T_x} & 0 \\ 0 & 1-\sqrt[N]{T_y} \end{pmatrix} \mathbf{A}^{N-i} = \sum_{i>2} \begin{pmatrix} \mathcal{A}_i^2 & \mathcal{A}_i\mathcal{B}_i \\ \mathcal{A}_i\mathcal{B}_i & \mathcal{B}_i^2 \end{pmatrix} \equiv \mathbf{X}. \qquad \text{(A.27)} \end{aligned}$$

Following the method from Jasperse *et. al* [64] to solve for the sum in Eq. (A.27), the matrix $\mathbf{A}$ and the transmissions will be expanded into a power series. Setting $\mathbf{A} = \exp(\mathbf{A}_0)$ and $\sqrt[N]{T_x} = \exp\left[\frac{1}{N}\ln(T_x)\right]$, the terms can be expanded to

$$\begin{aligned} \mathbf{A} &= 1 + \frac{1}{N}\mathbf{A}_0 + \mathcal{O}\left(\frac{1}{N^2}\right) \qquad \text{(A.28)} \\ \sqrt[N]{T_x} &= 1 + \frac{1}{N}\ln(T_x) + \mathcal{O}\left(\frac{1}{N^2}\right) \qquad \text{(A.29)} \end{aligned}$$

where

$$\mathbf{A}_0 = \begin{pmatrix} \frac{1}{2}\ln(T_x) & s \\ s & \frac{1}{2}\ln(T_y) \end{pmatrix}. \tag{A.30}$$

Equation (A.27) can then be rewritten using the geometric series relation in the infinite N limit as

$$\begin{aligned} \mathbf{X} &= \frac{1}{N}\sum_{i=0}^{N-1} \mathbf{A}^i \mathbf{T} \mathbf{A}^i \qquad \text{(A.31)} \\ \mathbf{A}_0\mathbf{X}\mathbf{A}_0 &= e^{\mathbf{A}_0}\mathbf{T}e^{\mathbf{A}_0} - \mathbf{T}, \qquad \text{(A.32)} \end{aligned}$$

where

$$\mathbf{T} = \begin{pmatrix} -\ln(T_x) & 0 \\ 0 & -\ln(T_y) \end{pmatrix}. \tag{A.33}$$

Equation (A.32) is a set of linear equations and, since there is no conjugate absorption in our experiment in Ch. 5, setting $T_y = 1$ and solving for $\mathbf{X}$ gives

$$\begin{aligned}
\sum_{i=2}^{2N+2} \mathcal{A}_i^2 &= \frac{1}{2\zeta^2} e^{-\frac{1}{2}\zeta}\Big\{32e^{\frac{1}{2}\zeta}s^2\left(1-\sqrt{T_x}\right) - \left[\sqrt{T_x}\left(1+e^{\zeta}\right) - 2e^{\frac{1}{2}\zeta}\right]\ln^2(T_x) \\
&\qquad -\zeta\sqrt{T_x}\ln(T_x)\left(e^{\zeta}-1\right)\Big\} \qquad \text{(A.34)} \\
\sum_{i=2}^{2N+2} \mathcal{B}_i^2 &= \frac{1}{2\zeta^{\frac{3}{2}}} e^{-\frac{1}{2}\zeta}\Big\{16\left(1-e^{\frac{1}{2}\zeta}\right)s^2\sqrt{T_x}\ln(T_x) \\
&\qquad + \left(1-e^{\zeta}\right)\sqrt{T_x}\ln^3(T_x) + 32\zeta e^{\frac{1}{2}\zeta}s^2\left(\sqrt{T_x}-1\right) \\
&\qquad +\zeta\ln^2(T_x)\left[\sqrt{T_x}\left(1+e^{\zeta}\right) - 2e^{\frac{1}{2}\zeta}\right]\Big\} \qquad \text{(A.35)} \\
\sum_{i=2}^{2N+2} \mathcal{A}_i\mathcal{B}_i &= \frac{2e^{\frac{1}{2}\zeta}\left(e^{\frac{1}{2}\zeta}-1\right)^2 s\sqrt{T_x}\ln(T_x)}{\zeta^2}, \qquad \text{(A.36)}
\end{aligned}$$

where $\zeta = \sqrt{16s^2 + \ln^2(T_x)}$. Solving for the remaining coefficients,

$$\begin{aligned}
\lim_{N\to\infty} \mathbf{A}^N &= \begin{pmatrix} T_x^{\frac{1}{4}}\left[\cosh(\frac{\zeta}{4}) + \frac{\ln(T_x)\sinh(\frac{\zeta}{4})}{\zeta}\right] & \frac{4sT_x^{\frac{1}{4}}\sinh(\frac{\zeta}{4})}{\zeta} \\ \frac{4sT_x^{\frac{1}{4}}\sinh(\frac{\zeta}{4})}{\zeta} & \frac{T_x^{\frac{1}{4}}e^{-\frac{1}{4}\zeta}\left[\ln(T_x)+\zeta+e^{\frac{1}{2}\zeta}(\zeta-\ln T_x)\right]}{2\zeta} \end{pmatrix} \qquad \text{(A.37)} \\
&= \begin{pmatrix} \mathcal{A}_1 & \mathcal{A}_2 \\ \mathcal{B}_1 & \mathcal{B}_2 \end{pmatrix}. \qquad \text{(A.38)}
\end{aligned}$$

Finally, the displacement vector and covariance matrix, accounting for the extraneous losses and the transmission of the system under study, are

$$\begin{aligned}
\vec{d} &= \alpha \begin{pmatrix} \sqrt{T_pT\eta_p\sqrt{T_x}}\left[\cosh(\frac{\zeta}{4}) + \frac{\ln(T_x)\sinh(\frac{\zeta}{4})}{\zeta}\right] \\ \frac{4sT_x^{\frac{1}{4}}\sinh(\frac{\zeta}{4})}{\zeta} \\ \sqrt{T_pT\eta_p\sqrt{T_x}}\left[\cosh(\frac{\zeta}{4}) + \frac{\ln(T_x)\sinh(\frac{\zeta}{4})}{\zeta}\right] \\ \frac{4sT_x^{\frac{1}{4}}\sinh(\frac{\zeta}{4})}{\zeta} \end{pmatrix} \qquad \text{(A.39)} \\
\boldsymbol{\sigma} &= \begin{pmatrix} T_pT\eta_p\sigma_{pp} + 1 - T_pT\eta_p & 0 & 0 & \sqrt{T_pT\eta_p\eta_c}\sigma_{pc} \\ 0 & \eta_c\sigma_{cc} + 1 - \eta_c & \sqrt{T_pT\eta_p\eta_c}\sigma_{pc} & 0 \\ 0 & \sqrt{T_pT\eta_p\eta_c}\sigma_{pc} & T_pT\eta_p\sigma_{pp} + 1 - T_pT\eta_p & 0 \\ \sqrt{T_pT\eta_p\eta_c}\sigma_{pc} & 0 & 0 & \eta_c\sigma_{cc} + 1 - \eta_c \end{pmatrix}, \qquad \text{(A.40)}
\end{aligned}$$

where

$$\sigma_{pp} = 1 + \frac{32s^2\sqrt{T_x}\sinh^2(\frac{\zeta}{4})}{\zeta^2} \tag{A.41}$$

$$\sigma_{pc} = \frac{4s\sqrt{T_x}\left[\zeta\sinh(\frac{\zeta}{2}) - 2\ln(T_x)\sinh^2(\frac{\zeta}{4})\right]}{\zeta^2} \tag{A.42}$$

$$\sigma_{cc} = \sqrt{T_x} - 1 + \frac{\sqrt{T_x}\left\{\cosh(\frac{\zeta}{2})\left[\zeta^2 + \ln^2(T_x)\right] - \ln(T_x)\left[\ln(T_x) + 2\zeta\sinh(\frac{\zeta}{2})\right]\right\}}{\zeta^2}. \tag{A.43}$$

This can also be used to find the normalized probe and conjugate intensity noise such that

$$\frac{\langle\Delta^2\hat{n}_p\rangle_0}{\langle\hat{n}_p\rangle_0} = \sum_{i=1}^{2N+2}\mathcal{A}_i^2 \tag{A.44}$$

$$= \frac{16s^2\left\{1 - \sqrt{T_x}\left[1 - \cosh(\frac{\zeta}{2})\right]\right\} + \ln^2(T_x)}{\zeta^2}, \tag{A.45}$$

$$\frac{\langle\Delta^2\hat{n}_c\rangle_0}{\langle\hat{n}_c\rangle_0} = \sum_{i=1}^{2N+2}\mathcal{B}_i^2 \tag{A.46}$$

$$= \frac{2\sqrt{T_x}\left[8s^2 + (\zeta^2 - 8s^2)\cosh(\frac{\zeta}{2}) - \zeta\ln(T_x)\sinh(\frac{\zeta}{2})\right] - \zeta^2}{\zeta^2}. \tag{A.47}$$

The balanced intensity difference is given by Jasperse *et. al* [64] as

$$\frac{\langle\Delta^2\left(\hat{n}_p - \hat{n}_c\right)\rangle_0}{\langle\hat{n}_p\rangle_0 + \langle\hat{n}_c\rangle_0} = \frac{\sum_{i=1}^{2N+2}\left(\mathcal{A}_1\mathcal{A}_i - \mathcal{B}_1\mathcal{B}_i\right)^2}{\mathcal{A}_1^2 + \mathcal{B}_1^2} \tag{A.48}$$

$$= 1 - \frac{2s\sinh^2(\frac{\zeta}{4})}{\zeta\cosh(\frac{\zeta}{2} + \varsigma)} - \sqrt{T_x}\frac{s\ln^2(T_x)\sinh^4(\frac{\zeta}{4})}{2\zeta^3\cosh(\frac{\zeta}{2} + \varsigma)}, \tag{A.49}$$

where $\tanh(\varsigma) = \frac{\ln(T_x)}{\zeta}$.

Appendix B

Fitting of Theory Parameters to Experimental Measurement Results

The fitting for the s and T_x values in Chapter 5 are done by the method of least squares. This method assumes that the best fit for a given data set is one that minimizes the variance of the data to the fit. Thus, a minimization of χ^2 defined as

$$\chi^2(p_1, p_2, \ldots, p_N) = \sum_i \frac{[y_i - y(p_1, p_2, \ldots, p_N|x_i)]^2}{\Delta^2 y_i}, \tag{B.1}$$

where, y_i and x_i are measured values, $y(p_1, p_2, \ldots, p_N|x_i)$ is the function to fit to y_i. This is done using the corresponding x_i data to find fitting parameter $p_1, p_2, \ldots, p_N$. The final term, $\Delta^2 y_i$, is the variance of the y_i measurement. Each measurement is thus weighted by how well known the y_i value is and a noisy measurement has less weight than a precise one.

To give an example, let us find the location of the beam waist for a laser. At each location along the beam path, x_i, multiple recordings of the beam radius, w_i, are taken. The multiple measurements of the radius give the variance in the measurement, $\Delta^2 w_i$. The laser radius, w, changes with propagation as

$$w(x) = w_0 \sqrt{1 + \left[\frac{\lambda(x - x_0)}{\pi w_0^2}\right]^2}, \tag{B.2}$$

where w_0 is the waist located at x_0 and λ is the wavelength of the laser. The χ^2 is then

$$\chi^2(w_0, x_0) = \sum_i \frac{\left\{w_i - w_0 \sqrt{1 + \left[\frac{\lambda(x_i - x_0)}{\pi w_0^2}\right]^2}\right\}^2}{\Delta^2 w_i}. \tag{B.3}$$

The best fit to the data using the method of least squares is given by the fitting parameters w_0 and x_0 that minimize Eq. (B.3).

The difficulty in this method comes from the minimization of χ^2. This could be done by brute force and examining every possible value of the fitting parameters in $y(x_i)$, but it would take a long time to explore the entire parameter space for an answer with sufficient significant digits. Also, if too few significant digits are used a local minimum could be chosen instead. Another method could be to take derivatives of each fitting parameter setting them to zero to find the extremum values and testing those for the minimum χ^2. However, complicated equations or systematic errors in data taking could make it so there is no solution using this method.

A better way to minimize χ^2 is to use optimization algorithms that adjust initial values of the coefficients to search for the values that minimize χ^2. Care must be taken in choosing an optimization algorithm, as some can get stuck in local minimums. The differential evolution (DE) algorithm that we use is known to be able to reliably find global minimums.

B.1 Differential evolution

The DE is a type of genetic algorithm in which an initial population of possible fitting parameter values are generated and then the population is mixed in order to optimized χ^2. In the example above, to minimize Eq. (B.3) an initial population would contain a set of points P_j such that each point $P_j = \{w_0^{(j)}, x_0^{(j)}\}$ where $w_0^{(j)}$ and $x_0^{(j)}$ are guessed values for the fitting of Eq. (B.2) to the data.

The possible values of the fitting parameters are bounded to decrease computational time and keep the values physical. For the example above, if the data was taken properly the measurements will be made before and after the minimum waist location. Thus, the position can be bound by the largest and smallest distance measured and the minimum waist also by zero and the largest measured. An initial inspection of the data could shrink this bound further.

For each P_j the χ_j^2 is calculated. The next population is generated based on the χ^2 of each point of the previous generation. To do this, a point P_{best} is found that has the lowest χ^2 of the population. Next, a point $P_i \neq P_{\text{best}}$ would be chosen from the previous generation and it will be decided whether to keep P_i for the next generation or to update it. This will be done for each point, so the order the points are chosen does not matter.

To generate a new point P', two other points of the previous generation are chosen at random, P_{source} and P_{sink}, such that $P_i \neq P_{\text{best}} \neq P_{\text{source}} \neq P_{\text{sink}}$. The two new points are used to generate a vector to create point P' from the best point P_{best}. The vector is the direction from source to sink and is normalized by the size of fitting parameter space, $\sqrt{\sum_i (p_i^{min} - p_i^{max})^2}$ where p_i^{min} and p_i^{max} are the minimum and maximum allowed values for parameter p_i. For optimizing Eq. (B.3), let us assume $P_{\text{source}} = \{w_0 = 1 \text{ mm}, x_0 = 10 \text{ cm}\}$ and $P_{\text{sink}} = \{w_0 = 2 \text{ mm}, x_0 = 5 \text{ cm}\}$. If the fitting parameter space is constrained by $0 \text{ mm} \leq w_0 \leq 5 \text{ mm}$ and $1 \text{ cm} \leq x_0 \leq 11 \text{ cm}$, a vector of

$$\frac{\{2 \text{ mm} - 1 \text{ mm}, 5 \text{ cm} - 10 \text{ cm}\}}{\sqrt{(0 \text{ mm} - 5 \text{ mm})^2 + (1 \text{ cm} - 11 \text{ cm})^2}} \approx \frac{\{0.1 \text{ cm}, -5 \text{ cm}\}}{10.01 \text{ cm}} \tag{B.4}$$

would be generated and added to $P_{\text{best}} = \{3\text{ mm}, 8\text{ cm}\}$ to generate $P' \approx \{3.1\text{ mm}, 3\text{ cm}\}$.

The χ^2 of P' is then calculated and if P' has a lower χ^2 than P_i it typically replaces it. The replacement is performed 70% of the time in order to improve the algorithms ability to find the global minimum and not get stuck in local minimums. For each point, except P_{best}, in the previous generation the next P_i is chosen with new P_{source} and P_{sink} until all point in the population of the previous generation have been used as a P_i. P_{best} is always used in the new generation.

The number of generations needed is not a known quantity, and the process is typically repeated until the population occupies a small region of the fitting parameter space. Generally when the range of values for each fitting parameter is smaller than the uncertainty in the fitting. The values of point P_{best} of the last generation are then taken as the best values for the fitting parameters.

Given that there is some uncertainty in measured values, there is not one single set of coefficient values that line up with the data as a possible fit. To find the uncertainty in the fitted coefficient values, the reduced χ^2 must first be found. For N measurements to fit M coefficients the degree of freedom (DoF) for the fit is $N - M$. The reduced χ^2 (χ^2_r) is χ^2 divided by the DoF. For a good fit of the data $\chi^2_r \approx 1$ is needed. It is possible for the $\chi^2_r < 1$, but as long as χ^2_r is not $\ll 1$ the fit is considered fine.

To understand where $\chi^2_r = 1$ comes from, let us look at a y that is independent of x_i. Thus, we will be looking for the mean of y. The χ^2_r for N sets of measurements is

$$\chi^2_r = \frac{1}{\Delta^2 y}\left(\frac{1}{N-1}\sum_{i=1}^{N}[y_i - y(x_i)]\right) \tag{B.5}$$

where $\Delta y_i = \Delta y$ since all the variances should be the same and the DoF is $N-1$ since there is one coefficient, the mean value. The terms in the parenthesis in Eq. (B.5) is the same as the variance of y_i, thus the χ^2_r should equal 1. For actual fittings, the χ^2_r is ratio of the fitting variance to the average variance of each set of data.

The error in the fitting of the coefficients is found by finding the values of the coefficients that increase the χ^2 by χ^2_r. For example, assume the beam waist is found to be 3.85 mm at 6.29 cm with a χ^2 of 13.4 and χ^2_r of 1.7 from the 2 coefficients and 10 sets of data. From the previous DE algorithm, it was found, since the χ^2 at each point from each generation was saved, that a waist of 3.88 mm and 3.82 mm gives a $\chi^2 = 15.1 = \chi^2_r + \min\chi^2$. Therefore the waist is 3.85 ± 0.03 mm.

B.2 Finding s and T_x

To find s and T_x for the experiment in Chapter 5, we used the method of least squares for each measurement, y_i, such that

$$\chi^2 = \sum_i \frac{[y_i - f_i(s, T_x)]^2}{\langle \Delta^2 y_i \rangle}, \tag{B.6}$$

where each measurement prediction f_i is from Eqs. (5.68)-(5.70) for the normalized probe, conjugate, and intensity difference noise. A single trace of 8000 points was taken for the balanced intensity difference, probe intensity noise, and conjugate intensity noise. Each divided by the intensity noise of a coherent state of equal power, which corresponds to the difference of two coherent states for the intensity difference noise. After correcting for imperfect detection from propagation and imperfect detectors, we take the base 10 logarithm of the measurements and compared it to the log of the theory to find the GoF, which is given by χ^2. The variance of each measurement was the variance of the $\log_{10}$ of the measurements.

For the DE, the coefficients were limited to $0 \leq s \leq 3$ and $0.5 \leq T_x \leq 1$. A population of 5,000 points was generated and the algorithm ran until the spread of point was at least an order of magnitude smaller than the error in s and T_x. The minimum GoF=0.4563. Since there are three measurements and two coefficients, the χ_r^2 is the same as the GoF. To find the error, we had saved each point of every generation and created a subset of those points where the GoF ≤ 0.9126. The maximum and minimum values of s and T_x in that subset are the standard errors for the fitting. The values found were $s = 2.04 \pm 0.02$ and $T_x = 0.71 \pm 0.02$.

Appendix C

Kramers-Kronig Relations

The Kramers-Kronig relation (KKR) states that the real and imaginary parts of a transfer function $\tau(f)$ must be related by a Hilbert transform,

$$\begin{aligned} \Re[\tau(f)] &= \frac{1}{\pi}\mathcal{P}\int_{-\infty}^{\infty}\frac{\Im[\tau(f')]}{f-f'}\,\mathrm{d}f & \text{(C.1)} \\ &= H[\Im[\tau(f)]] & \text{(C.2)} \end{aligned}$$

$$\begin{aligned} \Im[\tau(f)] &= -\frac{1}{\pi}\mathcal{P}\int_{-\infty}^{\infty}\frac{\Re[\tau(f')]}{f-f'}\,\mathrm{d}f & \text{(C.3)} \\ &= -H[\Re[\tau(f)]], & \text{(C.4)} \end{aligned}$$

where $\mathcal{P}$ denotes the Cauchy principal value integral, $\Re[\cdot]$ the real part of the function, $\Im[\cdot]$ the imaginary part, and $H[\cdot]$ the Hilbert transform. The change in sign from the real to the imaginary equation is due to the Hilbert transform being the negative inverse of itself,

$$\tau(f) = -H[H[\tau(f)]]. \tag{C.5}$$

The KKR comes from causality given that a physical system cannot react instantaneously to a driving force without responding before the driving force is applied. As is always the case, these relations need to be satisfied when the response of the system is generalized.

The transfer function for the initial Lorentzian lineshape with zero off resonance transmission and perfect on resonance transmission for a unitless frequency F is given by

$$\tau(F) = \frac{1}{1-iF} = \frac{1}{1+F^2} + i\frac{F}{1+F^2}. \tag{C.6}$$

Arbitrary on resonance transmission for zero off resonance transission can be set simply by multiplying by $\sqrt{T_{\mathrm{res}}}$ as it simply rescales the response. Setting an arbitrary off resonance transmission is more difficult as, due to causality, an offset cannot be added to the transfer function as a response at infinite frequency is not physical. Using the linearity of the transform, $H[f+g] = H[f] + H[g]$, if two transfer functions follow KKR then so does the sum

of them. This is how we are able to find the transfer function for arbitrary on and off resonance transmissions for the Lorentzian lineshape, adding two transfer functions. The second response is set much wider than the first to approximate an offset as, near the resonance of the initial transfer function, the second transfer function can be treated as flat. This is done by taking the infinite limit for the HWHM of the second transfer function.

To find the transfer function for an arbitrary resonance, we solve for A and B in

$$T_{\text{off}} + \frac{T_{\text{res}} - T_{\text{off}}}{1+F^2} = \lim_{\sigma\to\infty} |A\tau_1(F) + B\tau_2(F/\sigma)|^2 \tag{C.7}$$

$$= \lim_{\sigma\to\infty} \frac{A^2}{1+F^2} + \frac{B^2}{1+\left(\frac{F}{\sigma}\right)^2} + \frac{2AB}{(1+F^2)\left(1+\left(\frac{F}{\sigma}\right)^2\right)} \tag{C.8}$$

$$= \frac{A^2+2AB}{1+F^2} + B^2. \tag{C.9}$$

Here it is easy to see that $B^2 = T_{\text{off}}$ and $A^2 + 2AB = T_{\text{res}} - T_{\text{off}}$ such that

$$A^2 + 2\sqrt{T_{\text{off}}}A + T_{\text{off}} - T_{\text{res}} = 0 \tag{C.10}$$

$$A = -\sqrt{T_{\text{off}}} \pm \sqrt{T_{\text{off}} - (T_{\text{off}} - T_{\text{res}})}. \tag{C.11}$$

After testing solutions, the answer that makes physical sense is $A = \sqrt{T_{\text{res}}} - \sqrt{T_{\text{off}}}$. Therefore the phase for this system is given by

$$\phi = \lim_{\sigma\to\infty} \arctan\left(\frac{\Im[(\sqrt{T_{\text{res}}} - \sqrt{T_{\text{off}}})\tau_1(F) + \sqrt{T_{\text{off}}}\tau_2(F/\sigma)]}{\Re[(\sqrt{T_{\text{res}}} - \sqrt{T_{\text{off}}})\tau_1(F) + \sqrt{T_{\text{off}}}\tau_2(F/\sigma)]}\right) \tag{C.12}$$

$$= \arctan\left(\frac{\frac{(\sqrt{T_{\text{res}}}-\sqrt{T_{\text{off}}})F}{1+F^2}}{\frac{(\sqrt{T_{\text{res}}}-\sqrt{T_{\text{off}}})}{1+F^2} + \sqrt{T_{\text{off}}}}\right) \tag{C.13}$$

$$= \arctan\left(\frac{F(\sqrt{T_{\text{res}}} - \sqrt{T_{\text{off}}})}{F^2\sqrt{T_{\text{off}}} + \sqrt{T_{\text{res}}}}\right). \tag{C.14}$$

For the Butterworth lineshape, a similar treatment was not possible due to additional frequency terms appearing in the transmission that could not be removed. Thus, another treatment had to be used. The Bode gain-phase relation (BGPR) is used here. The gain phase relation comes from the radial form of the transfer function,

$$\tau(F) = |\tau(F)|e^{i\arg[\tau(F)]} \tag{C.15}$$

$$\ln[\tau(F)] = \ln[\sqrt{T(F)}\,] + i\phi(F). \tag{C.16}$$

The BGPR states that $\ln[\sqrt{T(F)}\,]$ and the phase are Hilbert transforms of each other, like in the KKR; however, unlike the KKR, there is not a unique solution to the imaginary part, the phase, if only the real part is known. The Hilbert transform of the natural log of the square root of the transmission response will give the minimum phase solution, but larger changes in phase with frequency are possible.

To numerically solve for the third order Butterworth phase for Fig. 6.5 we used two different methods. The first is the fast Hilbert transform (FHT) based on the fast fourier transform (FFT). For a function $g(t)$, the Fourier transform, $\mathcal{F}[g(t)](f)$, of a Hilbert transform gives

$$\begin{aligned} \mathcal{F}[H[g(t)]](f) &= -i\,\mathrm{sign}(f)\mathcal{F}[g(t)](f) && \text{(C.17)} \\ H[g(t)] &= \mathcal{F}^{-1}[-i\,\mathrm{sign}(f)\mathcal{F}[g(t)](f)](t) && \text{(C.18)} \end{aligned}$$

where

$$\mathrm{sign}(f)\begin{cases} 1 & f > 0 \\ 0 & f = 0 \\ -1 & f < 0 \end{cases} \tag{C.19}$$

gives the sign of the variable. Thus a FHT is an inverse FFT of $-i\,\mathrm{sign}(f)$ times the FFT of the function to be transformed.

This transform is not without problems as the FFT suffers from spectral leakage. For the FFT, only a finite sampling of the data to be transformed is available, due to not being able to record data for infinite amounts of time. This finite length 'windows' the waveform and unless every oscillation is zero at the edges of the 'window', some of the frequencies leak out. Since the FFT treats the sample as if it is repeating, to give an equivalent infinite sampling of the data, the spectral leakage out of the 'window' causes it to be added back in. Luckily, the problems are at the edges of the FFT so the lower frequency terms are unaffected. To examine higher frequencies, a large window is used to push the spectral leakage issue even higher. For the FHT, we used a unitless frequency range of $F = \pm 1,000$ and used only the range $F = \pm 3$ for the phase response.

The second approach is based on the numerical solution of the Hilbert transform from Lee *et. al*[83] to find the phase

$$\phi(F) = \frac{1}{\pi}\mathcal{P}\int_0^\infty \ln\left[\left|\frac{f+F}{f-F}\right|\right]\frac{\mathrm{d}\ln\left[\sqrt{T(f)}\right]}{\mathrm{d}f}\mathrm{d}f, \tag{C.20}$$

using numerical integration over the dummy variable f. Since the response of the system must be zero at very high frequencies, the integration was not done to infinity but to a limit L such that integrating to $L + \delta L$ did not change the solution. The given solution to this equation had many numerical artifacts due to computation, but with sufficient smoothing matched well with the HFT solution. At the end, this form was used only to verify the HFT solution due to the instability of the solution making it difficult to find the derivative of the phase.

Bibliography

[1] Claude Cohen-Tannoudji, Bernard Diu, and Franck Laloë. *Quantum mechanics*. Hermann and John Wiley & Sons Inc., 1996.

[2] J. J. Sakurai and Jim Napolitano. *Modern quantum mechanics*. Addison Wesley, second edition, 2011.

[3] Walther Gerlach and Otto Stern. Der experimentelle nachweis der richtungsquantelung im magnetfeld. *Zeitschrift für Physik*, 9(1):349–352, 1922.

[4] B. Roy Frieden. *Science from Fisher information*. Cambridge University Press, 2004.

[5] Radhakrishna C. Rao. Information and the accuracy attainable in the estimation of statistical parameters. *Bull. Calcutta Math. Soc.*, 1945.

[6] Harald Cramér. *Mathematical methods of statistics*. Princeton University Press, 1974.

[7] C. Radhakrishna Rao. *Selected papers of C.R. Rao*. Wiley, 1994.

[8] Carl W. Helstrom. *Quantum detection and estimation theory*. Academic Press, 1976.

[9] Alexander Holevo. *Probabilistic and statistical aspects of quantum theory*. Springer Basel, 2011.

[10] Charles M. Goldie and Richard G.E. Pinch. *Communication theory*. Cambridge University Press, 1991.

[11] Nicolas Gisin and Rob Thew. Quantum communication. *Nature Photonics*, 1(3):165–171, 2007.

[12] Adeline Orieux and Eleni Diamanti. Recent advances on integrated quantum communications. *Journal of Optics*, 18(8):083002, 2016.

[13] Fabian Furrer, Tobias Gehring, Christian Schaffner, Christoph Pacher, Roman Schnabel, and Stephanie Wehner. Continuous-variable protocol for oblivious transfer in the noisy-storage model. *Nature Communications*, 9(1):1450, 2018.

[14] Sean D. Huver, Christoph F. Wildfeuer, and Jonathan P. Dowling. Entangled Fock states for robust quantum optical metrology, imaging, and sensing. *Physical Review A*, 78(6):063828, 2008.

[15] Qi Wang and Wan-Ming Zhao. A comprehensive review of lossy mode resonance-based fiber optic sensors. *Optics and Lasers in Engineering*, 100:47–60, 2018.

[16] Nikita Toropov, Gema Cabello, Mariana P. Serrano, Rithvik R. Gutha, Matías Rafti, and Frank Vollmer. Review of biosensing with whispering-gallery mode lasers. *Light: Science & Applications*, 10(1):42, 2021.

[17] JiřıHomola, Sinclair S. Yee, and Günter Gauglitz. Surface plasmon resonance sensors: Review. *Sensors and Actuators B: Chemical*, 54(1-2):3–15, 1999.

[18] Ming Li, Scott K. Cushing, and Nianqiang Wu. Plasmon-enhanced optical sensors: A review. *The Analyst*, 140(2):386–406, 2015.

[19] Alex Monras and Matteo G. A. Paris. Optimal quantum estimation of loss in bosonic channels. *Physical Review Letters*, 98(16):160401, 2007.

[20] G. Adesso, F. Dell'Anno, S. De Siena, F. Illuminati, and L. A. M. Souza. Optimal estimation of losses at the ultimate quantum limit with non-Gaussian states. *Physical Review A*, 79(4):040305, 2009.

[21] Carmen Invernizzi, Matteo G. A. Paris, and Stefano Pirandola. Optimal detection of losses by thermal probes. *Physical Review A*, 84(2):022334, 2011.

[22] Timothy S. Woodworth, Kam Wai Clifford Chan, Carla Hermann-Avigliano, and Alberto M. Marino. Transmission estimation at the Cramér-Rao bound for squeezed states of light in the presence of loss and imperfect detection. *Physical Review A*, 102(5):052603, 2020.

[23] Timothy S. Woodworth, Carla Hermann-Avigliano, Kam Wai Clifford Chan, and Alberto M. Marino. Transmission estimation at the fundamental quantum Cramér-Rao bound with macroscopic quantum light. *arXiv:2201.08902*, 2022.

[24] G.S. Atkinson, E.J. Allen, G. Ferranti, A.R. McMillan, and J.C.F. Matthews. Quantum enhanced precision estimation of transmission with bright squeezed light. *Physical Review Applied*, 16(4):044031, 2021.

[25] Paul-Antoine Moreau, Javier Sabines-Chesterking, Rebecca Whittaker, Siddarth K. Joshi, Patrick M. Birchall, Alex McMillan, John G. Rarity, and Jonathan C. F. Matthews. Demonstrating an absolute quantum advantage in direct absorption measurement. *Scientific Reports*, 7(1):6256, 2017.

[26] Elena Losero, Ivano Ruo-Berchera, Alice Meda, Alessio Avella, and Marco Genovese. Unbiased estimation of an optical loss at the ultimate quantum limit with twin-beams. *Scientific Reports*, 8(1):7431, 2018.

[27] Fu Li, Tian Li, Marlan O. Scully, and Girish S. Agarwal. Quantum advantage with seeded squeezed light for absorption measurement. *Physical Review Applied*, 15(4):044030, 2021.

[28] J. Sabines-Chesterking, R. Whittaker, S. K. Joshi, P. M. Birchall, P. A. Moreau, A. McMillan, H. V. Cable, J. L. O'Brien, J. G. Rarity, and J. C. F. Matthews. Sub-shot-noise transmission measurement enabled by active feed-forward of heralded single photons. *Physical Review Applied*, 8(1):014016, 2017.

[29] Ravinder R. Puri. *Mathematical methods of quantum optics*. Springer, 2001.

[30] Peter D. Drummond and Zbigniew Ficek, editors. *Quantum squeezing*. Springer, 2004.

[31] Leonard Mandel and Emil Wolf. *Optical coherence and quantum optics*. Cambridge University Press, 1995.

[32] Dominik Šafránek, Antony R Lee, and Ivette Fuentes. Quantum parameter estimation using multi-mode Gaussian states. *New Journal of Physics*, 17(7):073016, 2015.

[33] Stig Stenholm and Kalle-Antti Suominen. *Quantum approach to informatics*. Wiley-Interscience, 2005.

[34] Michael A. Nielsen and Isaac L. Chuang. *Quantum computation and quantum information*. Cambridge University Press, tenth edition, 2010.

[35] Léo Morel, Zhibin Yao, Pierre Cladé, and Saïda Guellati-Khélifa. Determination of the fine-structure constant with an accuracy of 81 parts per trillion. *Nature*, 588(7836):61–65, 2020.

[36] The LIGO Scientific Collaboration. Enhanced sensitivity of the LIGO gravitational wave detector by using squeezed states of light. *Nature Photonics*, 7(8):613–619, 2013.

[37] John R. Taylor. *An introduction to error analysis*. University Science Books, second edition, 1997.

[38] Scott R. Eliason. *Maximum likelihood estimation*. Sage, 1993.

[39] Matteo G. A. Paris. Quantum estimation for quantum technology. *International Journal of Quantum Information*, 07(supp01):125–137, 2009.

[40] Zoran Gajić and Muhammad Tahir Javed Qureshi. *Lyapunov matrix equation in system stability and control*. Academic Press, 1995.

[41] Jing Liu, Xiao-Xing Jing, and Xiaoguang Wang. Quantum metrology with unitary parametrization processes. *Scientific Reports*, 5(1):8565, 2015.

[42] Jeffrey N. Anker, W. Paige Hall, Olga Lyandres, Nilam C. Shah, Jing Zhao, and Richard P. Van Duyne. Biosensing with plasmonic nanosensors. *Nature Materials*, 7(6):442–453, 2008.

[43] Mohammadjavad Dowran, Ashok Kumar, Benjamin J. Lawrie, Raphael C. Pooser, and Alberto M. Marino. Quantum-enhanced plasmonic sensing. *Optica*, 5(5):628, 2018.

[44] Hans-A. Bachor and Timothy C. Ralph. *A guide to experiments in quantum optics*. Wiley-VCH, second edition, 2004.

[45] M. S. Kim, W. Son, V. Bužek, and P. L. Knight. Entanglement by a beam splitter: Nonclassicality as a prerequisite for entanglement. *Physical Review A*, 65(3):032323, 2002.

[46] Kok Chuan Tan and Hyunseok Jeong. Nonclassical light and metrological power: An introductory review. *AVS Quantum Science*, 1(1):014701, 2019.

[47] B. M. Escher, R. L. de Matos Filho, and L. Davidovich. General framework for estimating the ultimate precision limit in noisy quantum-enhanced metrology. *Nature Physics*, 7(5):406–411, 2011.

[48] M. Uria, P. Solano, and C. Hermann-Avigliano. Deterministic generation of large Fock states. *Physical Review Letters*, 125(9):093603, 2020.

[49] Ivan N. Agafonov, Maria V. Chekhova, and Gerd Leuchs. Two-color bright squeezed vacuum. *Physical Review A*, 82(1):011801, 2010.

[50] M.V. Chekhova, G. Leuchs, and M. Żukowski. Bright squeezed vacuum: Entanglement of macroscopic light beams. *Optics Communications*, 337:27–43, 2015.

[51] C. F. McCormick, A. M. Marino, V. Boyer, and P. D. Lett. Strong low-frequency quantum correlations from a four-wave-mixing amplifier. *Physical Review A*, 78(4):043816, 2008.

[52] Henning Vahlbruch, Moritz Mehmet, Karsten Danzmann, and Roman Schnabel. Detection of 15 dB squeezed states of light and their application for the absolute calibration of photoelectric quantum efficiency. *Physical Review Letters*, 117(11):110801, 2016.

[53] Evandro Conforti, Mareli Rodigheri, Tiago Sutili, and Flavio J. Galdieri. Acoustical and 1/f noises in narrow linewidth lasers. *Optics Communications*, 476:126286, 2020.

[54] J. B. Johnson. Thermal agitation of electricity in conductors. *Physical Review*, 32(1):97–109, 1928.

[55] T. Kimura and K. Otsuka. Thermal effects of a continuously pumped Nd^{3+}:YAG laser. *IEEE Journal of Quantum Electronics*, 7(8):403–407, 1971.

[56] Bernard Bendow and Peter D. Gianino. Optics of thermal lensing in solids. *Applied Optics*, 12(4):710, 1973.

[57] Robert W. Boyd. *Nonlinear optics*. Academic Press, 2008.

[58] C. F. McCormick, V. Boyer, E. Arimondo, and P. D. Lett. Strong relative intensity squeezing by four-wave mixing in rubidium vapor. *Optics Letters*, 32(2):178, 2006.

[59] Agilent. Spectrum analyzer basics. *Application note 150*, 2006.

[60] Keysight. Spectrum and signal analyzer measurements and noise. *Application Note: 5966-4008E*, 2017.

[61] Bahaa E. A. Saleh. *Fundamentals of photonics*. Wiley, 1991.

[62] Eric D. Black. An introduction to Pound–Drever–Hall laser frequency stabilization. *American Journal of Physics*, 69(1):79–87, 2001.

[63] Robert W. Boyd. *Radiometry andthe detection of optical radiation*. Wiley, 1983.

[64] M. Jasperse, L. D. Turner, and R. E. Scholten. Relative intensity squeezing by four-wave mixing with loss: An analytic model and experimental diagnostic. *Optics Express*, 19(4):3765, 2011.

[65] Philip R. Bevington. *Data reduction and error analysis for the physical sciences*. McGraw-Hill, 2003.

[66] Rainer Storn and Kenneth Price. *Journal of Global Optimization*, 11(4):341–359, 1997.

[67] Ferrante Neri and Ville Tirronen. Recent advances in differential evolution: A survey and experimental analysis. *Artificial Intelligence Review*, 33(1-2):61–106, 2009.

[68] Jiří Homola. Present and future of surface plasmon resonance biosensors. *Analytical and Bioanalytical Chemistry*, 377(3):528–539, 2003.

[69] Shijie Deng, Peng Wang, and Xinglong Yu. Phase-sensitive surface plasmon resonance sensors: Recent progress and future prospects. *Sensors*, 17(12):2819, 2017.

[70] Yanyan Zhi, Xiao-Chong Yu, Qihuang Gong, Lan Yang, and Yun-Feng Xiao. Single nanoparticle detection using optical microcavities. *Advanced Materials*, 29(12):1604920, 2017.

[71] Matthew R. Foreman, Jon D. Swaim, and Frank Vollmer. Whispering gallery mode sensors. *Advances in Optics and Photonics*, 7(2):168, 2015.

[72] James H. Wade and Ryan C. Bailey. Applications of optical microcavity resonators in analytical chemistry. *Annual Review of Analytical Chemistry*, 9(1):1–25, 2016.

[73] Giampaolo Pitruzzello and Thomas F Krauss. Photonic crystal resonances for sensing and imaging. *Journal of Optics*, 20(7):073004, 2018.

[74] Brian E. Anderson, Bonnie L. Schmittberger, Prasoon Gupta, Kevin M. Jones, and Paul D. Lett. Optimal phase measurements with bright- and vacuum-seeded SU(1,1) interferometers. *Physical Review A*, 95(6):063843, 2017.

[75] Mohammadjavad Dowran, Timothy S. Woodworth, Ashok Kumar, and Alberto Marino. Fundamental sensitivity bounds for quantum enhanced optical resonance sensors based on transmission and phase estimation. *Quantum Science and Technology*, 7(1):015011, 2021.

[76] Rik H.J. Kop, Pedro de Vries, Rudolf Sprik, and Ad Lagendijk. Kramers-Kronig relations for an interferometer. *Optics Communications*, 138(1-3):118–126, 1997.

[77] Boris Gralak, Michel Lequime, Myriam Zerrad, and Claude Amra. Phase retrieval of reflection and transmission coefficients from Kramers–Kronig relations. *Journal of the Optical Society of America A*, 32(3):456, 2015.

[78] Patrick M. Birchall, Euan J. Allen, Thomas M. Stace, Jeremy L. O'Brien, Jonathan C. F. Matthews, and Hugo Cable. Quantum optical metrology of correlated phase and loss. *Physical Review Letters*, 124(14):140501, 2020.

[79] Marcin Jarzyna and Rafał Demkowicz-Dobrzański. Quantum interferometry with and without an external phase reference. *Physical Review A*, 85(1):011801, 2012.

[80] Horace P. Yuen and Vincent W. S. Chan. Noise in homodyne and heterodyne detection. *Optics Letters*, 8(3):177, 1983.

[81] Hendrik W. Bode. *Network analysis and feedback amplifier design*. Isha Books, 2013.

[82] John Bechhoefer. Kramers–Kronig, Bode, and the meaning of zero. *American Journal of Physics*, 79(10):1053–1059, 2011.

[83] M. Howard Lee and O. I. Sindoni. Kramers-Kronig relations with logarithmic kernel and application to the phase spectrum in the Drude model. *Physical Review E*, 56(4):3891–3896, oct 1997.